Remote measurement of surface temperature distributions in laser heated samples

Ladds, David A.

Award date:
1994

Awarding institution:
University of Bath

REMOTE MEASUREMENT OF SURFACE TEMPERATURE DISTRIBUTIONS IN LASER HEATED SAMPLES

Submitted by David A. Ladds
for the degree of
Doctor of Philosophy
of the University of Bath
1994

ProQuest LLC
789 East Eisenhower Parkway
P.O. Box 1346
Ann Arbor, MI 48106-1346

Abstract

A remote method for measuring temperature distributions induced by laser heating on a sample has been developed and tested. Using two dimensional Charge Coupled Device (CCD) detection methods and the assumption of radially symmetric laser heating, the spectral image of a two dimensional sample is compressed into one spatial dimension, and the two dimensional form reconstructed using an inverse Abel transform technique. Using this technique the melting point characteristics of UO_2 have been investigated, and the experimental techniques and mathematical procedures implemented have been validated.

Contents

List of Figures

List of Tables

Acknowledgements

I would like to thank the other members of the research group, Joanna Ayling and Duncan Tytler for their assistance with this work, and my project supervisor Prof. G. Saunders for his enthusiasm and confidence in my work. Thanks are also due to Mr. R. Draper for assistance with equipment design, construction and maintenance; to Wendy Lambson for all matters regarding sample preparation; to Bill Clark for discussion on optical techniques; to Brian Ring and Barry Chapman for general practical help; and to all other members of the School of Physics.

I also wish to thank AEA Technology, Harwell, for financial assistance and general support (including the supply of UO_2 samples); in particular Mr. R. Williamson (Reactor Services Division) and Dr. A. H. Harker (Theoretical Physics Division) for useful consultation.

Special thanks go to Dr. D. Bird for discussion on many mathematical and computational matters during both my time as an undergraduate and as a postgraduate. I would also like to express my gratitude to Joanna Ayling and Martin Saunders for advice during the writing of this thesis.

Finally, I would like to thank Janet Smith for her statistical knowledge, for many hours of proof-reading and constructive criticism and, most importantly, for her continual support and encouragement throughout the period of this work.

Chapter 1

Introduction

Accurate knowledge of the thermal properties of uranium dioxide (UO_2) and similar compounds is essential for modelling the conditions and processes occurring in a fission reactor; one of the important applications of such models is in the consideration of fission reactor safety. In recent years many studies of nuclear oxides have been made, at either high temperatures [1, 2] or pressures [3]; however little work has been performed at elevated temperatures and high pressures simultaneously.

Experimental data relating to thermal conductivity in particular are usually calculated from thermal diffusivity measurements, therefore requiring detailed information of density and specific heat. To obtain information on thermal conductivity directly, temperature gradients must be set up within the material to be investigated. Therefore the aim of this project was to design, construct and test a piece of apparatus to generate temperatures in the region of 6000K, and to measure the induced surface temperature distribution. Both processes must be performed

remotely as this apparatus is intended to be used in conjunction with diamond anvil cells for determination of pressure dependences. Since thermal diffusivity is a transient property governing the time evolution of heat through a body, in order to obtain diffusivity information, the measurement techniques employed in this project must be capable of reconstructing time dependent temperature profiles, in addition to the steady state case. Therefore a single temperature measurement must be performed in as short a time as possible.

Diamond anvil cells are now well established as tools for high pressure generation [4, 5]. A piece of apparatus to measure temperature distributions induced in laser heated diamond anvil cells has been proposed by Heinz and Jeanloz [6] of the University of California, Berkeley. In their system a radial temperature distribution is induced on the sample by heating with an infra-red laser operated in the TEM_{00} mode. This temperature distribution is then reconstructed, using inverse Abel transform and (four wavelength) spectro-radiometric techniques, from a scanned image of the sample surface. As a preliminary to this project the author undertook a two month on-site visit to gain first hand experience of the Berkeley system, and was involved in both the process of obtaining temperature profiles of the heated samples, and the improvement of the mathematical analysis procedures.

The work described in this text covers the design, construction and testing of a new system for measuring temperature profiles, for eventual use with laser heated diamond anvil cells. This apparatus is designed to extend and improve the Berkeley system, detecting many more wavelength images in a much shorter time interval, as well as providing a much greater spatial resolution of the surface temperature

distribution. Use of this new system enables accurate, time resolved investigations of UO_2 and similar compounds to be performed. The temperature profiles obtained from heated samples also allow a direct examination of melting points.

The experimental and mathematical procedures used have been verified using a known temperature source and a material with a known melting temperature. An analysis of the melting point characteristics of stoichiometric UO_2 under ambient pressure has also been performed.

Chapter 2

Experimental Techniques

The steady-state and transient thermal properties of materials, at temperatures of up to approximately 6000K and pressures up to 100kbar, are to be investigated by measuring the two-dimensional temperature distribution induced in a heated sample. Therefore the apparatus used for this experiment must be capable of generating the extremely high temperatures required, and then measuring the temperature distribution induced across the sample surface.

For steady state thermal properties to be investigated, it is necessary to generate (and measure) a stable temperature *distribution* across the sample surface. This allows the application of standard heat conduction models to the particular sample and heating configuration, and the subsequent calculation of thermal conductivities. The heating process must therefore provide a non uniform heat input across the sample surface. The investigation of transient thermal properties requires the measurement of the time evolution of the temperature distribution, allowing the time dependent terms in the relevant heat conduction models to be

included. This demands that the temperature measurement system be capable of performing a measurement as quickly as possible.

2.1 Sample Configurations

Before designing the experimental apparatus, the expected sample configurations must be considered: these include both sample type (for example metals, ceramics etc.) and sample mountings. Both the heating and measurement systems must be unchanged, when different sample types and mounting are used to provide a general system for thermal property measurements.

To achieve the elevated pressures for phase diagram investigations, a diamond anvil cell (DAC) will eventually be used to contain the sample under test. The DAC is a standard tool in high pressure research, and many review articles have been published describing their different forms and uses [4,5]. The particular type of cell acquired for use in this experiment is the Mao-Bell cell, designed primarily for X-ray diffraction studies at pressures exceeding 1Mbar [7–11].

In diamond cell work the samples are extremely small since they are contained within the space between the two diamond culets. With the Mao-Bell cell, the size of the diamond culets may vary between 0.7mm and 0.15mm across, the corresponding sample sizes being smaller still (approximately half the culet dimension). The heating process is therefore required to set up a temperature distribution across this small sample in order that thermal properties may be calculated from standard conduction models. In turn, the measurement system must

also be capable of measuring the distribution across the small sample surface.

The aim of the work discussed in this text is to contruct apparatus to generate and measure temperature distributions induced in urania samples at ambient pressures. Future work will include the extension of this to high pressures using the diamond anvil cell.

For work on urania at ambient pressures and elevated temperatures, a special sealed container, called the Controlled Atmosphere Chamber (CAC), was constructed as described in section 3.3. This allows a sample of uranium compound to be contained within a reducing atmosphere, preventing the stoichiometry of the compound from being changed. The CAC also permits the analysis of samples contained in hostile environments; for example in the presence of toxic atmospheres; or that are themselves toxic and cannot be measured safely under normal laboratory conditions.

2.2 Temperature Generation

The method of heat generation in the sample under test is required to be generally applicable to any type of sample (metal, ceramic, etc.) or sample mounting (sealed gas chamber, DAC, etc.).

The use of diamond anvil cells for determining the pressure dependence of thermal properties severely restricts the choice of techniques that may be adopted. The main problems are that diamond oxidises above 700°C, graphitisation begins above

800°C, and the diamonds lose their strength with increased temperature [4,5]. In heating a sample contained within a DAC to temperatures in the region of 6000K, great care must be taken to ensure that the sample is heated directly, while the diamonds are maintained at low temperature. Any external heating process, for example using resistive collars around the diamonds [12–16], would inevitably heat the diamonds, restricting their use to below 600°C.

Heating the sample itself may be performed by resistive heating [17], or by laser heating [18]. Resistive heating techniques are not suitable for investigating ceramic samples because they require that the sample can be made into thin wires which are passed through the DAC cavity. Laser heating was developed specifically to allow measurements to be performed at extremely high temperatures, especially with samples inside diamond anvil cells [18]. It is a method which can be applied to any sample provided the sample is visible, for example through the diamonds in a DAC or through an optical window in a sealed vessel such as the Controlled Atmosphere Chamber. The heating can be controlled to produce very localised hot areas with large associated temperature gradients, ideal for use in thermal property measurements. Laser heating systems have been used extensively to investigate the phase diagrams and behaviour of materials found in the upper mantle [19–21].

2.3 Temperature Measurement Techniques

There are two main categories of temperature measurement methods that may be considered for this application. The first are direct contact methods where

the measurement device is in thermal contact with the material to be measured. These include thermometers, thermocouples and other resistive techniques. The second type are non-contact methods which use the characteristic thermal radiation emitted by a sample in the measurement process.

The choices for measurement technique are severely limited by the experimental requirements. There are three main factors which rule out the use of direct contact methods. The first is that measurements are to be performed at such extremes of temperature: the hottest part being at several thousand degrees, while the cooler areas are at only a few hundred degrees. Most direct contact methods are only accurate over a small range of temperatures, preventing measurements at many points on the sample being taken simultaneously. The second factor is that the measurement process must determine the temperature *distribution* across the sample surface. To achieve this, many contacts would be required on each sample, which would be both time consuming and complicated to set up. It would also cause the thermal properties of the sample to be altered, since the contacts would necessarily affect the flow of heat across the surface. The third factor is that the measurement process must take as short a time as possible, allowing the investigation of the time evolution of temperature across the sample. The direct contact methods all have a time constant associated with them, since they are dependent on the device and the sample coming into thermal equilibrium before an accurate reading may be taken. This process will also affect the flow of heat through the sample: the devices act as heat sinks (or sources) in order to achieve thermal equilibrium.

In addition to the three factors above, if the sample is contained in a diamond

anvil cell (for investigation of the pressure dependence of thermal properties), it is extremely difficult to attach direct contacts. This is a similar problem to that of attaching heating contacts to a sample, as discussed in section 2.2. Since the measurement system is intended for analysing samples at both ambient and high pressures, the use of the DAC must not affect the measurement process and hence direct contact methods must be ruled out.

The requirements above imply that the a non-contact method using the thermal radiation from the sample is required. There are many such techniques available, the majority of which are based on black-body radiation. The original model for black-body radiation was derived by Wien in 1896 [22] and took the form:

$$I(\lambda, T) = \frac{2\pi hc^2 \varepsilon \lambda^{-5}}{e^{hc/k\lambda T}} \tag{2.1}$$

where h, c and k are Planck's constant, the speed of light in vacuum and Boltzmann's constant respectively, and ε is the emissivity of the sample surface. This model was improved by Max Planck in 1917, to the form:

$$I(\lambda, T) = \frac{2\pi hc^2 \varepsilon \lambda^{-5}}{e^{hc/k\lambda T} - 1} \tag{2.2}$$

where the '-1' term accounted for the discrepancies seen between the Wien model and the experimental observations of black-bodies. Two typical measurement techniques which use black-body radiation are optical pyrometry and spectroradiometry, which are now discussed in turn.

2.3.1 Optical Pyrometry

Optical pyrometry is a widely used technique for black-body temperature measurement [23–27], and two main methods are now outlined briefly.

2.3.1.1 Single wavelength

The simplest measurement technique using black-body radiation is single wavelength optical pyrometry. In this method the light emitted from the hot sample is compared by eye with that from a known temperature source. A schematic diagram of the apparatus is shown in figure 2.1. The two sources are arranged such that both can be viewed simultaneously, the light passing through a red filter to select a small range of wavelengths, generally centred around 555nm where the response of the eye is a maximum. The temperature of the known source is then adjusted until the two become indistinct, at which point it is assumed that they are at identical temperatures.

For an accurate measurement to be performed, the emissivities of the two sources are required to be identical. This is in general not the case, and the effective temperature measured by this type of pyrometer is usually lower than the true sample temperature. This is easily seen by considering the ratio of two Wien curves (equation 2.1) for identical wavelengths, but different emissivities. At the observed intensity match the two intensities are identical, hence

$$\frac{I_s(\lambda)}{I_k(\lambda)} = \frac{2\pi hc^2\lambda^{-5}\varepsilon_s}{2\pi hc^2\lambda^{-5}\varepsilon_k} \cdot \frac{e^{hc/k\lambda T_k}}{e^{hc/k\lambda T_s}} = 1 \tag{2.3}$$

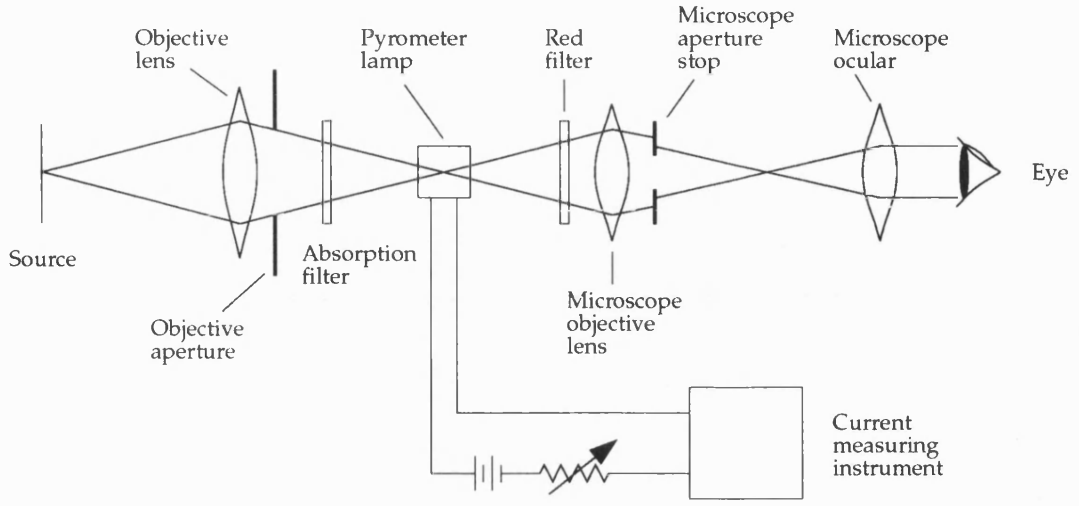

Figure 2.1: Schematic diagram of a single wavelength optical pyrometer.

where $I_s(\lambda)$ and $I_k(\lambda)$ are the measured intensities of the sample and known source respectively, and ε_s, ε_k, T_s and T_k are the emissivities and temperatures of the sample and known source. This reduces to the relationship:

$$\frac{1}{T_k} - \frac{1}{T_s} = \frac{k\lambda}{hc} \ln\left(\frac{\varepsilon_k}{\varepsilon_s}\right), \tag{2.4}$$

which implies that the more ε_s differs from ε_k, the more inaccurate the measured temperature will be. This error is systematic to the experimental technique, and may be corrected for if the emissivity of the sample is known at the wavelength and temperature of the measurement. In this experiment the emissivity of the samples may not necessarily be well known, especially in the case of urania [28], the investigation of which is the main objective of this project (see chapter 1), hence single wavelength pyrometry is unsuitable.

2.3.1.2 Two wavelength pyrometry

The dependence on emissivity may be removed by considering the ratio of intensities at two selected wavelengths. In this way, the intensities of the source and sample are not matched (i.e. $I_s(\lambda) \neq I_k(\lambda)$), but rather the ratios, such that

$$\frac{I_s(\lambda_1)}{I_s(\lambda_2)} = \frac{I_k(\lambda_1)}{I_k(\lambda_2)}. \tag{2.5}$$

where λ_1 and λ_2 are the two selected wavelengths. This removes the emissivity term from the ratio equation, assuming that it is independent of wavelength over the range from λ_1 to λ_2.

Since emissivity is in general dependent on wavelength (for non-grey bodies only) the two chosen wavelengths must be close, avoiding any problem due to inconsistent emissivities ($\varepsilon(\lambda_1) \neq \varepsilon(\lambda_2)$). If the wavelengths are too close, there will not be any discernible difference between the recorded intensities at the two wavelengths, causing the measurement to be invalid. Thus the two wavelength method is a compromise between avoiding emissivity incompatibilities and achieving a discernible intensity difference.

In both single- and two-wavelength pyrometry the whole emitting area of the hot-spot is viewed, producing an average temperature reading. This is obviously not suitable for measuring a surface temperature distribution as generated on the sample by laser heating (section 2.2). If suitable optics are employed to examine only a small area of hot-spot, pyrometry can produce a spot temperature reading, but only one can be recorded at any time. Building up a temperature distribution

will therefore be time consuming. Because of the impracticalities, pyrometry methods are deemed unsuitable for this experiment.

2.3.2 Spectro-radiometry

An alternative to pyrometry is the use of spectroscopic techniques to obtain a spectral image of the sample. The light emitted from a small spot on the sample can be spectrally split, and the resulting image recorded on a one-dimensional linear detector. A mathematical fitting package can then be used to compare the intensity–wavelength data to the Planck equation (2.2), to determine the corresponding temperature (and emissivity if the spectral intensity is known in absolute units) at that particular point on the sample. This will produce a spot measurement on the sample surface, or if the whole sample is examined, a measure of the average temperature in a similar way to the optical pyrometry method.

The prime advantage of spectro-radiometry over pyrometry is that a spectral image may be recorded and stored for analysis at a later stage, allowing subsequent measurements to be performed within a very short time interval. This allows good time resolution of the temperature across the surface, but not spatial resolution of the distribution. An alternative approach is required to achieve the distribution measurement.

2.4 Obtaining Temperature Distributions

As a small section of the sample can be investigated using spectroradiometry, it is apparent that by measuring at several positions across the sample, an impression of the temperature distribution can be built up. This is most easily achieved by using a one-dimensional spectrum analyser that is scanned along a line across the sample, with measurements being taken at regular spatial intervals. This data is then compared to the Planck equation (2.2) to determine the temperature at each spatial position measured. This method would still only produce information about a line across the sample, and unless the line happened to go directly through the centre of the heated spot, the peak temperature could not be measured. To obtain the two-dimensional temperature distribution across the sample requires either many such line scans, or a more complex imaging method.

The main disadvantage of the scanning method is the time taken to perform a measurement, requiring that the sample temperature is stable throughout the duration of the scan. If the temperature changes during the scan, it will appear that there is a temperature gradient across the sample surface, since there is a finite time interval between measurements at the extreme edges. For this experiment, very short exposure images of the sample are required (10-100ms per image), giving an almost instantaneous picture of the sample. This makes it possible to investigate the time development of the temperature distribution by taking many measurements at various time intervals after the heating process has started. This would be almost impossible with a scanning data collection mechanism, as measurements would be required during the transient part of the

temperature development.

2.4.1 Compressing Two Spatial Dimensions into One

Spectral analysis systems using two-dimensional imaging systems, e.g., charge coupled device (CCD) detectors, make it possible to measure instantaneously the wavelength dependence of light emitted by a hot sample as a function of one spatial dimension only. One dimension of the image contains the spatial information, whilst the other contains the wavelength (spectral) information. To measure a two-dimensional distribution it is possible to use a similar scanning method to that mentioned previously; however the problems relating to measuring time development of the temperature distribution are not resolved.

Obtaining a full spectral image of the sample using a two dimensional detector array requires compression of the two spatial dimensions of the sample into one. This can be performed using a different spatial co-ordinate set to the usual Cartesian x–y. For example, an axially symmetric distribution can be described by a one-dimensional function $f(r)$ instead of a two-dimensional set $f(x, y)$. It follows that if an axially symmetric temperature distribution can be generated on the sample surface, it is then possible to measure it using a one dimensional data collection method operating in radial co-ordinates. The use of laser heating as described in section 2.2 provides a radial temperature profile on the sample surface (when the laser is operated in the fundamental TEM_{00} mode, see section 3.1).

The process of measuring radial distributions is a common one in tomographic ap-

plications, for example measuring absorption coefficients in plasma columns or in X-ray Computed Axial Tomography (CAT) scanning. In these applications a two dimensional distribution in the x–y plane is viewed from the side (i.e., from within the plane), and the two dimensional information $f(x, y)$ is then reconstructed using mathematical transforms. These transforms belong to the set derived from the Radon Transform pair, in which a radial function $f(r, \theta)$ can be converted to a Cartesian co-ordinate set $f(x, y)$, or vice versa (see chapter 6).

The experimental apparatus can be arranged to provide the image detection system with a two dimensional function, such that one dimension (x say) contains the spectral information, and the other (y) the radial information transformed into the cartesian co-ordinate system. This experimental process is the one used here, and is discussed in section 3.2.5, with the mathematical reconstruction of the radial function discussed in section 5.6.

Chapter 3

Experimental Design

The experimental system can be divided into two distinct parts: one which performs the heating of the sample, the other which measures the generated temperature distribution. The choice of heating and detection methods is limited by the requirement that both operations be performed remotely. This allows measurements to be made on samples which are contained in hostile environments, or that are toxic and cannot be measured safely under normal laboratory conditions. Possible heating and detection methods have been discussed in chapter 2. In this present chapter the implementation of the systems used in this particular experiment is discussed.

3.1 Generation of High Temperatures

To produce the extremely high temperatures required for measuring thermal properties, an infra-red laser system is used. A schematic view of the heating system

is shown in figure 3.1. The laser used in this system is an 18W continuous wave (c.w.) Nd:YAG laser operated in the TEM_{00} monomode configuration with an output beam diameter of 0.4mm. Using the TEM_{00} mode gives a Gaussian cross-sectional beam profile, and therefore standard Gaussian Beam Optic (Quasi Optic) techniques [29–32] can be employed to analyse the propagation of light through the system. Standard geometric optics cannot be used in this case since the light entering the lens is a parallel beam of infra-red laser radiation, and there is no real object for the lens to form an image.

The TEM_{00} mode is the only one with a single central intensity maximum, and an axially symmetric intensity distribution, which decreases monotonically with distance from beam axis. Therefore using this mode induces a single, axially symmetric hot-spot on the sample, the temperature being a maximum at the spot centre. To simplify any thermal calculations made using the temperature measurements, it is essential that the heating process produces a single hot area on the sample; the symmetry is required to allow the experimental data to be analysed using Abel Transforms.

The emerging laser beam is initially expanded from 0.4mm diameter to 4mm diameter using a standard 10:1 upcollimator (beam expander). This allows a smaller focused spot to be generated on the sample surface for a given focusing lens. Due to space restrictions, the expanded beam must be reflected into the laser focusing optics by 180°, using a gold coated mirror (M_1) and then a dichroic high-pass (or 'hot') mirror (M_2). A gold mirror is used as it has a high reflectance for Nd:YAG radiation at 1064nm [33], and therefore allows maximum power transfer to the focusing optics. The dichroic mirror (M_2) is designed to reflect the Nd:YAG

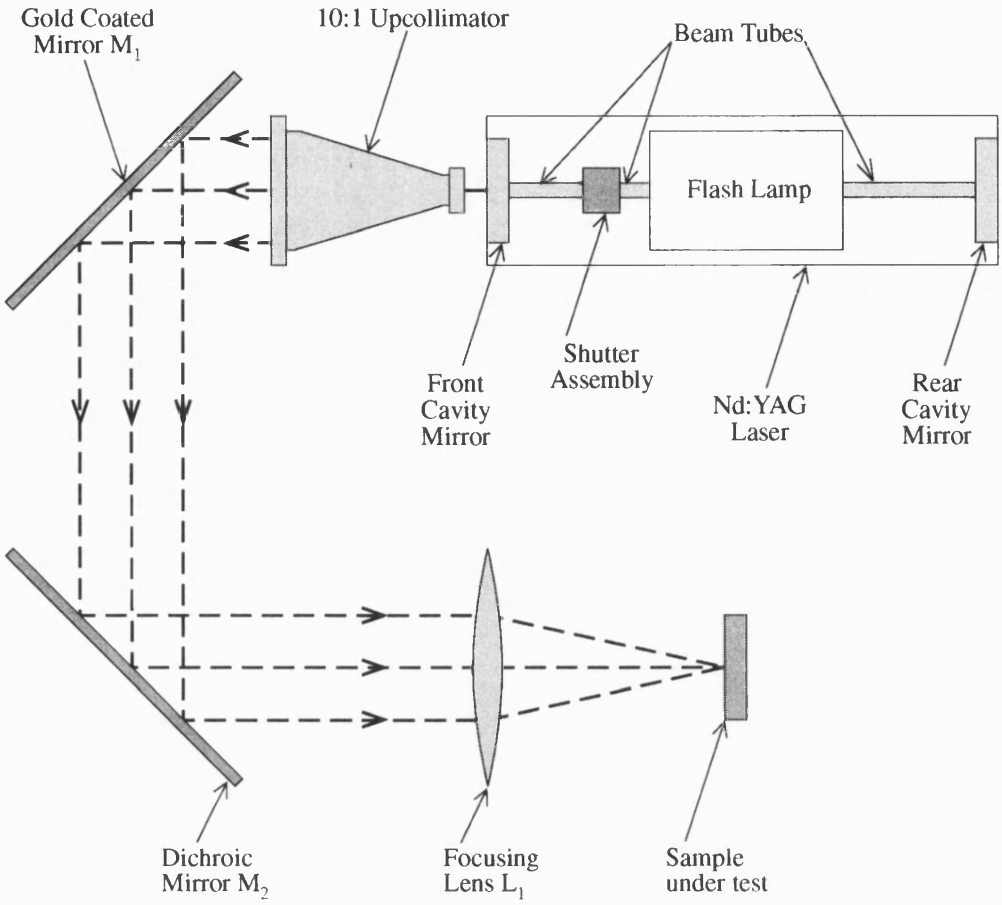

Figure 3.1: Schematic view of the laser heating system.

radiation, but pass the visible then emitted from the sample; this is discussed in more detail in section 3.2.1. Following the two reflections the light enters the focusing lens (L_1), a multi-element, 25mm diameter achromatic lens which produces a focused laser spot on the sample surface, positioned at the focal point of the lens. Lenses with a focal length of 40mm and 70mm have been used.

The diameter of the hot-spot on the sample can be found using Gaussian beam analysis, as mentioned previously. In the calculation of the hot-spot size the main

required characteristic of the beam is its radius w, which is the distance from the beam axis at which the beam intensity falls to $1/e^2$ (≈ 0.135) of its value on the axis. Approximately 86% of the power in the beam is contained within radius w, and approximately 99.97% within $2w$. The focusing lens (L_1) has a radius of $6.25w$ (the laser beam diameter is 4mm and the lens diameter is 25mm) and will therefore allow about 99.9997% of the beam power through. The beam waist w_0 is defined as the smallest beam radius encountered along the beam path, and for systems with a parallel incident beam, is located at the focal point of the lens (where the sample is situated). Therefore calculation of the beam waist allows the expected size of the hot-spot to be determined. The beam waist can be found [32] using the equation

$$2w_0 = \frac{4}{\pi} \cdot \frac{\lambda}{D} \cdot F, \tag{3.1}$$

where F is the focal length of the lens, D is the diameter of the beam where it passes through the lens, and λ is the wavelength of the light. For this experiment D is 4mm (the diameter of the beam after passing through the upcollimator), F is 40mm or 70mm (depending on the lens chosen) and λ is 1064nm since the light beam is monochromatic Nd:YAG laser light. The corresponding beam waists are calculated using equation 3.1, and are tabulated in table 3.1.

Lens	Beam Waist ($2\omega_0$)
40mm	13.54μm
70mm	23.70μm

Table 3.1: Beam waists for given focusing configurations.

The reason for expanding the beam before focusing to a spot is now evident, as the relationship

$$w_0 \propto \frac{1}{D} \tag{3.2}$$

can be deduced from equation 3.1: the beam waist is inversely proportional to the diameter of the beam illuminating the lens. Expanding the beam by a factor of 10:1 therefore reduces the size of the focused spot by a factor of 10, and concentrates the power into a much smaller area. This concentration allows the extremely high temperatures required to be generated on the sample.

The focused beam has a depth of focus associated with it, which is a measure of the divergence of the beam along the beam axis. This is defined as the distance from the beam waist position at which the beam radius is $\sqrt{2}$ times the beam waist. Calculation of the depth of focus is also performed using Gaussian Optics [32], by the equation

$$\mathrm{DOF} = \frac{8\lambda F^2}{\pi D^2} \tag{3.3}$$

The corresponding values for the focusing systems used in this experiment are listed in table 3.2. To allow correct thermal analysis of the heated spot, it is necessary to have the sample surface positioned within the depth of focus. The exact dimensions of the spot and the heat input will then be known, and the heat conduction equations may be used.

Lens	Depth of Focus
40mm	270.9μm
70mm	829.8μm

Table 3.2: Depths of focus for given focusing configurations.

3.2 Measurement of Temperature

The optical system as described in section 3.1 is used to generate a temperature distribution on the surface of a sample placed at the focal point of the laser focusing lens. The measurement system is designed to determine this temperature distribution in as short a time as possible, to allow time dependent studies to be carried out (in later experiments, if required). Due to the way some samples must be contained, it is a remote measurement system, so there can be no surface contact with the sample: an optical system is used. This system can be sub-divided into two sections: the light collection and focusing optics, and the spectral image formation. The collection optics are used to gather the thermal radiation emitted by the sample. The image focusing optics are then used to form a suitable image to be spectrally analysed. The optics must be designed to match the spectral analysis system's requirements, particularly relating to image size.

3.2.1 Collection and Focusing Optics

The collection optics are based around the lens system used for the laser heating, and are illustrated in figure 3.2. The light emitted by the hot sample is focused to a parallel beam by the laser focusing lens (L_1) since the sample surface is positioned

at its focal length. This ensures that the area examined by the temperature measurement system is the same as that heated by the laser. The parallel beam then passes through the dichroic ('hot') mirror (M_2) which separates the incident laser beam and the radiated light. This mirror is actually an interference filter consisting of multiple layers approximately 1μm apart, which diffract light at wavelengths in the region of 1.064μm (Nd:YAG light). The passage of visible light through the mirror induces unwanted intensity ripples in its spectral distribution due to diffraction effects. These ripples must be corrected for in the subsequent mathematical analysis (see section 5.1). A 1.064μm filter (F_1) is used after the dichroic mirror, to ensure that any laser light reflected from the sample surface or the intermediate optics, and passed through the mirror (M_2), does not enter the detection optics.

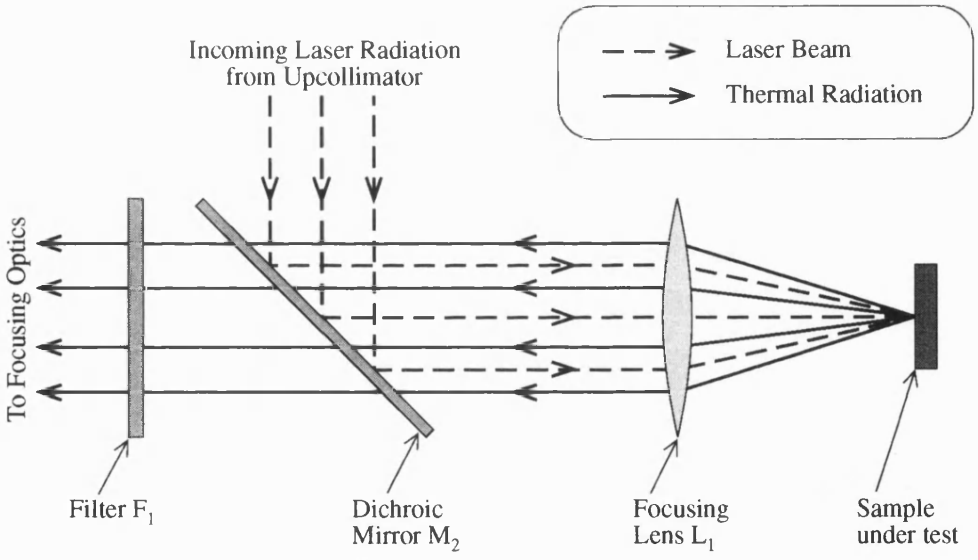

Figure 3.2: Schematic view of the light collection optics

After passing through the filter the light is focused to an image on the spectrograph entrance slit. As explained in section 3.2.5, the larger the image is vertically (per-

pendicular to the direction of spectral splitting in the spectrograph) the greater the number of rows of pixels on the CCD detector the image will cover. The focusing optics must therefore be designed to generate an image which is as large as possible vertically (and hence fills the maximum number of CCD detector rows) but is still small enough to fit within the slit width. It is essential that the image is not wider than the slit, as that would destroy the axial symmetry of the image and invalidate the use of the Abel Inversion in the analysis.

The focusing system may take several forms, and three that have been used in this experiment are discussed here. The first example is the simplest, using only one extra lens. A circular image is formed, which is contained within the width of the entrance slit. This method covers fewer CCD rows than the other two methods and so has the lowest vertical resolution.

The second example uses a microscope objective to form an image much wider than the spectrograph slit. This can be useful for measuring lines across non-axially symmetric temperature profiles generated, for example, on non-homogeneous samples, or near the sample edge.

The third focusing system uses cylindrical optics to focus a vertically magnified image within the slit to maximise the vertical resolution of the image, while still containing the image width within the slit. This is the usual system used in this experiment as it produces the largest spatial resolution of the three (which are now discussed in turn).

3.2.2 Circular Focusing System

The simplest focusing system uses a single circular lens to focus a small image of the hot-spot within the spectrograph entrance slit. As the entire hot-spot is examined, the Abel Inversion is necessary to calculate radial temperature profiles from the line integrals that constitute the recorded data set.

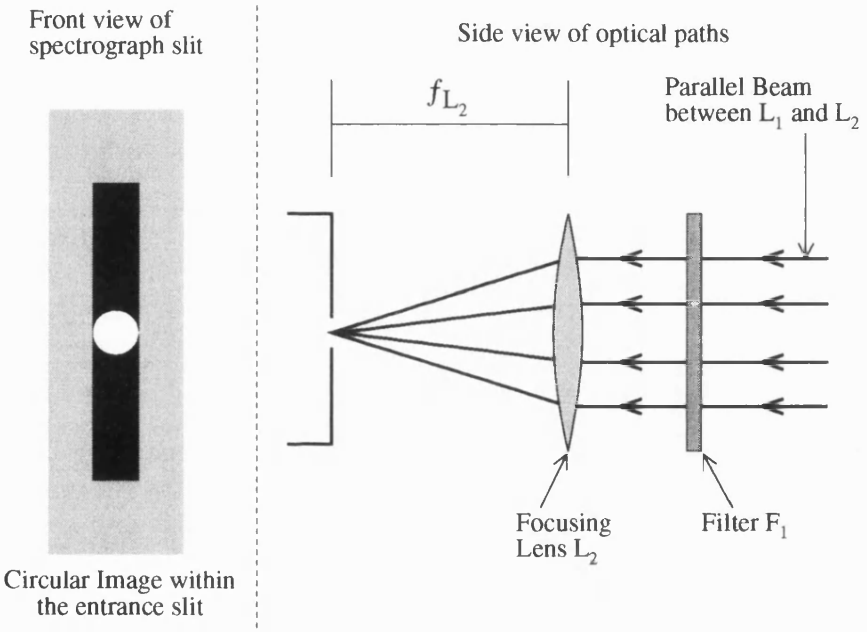

Figure 3.3: Circular lens focusing system forming a circular image within the spectrograph entrance slit.

The position of the lens L_2 is shown in figure 3.3 together with an impression of the image formed within the spectrograph slit. Clearly the number of rows on the CCD that the image falls on are limited by the width of the slit since the image is circular. To obtain a better vertical resolution the slit must be made as wide as possible to allow a large image to be formed. However, the operation of the spectrograph requires that the slit be as narrow as possible to prevent

horizontal smear between wavelengths, as discussed in section 3.2.5. The choice of slit width is therefore a compromise between vertical resolution and reduction of wavelength overlap. The spectrograph is supplied with slit widths of 50μm, 100μm and 250μm. The images focused within these slits cover a maximum of 3, 5 and 11 CCD pixels respectively (see section 3.2.5). The 250μm slit must therefore be used in this system since the smaller slit would not provide any useful resolution of surface temperature.

The lens L_2 must be selected to produce a focused image of the correct dimension within the spectrograph entrance slit. Since lens L_1 focuses the thermal radiation from the sample surface to a parallel beam, lens L_2 can be positioned at any point along the beam without affecting the final image. By considering the limiting case when the distance between the two lenses approaches zero, they can be then treated as a single lens and the optics become much simpler.

The diameter of the focused laser spot on the sample has already been calculated (as $2w_0$) using Gaussian beam optics. The hot spot size is not necessarily equal to the laser spot size due to radial heat conduction across the sample surface. As stated previously, approximately 99.97% of the beam power is contained within twice the beam waist diameter ($4w_0$). To ensure that the image of the hot spot is always contained within the width of the slit, a hot spot diameter of approximately $8w_0$ is considered in the calculation of image distance. This assumption allows the hot spot to be twice as wide again, and allows high thermal conductivity materials to be examined, where the heat spreads over a much larger surface area than the beam heats directly, while still maintaining the image within the slit.

The horizontal magnification required for the image of the spot to fill the width of the spectrograph slit is determined by

$$M = -\frac{W_s}{D_h} \tag{3.4}$$

where W_s is the width of the spectrograph slit, and D_h is the diameter of the hot spot. The magnification is negative since the image is inverted. From the Gaussian lens equation, the magnification is also related to the distances of the object (s_o) and image (s_i) from the lens by the equation

$$M = -\frac{s_i}{s_o}. \tag{3.5}$$

In the case of the two lens model, the distances s_o and s_i are equal to the focal lengths of the lenses L_1 and L_2 respectively. Equation 3.5 can therefore be written in the more useful form as

$$M = -\frac{f_{L_2}}{f_{L_1}}. \tag{3.6}$$

Combining equations 3.5 and 3.6 produces the relationship

$$\frac{f_{L_2}}{f_{L_1}} = \frac{W_s}{D_h}. \tag{3.7}$$

The overall magnification of the image is therefore determined by the ratio of the focal lengths of the two lenses. It is interesting to note that when a Gaussian

beam analysis was performed on the two lens system the same result for the magnification factor was obtained.

The diameter D_h is assumed to be $8w_0$ (as stated previously), therefore substituting equation 3.1 into 3.7 produces the relationship

$$f_{L_2} = W_s \cdot \frac{\pi D}{16\lambda_L} \tag{3.8}$$

where D and λ_L are system parameters equal to the diameter and wavelength of the heating laser incident on L_1. For the system used in this experiment (assuming a slit width of 250μm, a beam diameter of 4mm, and beam wavelength of 1064nm), the focal length of L_2 is calculated as

$$f_{L_2} = 18.45\text{cm}. \tag{3.9}$$

The corresponding focal lengths for the slit widths 100μm and 50μm are 7.38cm and 3.69cm respectively.

Equation 3.8 shows that the focal length of L_2 is independent of the focal length of L_1. This is a useful result, since L_1 can be varied to produce either a strong, localised heating pulse or a wide, heating area without affecting the focal length of L_2 required to form a magnified image. The only situations in which L_2 need be changed are if the spectrograph slit, or the laser beam characteristics are altered.

3.2.3 Microscope Objective

An adaptation of the circular lens system uses an extra, short focal length lens (L_3) positioned after the imaging lens (L_2) in figure 3.3, such that it produces a magnified circular image of the intermediate image formed by lens L_2. The ray diagram, figure 3.4, shows the relative positions of the circular lens system and the extra lens (L_3). The magnified image may be wider than the spectrograph slit; however it must fit within the vertical height of the slit. The spectrograph slit can then be positioned to select any line across the magnified image. Therefore this system allows a line profile across the sample to be measured, rather than a full surface distribution.

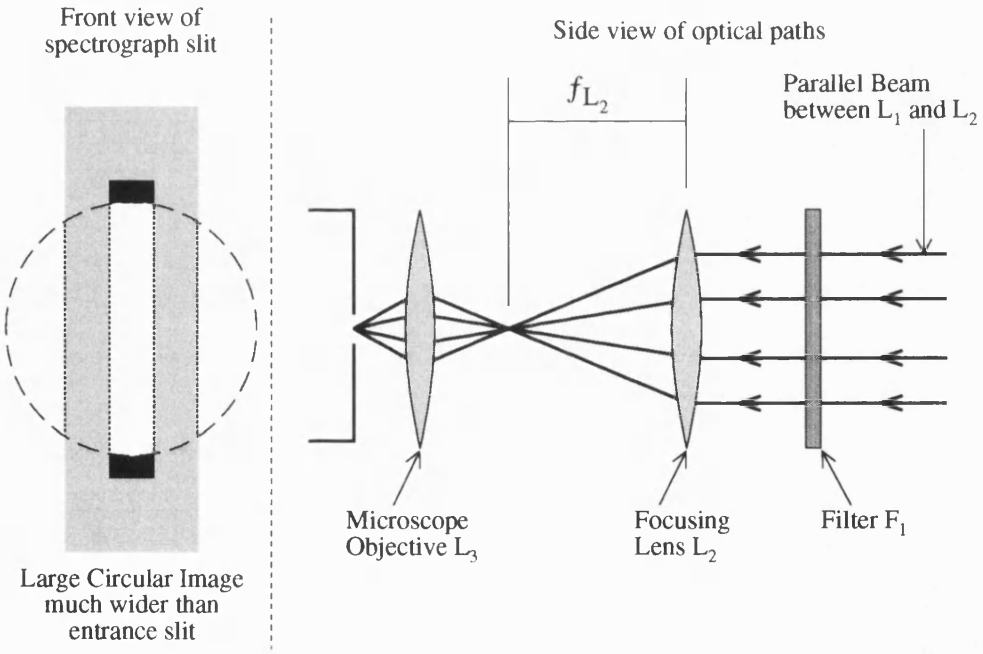

Figure 3.4: Microscope objective focusing system which is used to form an enlarged image wider than the entrance slit.

The prime advantage of this particular focusing system is that there is no need for the Abel Inversion stage of the mathematical analysis, since the data does not consist of sets of line profiles. If the hot-spot on the sample is not axially-symmetric, for instance due to edge effects, the Abel Inversion process cannot be performed. By examining a particular line across the spot, it is possible to measure a selected temperature profile. This system also has a very large spatial resolution because the image of a small hot-spot can be enlarged to fill the full height of the CCD detector.

The main disadvantage of this particular optical arrangement is that unless the centre of the image can be accurately positioned coincident with the slit, it is very difficult to measure the peak temperature on the sample. Since only a small fraction of the image actually enters the slit, a long exposure on the CCD detector is required, to allow enough light for a single data scan to be collected. This is contrary to the requirements of the experiment that near instantaneous data be recorded to prevent problems associated with unstable temperature distributions.

A secondary problem associated with this method is that it can only measure the average temperature in the region around the temperature peak. This problem is illustrated in figure 3.5, which shows a cross-section through the centre of an image is focused onto the entrance slit. Around the centre of the spot, several temperature contour lines are present within the width of the slit, and only the average temperature over this range can be determined. This effect can be reduced by using the narrowest slit available, thus decreasing the number of temperatures detected around the central maximum.

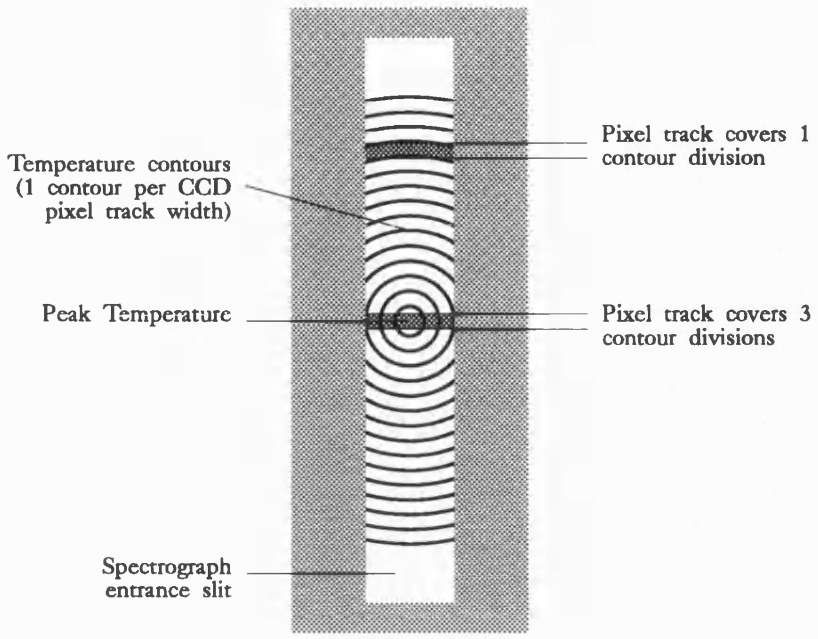

Figure 3.5: Average temperature measurement across microscope objective image.

To illustrate the form of data obtained using this focusing system, figure 3.6 shows the image obtained from a 250μm diameter annulus, back-illuminated by a known colour temperature light source. The spectrograph slit was positioned as near to the centre of the image as possible (actual positioning judged by eye) to obtain what would be a peak temperature, when a heated spot is being viewed.

This image clearly shows the cross-section through an annulus: a bright centre surrounded by a dark ring, with a surrounding light ring. Since this data corresponds to a spectrally split line through the image, the only mathematical analysis required is to correct for the spectral response of the system and to fit the data to the Planck curve (see section 5.7). The results from the fit are shown in figure 3.7. This selected data set is of poor quality, containing dark stripes across the centre and light bands at the edges. The low temperature points in the temperature

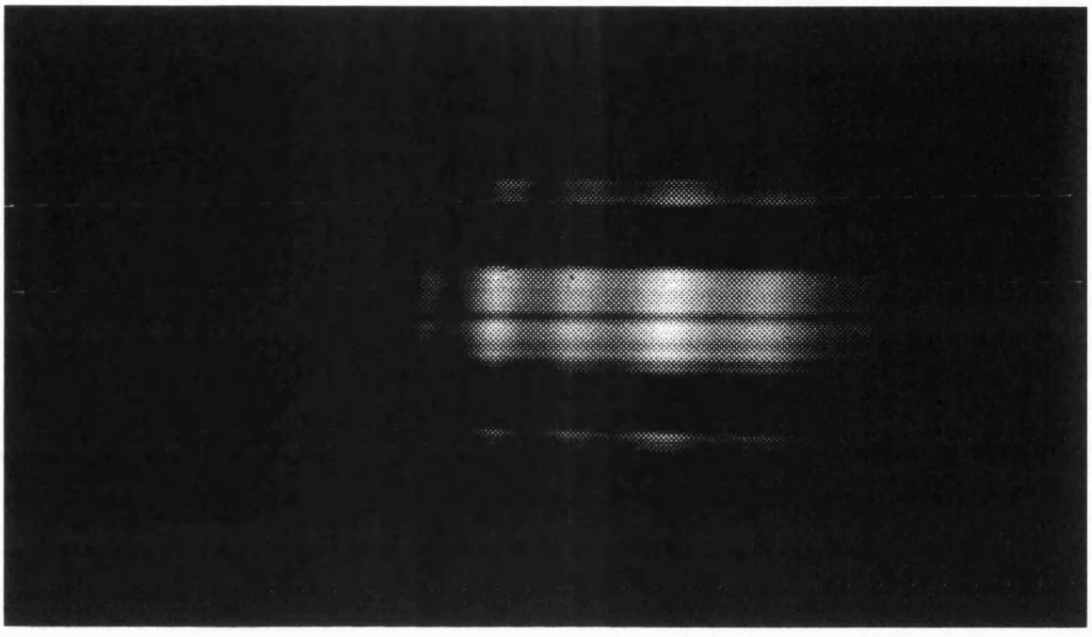

Figure 3.6: Image across a back-illuminated annulus taken using the microscope objective focusing system

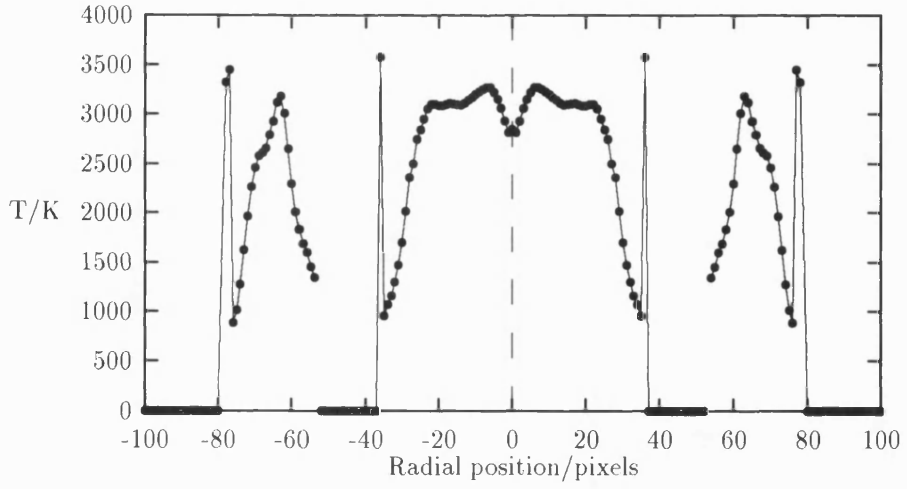

Figure 3.7: Temperature profile resulting from the data set in figure 3.6

profile (figure 3.7) correspond directly to the stripes in the data set (figure 3.6), after the effects of symmetrising have been considered. It does demonstrate however, that the temperature profiles obtained using this focusing system are very susceptible to noise in the original data, since the temperature is fitted directly.

3.2.4 Cylindrical Focusing System

To achieve the maximum vertical resolution in this experiment, it is necessary to have the image as large as possible vertically, while still fitting in the slit horizontally. Using cylindrical optics it is possible to magnify the image in one dimension (vertically) and also reduce it in the other (horizontally); hence the image will cover more vertical tracks on the CCD detector surface than in the circular lens system. This allows more measurements to be performed across the hot-spot, increasing the spatial resolution across the sample. In this system two additional lenses are used, their positions shown in figure 3.8.

To produce as large an image as possible, the circular imaging lens (L_2) is replaced by a longer focal length lens. This lens is still referred to as L_2 since it performs the same operation as in the circular focusing system. The size of the image formed by lens L_2 is found using the equation

$$\frac{D_i}{D_h} = \frac{f_{L_2}}{f_{L_1}}, \tag{3.10}$$

where D_i is the diameter of the image on the slit and D_h is the diameter of the hot-spot (as before). The image is formed at a distance equal to the focal length of

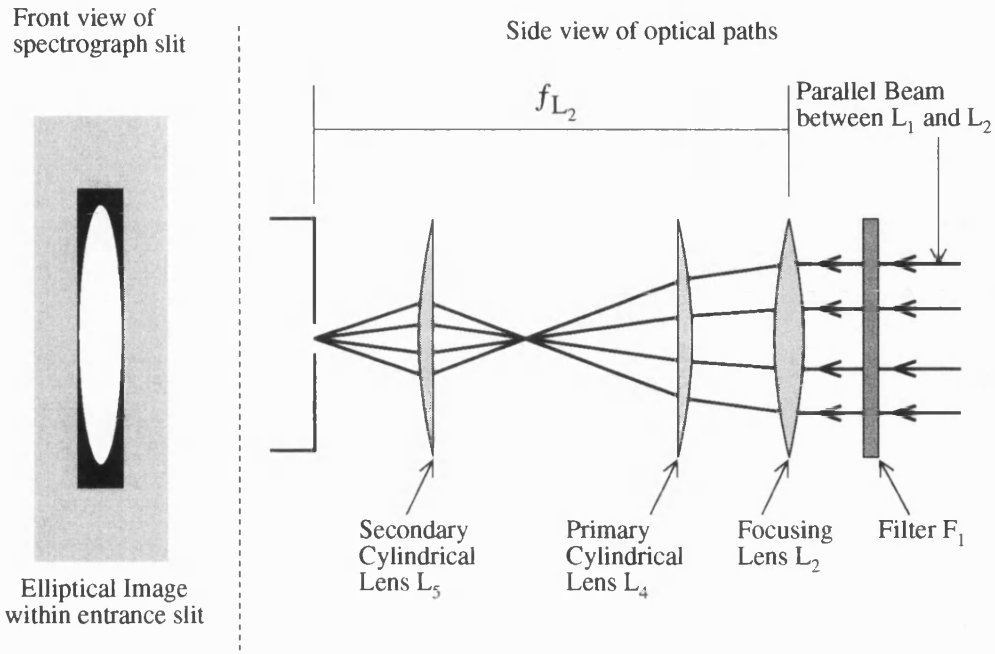

Figure 3.8: Cylindrical lens focusing system forming a vertically magnified elliptical image within the entrance slit.

this new lens. The spectrograph is now positioned as in the microscope objective case (see section 3.2.3), with the centre of the large image coincident with the slit centre. It is important to note here that a long focal length imaging lens (L_2) is used, rather than a microscope objective, as it is necessary to include two further lenses between lens L_2 and the slit. This would not be possible using the objective due to its very short focal length.

To obtain the reduction in horizontal image size, two cylindrical lenses (L_4 and L_5) are positioned as shown in figure 3.8. The longer focal length lens (L_4) provides an intermediate, elliptical 'image'. This 'image' is only focused in the horizontal dimension, since the vertical dimension is unaffected by the lens, and at this intermediate position is not at the focal point of lens L_2. The short focal length

lens (L_5) then forms a horizontally focused, reduced elliptical image coincident with the focal point of the main imaging lens (L_2). This image is contained within the entrance slit of the spectrograph, the minor axis of the elliptical image being less than the slit width, and the major axis being less than the height of the slit.

Since real images are being produced at all stages, geometric optics can be used to determine the appropriate focal lengths and positions for the two cylindrical lenses.

3.2.5 Spectral Image Formation

A near instantaneous, two dimensional spectral image of the sample is required, one possible method to achieve this is the compression of two spatial dimensions into one, replacing the second dimension with the spectral information required (see section 2.4.1). This is performed using a spectrograph in combination with a two-dimensional Charge Coupled Device (CCD) detector system, as shown in figure 3.9.

The focusing optics discussed previously (sections 3.2.2 to 3.2.4) are used to supply the spectrograph with an image which can be spectrally split, for detection by the CCD detector positioned in the spectrograph's focal plane. The actual form of the image on the entrance slit does not affect the operation of the spectrograph/CCD combination, but does determine the methods used to analyse a measured data set (see chapter 5).

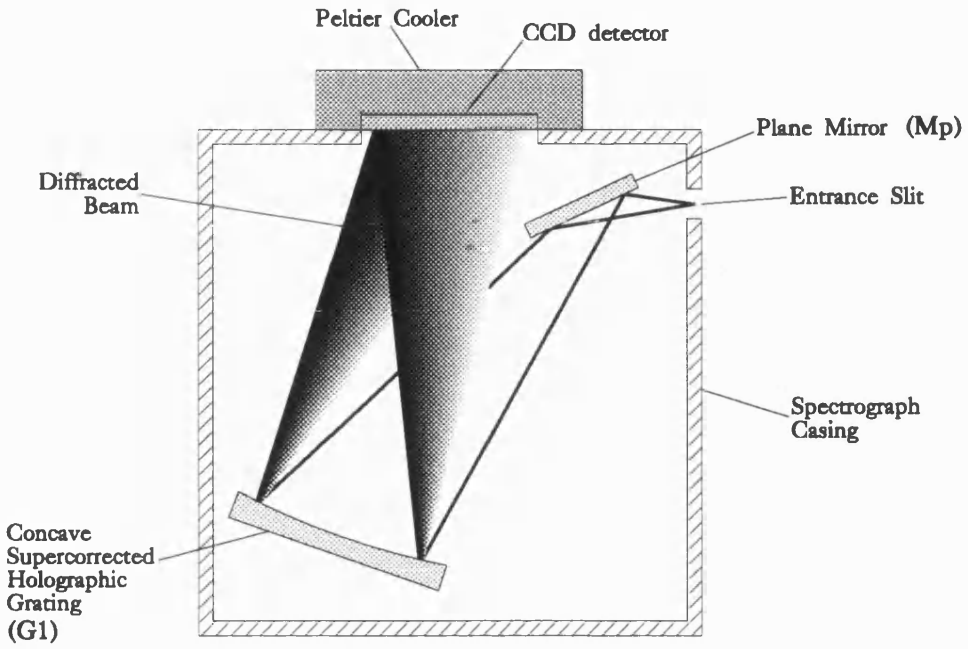

Figure 3.9: Schematic view of the spectral image formation system

3.2.5.1 Spectrograph Operation

The spectrograph is designed to spectrally split a focused image, formed in its entrance slit in one dimension, whilst leaving the other dimension intact. The main component of the spectrograph is a concave, supercorrected holographic grating, which forms a flat spectral image in an image plane. The schematic layout of the spectrograph is shown in figure 3.9.

The operation of the spectrograph can be explained by considering a monochromatic image formed within the entrance slit. A plane mirror (M_p) directs the light from this focused image onto the diffraction grating (G_1). The grating then forms an exact copy (of the image within the entrance slit) in the image plane,

its position along the wavelength axis being determined by the component wavelength of the initial image. This is only possible due to the super-corrected nature of the grating, and is described in more detail in the literature supplied with the spectrograph [34,35].

3.2.5.2 Wavelength Convolution

Considering an incident image composed of two distinct wavelengths introduces the concept of wavelength convolution (smear). The diffracted images are both formed within the image plane of the spectrograph, but are at slightly different positions in the wavelength dimension.

The spectral images at two close wavelengths are diffracted by slightly different amounts, but not enough to separate them completely. As a consequence, both images may be detected by a single CCD pixel. This convolution in the wavelength dimension is illustrated by figure 3.10, the shaded CCD pixels detecting a contribution from both split images.

By making the incident image as narrow as possible, the wavelength smear can be reduced. In the case of the CCD detector used in this experiment, each pixel on the detector surface is 23μm wide. Any incident image narrower than this will therefore be detected by a maximum of two pixels, the amount of smear thus being negligible as 23μm corresponds to a wavelength difference of only 0.5nm (see section 4.4.1). Three slit widths are supplied as standard with the spectrograph used in this experiment: 250μm, 100μm, and 50μm. For most applications the

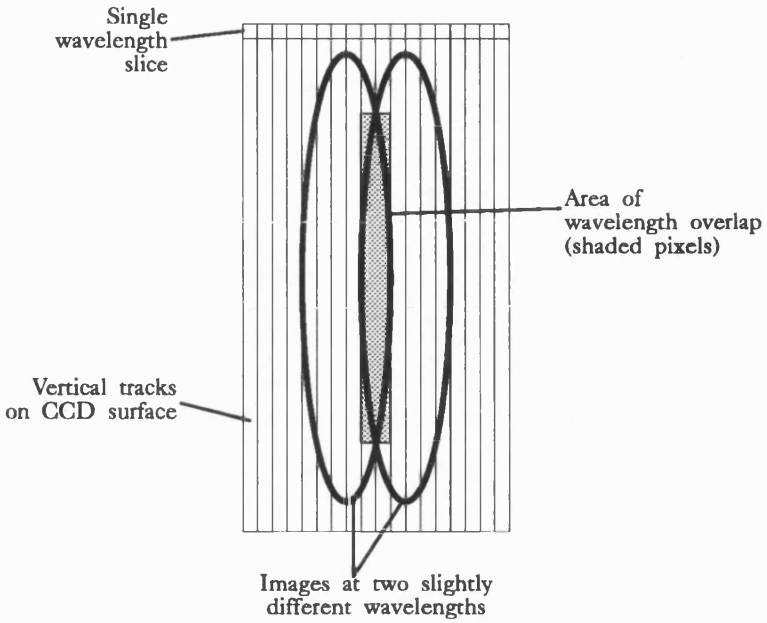

Figure 3.10: Wavelength convolution in the spectral image

50μm slit is preferable since this gives the maximum restriction on the incident image size. An image which fully fills this slit width will be detected (for one wavelength of the split image) by a maximum of three CCD detector pixels. In most cases the full image will cover a width of 250–300 pixels, so the overlap will only be of the order of 1% of the image dimension. Another consideration is that for Planck distributed data, the difference in expected intensities at wavelengths 1.5nm apart will be extremely small, so the effect of wavelength smear can be discounted for narrow slits. For wide slits some correction for wavelength smear would be required, since a single wavelength image may be detected by a large number of CCD pixels.

3.2.5.3 Spatial Resolution

The number of radial positions at which a temperature may be measured is determined by the number of CCD slices the spectral image covers. The diffraction grating G_1 forms a spectral image with the same height as the focused image within its entrance slit. To produce a large spatial resolution, it is necessary to form a large image in the spectrograph entrance slit which, when spectrally split, covers the maximum number of CCD slices possible. The dimensions of the hot spot on the sample are fixed, being determined by the focal length of lens L_1 (see section 3.1). Improved spatial resolution is achieved by using magnifying optics to form an enlarged image of the hot spot within the entrance slit (see sections 3.2.2 to 3.2.4).

3.2.6 Image Recording System

The image formed by the spectrograph is recorded for subsequent analysis by a computer controlled, two-dimensional CCD detector, as illustrated in figure 3.9. To allow a focused image to be recorded, the detector face is positioned coincident with the imaging plane of the spectrograph. For this experiment the CCD detector forms part of an Optical Multichannel Analysis (OMA) system manufactured by EG&G Instruments.

The CCD is a model 1430-P, two-dimensional array of silicon detector pixels, each one 23μm square. The full face is made up of 576×384 such pixels, creating an imaging area of 13.25mm×8.83mm, as quoted by the manufacturer. The correct

active area exposure time is controlled by an electro-mechanical plane shutter (with a minimum of 10ms), which allows measurements on comparatively cool samples (hence low light emission) and also time resolved images by repeated, short exposure imaging.

The silicon detector face is mounted directly onto a Peltier cooler to reduce the dark count, and is normally operated at between -15°C and -5°C. To reduce water condensation and ice build up, the entire detector chassis is flushed with nitrogen gas (at approximately 1.5litres/min). This helps to prevent dark and light spots on the image being recorded by the detector (as discussed in section 5.2). The main body of the Peltier cooler is cooled by a water jacket, the flow rate through the jacket being set at approximately 100cm^3/min.

The CCD detector cooling, shutter and signal digitisation are controlled by a model 1430-1 detector controller using a 14 bit analogue–digital converter giving a range of 16384 intensity levels. Signals are passed to and from the detector via a model 1464 scan control interface, using GPIB communication with a 386 based PC. The entire system is then controlled from the OMA operating software supplied by EG&G with the detection components.

3.2.7 Form of Measured Data

The experimental data recorded by the CCD detector is a two-dimensional image; one dimension gives spatial information and the other gives spectral information. This image is generated from the focused image in the spectrograph entrance slit,

and has certain attributes that become significant during the mathematical analysis of the surface temperature distribution. The horizontal lines in the data set are referred to in this text as *wavelength slices*, and correspond to the wavelength spectrum obtained from a particular strip integral at a given vertical position within the data set. The vertical lines are referred to as *vertical tracks*, and correspond to the set of strip integrals across the entire spectrograph slit at a particular wavelength. By considering a particular track the spatial distribution of emitted light at a given wavelength can be determined.

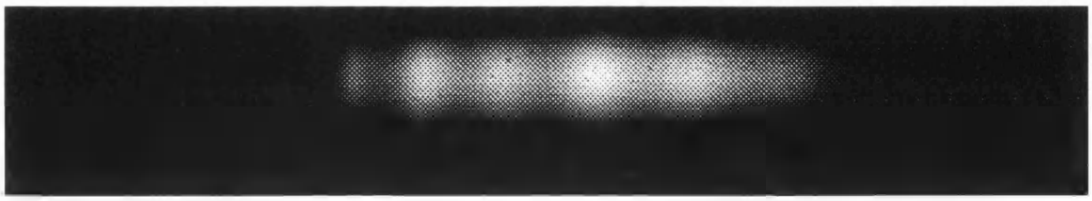

Figure 3.11: Example data set showing the horizontal wavelength slices and vertical tracks.

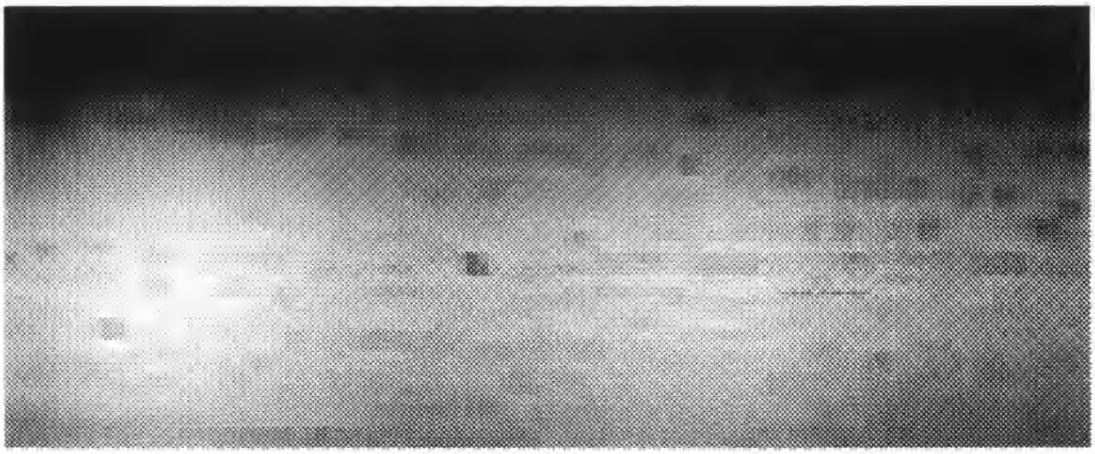

Figure 3.12: Enlarged section of the data set imaged in figure 3.11.

Figure 3.11 shows the complete spectrally split image of a laser heated spot. Most of the data set is zero, as indicated by the large expanse of black in the image,

and it is important that any analysis ignores these areas, since including them would require a significant amount of extra computation. The data in this image has been scaled to make the maximum data values appear white.

Expanding the image to concentrate on a small region of the data set makes the individual pixels in the data set visible. This allows the separate slices and tracks of the image to be seen.

3.3 Sample Containment

The object of the experiment is to measure temperature profiles of samples heated to very high temperatures. At such high temperatures many samples are prone to oxidation or vaporisation: it may be necessary to contain the material within a reducing atmosphere during the heating process. The type of reducing gas used is dependent on the characteristics of the material being investigated; this is discussed with the relevant sample information in chapter 8.

3.3.1 Controlled Atmosphere Chamber

The Controlled Atmosphere Chamber (CAC) is a sealed sample container which has been designed with two main specifications. Firstly, to prevent surface oxidation, it must enable suitable reducing gases to be passed over an experimental sample contained within it. Secondly it should allow samples to be removed and re-mounted in the same position, eliminating the need for refocusing of the lens L_1

for each new sample under test.

The CAC is an air tight container with two gas inlets: one used to pass gas into the chamber, and the other to take exhaust gas out. An important feature of the outlet is that is prevents the reducing gases being released into the laser room, since some reducing gases contain proportions of hydrogen (requiring that the gas be efficiently removed from any source of heating), or carbon monoxide. To allow easy removal and repositioning of samples, they are positioned on a special mount fixed to the lid of the box. The main part of the box is then fixed in position longitudinally along the axis of the laser beam, but mounted on an x-y positioning stage to permit different areas of the samples to be examined. A schematic diagram of the CAC on the translation stages is shown in figure 3.13.

The CAC is made from an aluminium alloy diecast box with a sealed lid. Two quartz windows are mounted into the casing of the box: one in its base, and the other in the lid. The window in the base allows the sample to be heated by the laser and the temperature on the front face to be measured; that in the lid allows measurements on the rear, unheated face of the sample to be performed. The windows are mounted with neoprene seals in the box–window and window–face plate interfaces to form air tight interfaces as illustrated by figure 3.14. Two mounting bolts are then used to clamp the face plate and the windows firmly onto the box casing, and the interfaces coated with silicone rubber to improve the efficiency of the neoprene seals.

The sample mount is a more complex structure than the window seals, and is designed to position the sample under test at the exact focus of the lens L_1. It

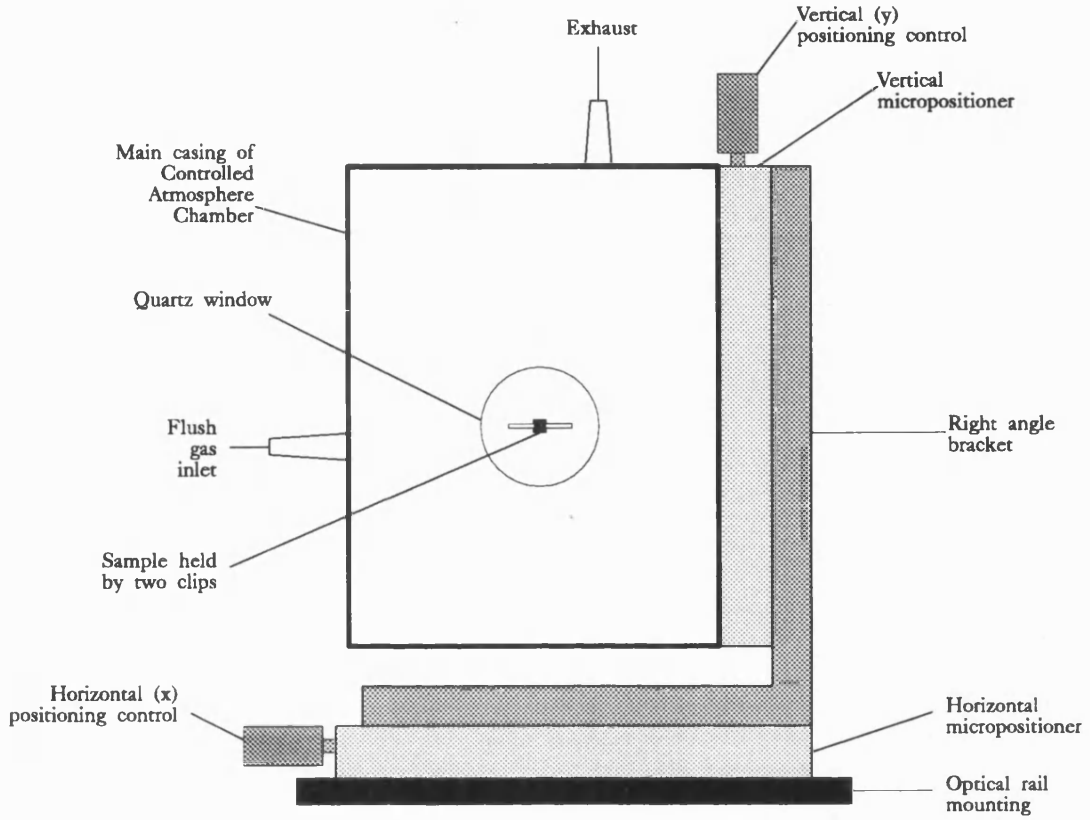

Figure 3.13: The Controlled Atmosphere Chamber (CAC) for sample containment (side view, i.e., looking along the axis of the laser beam)

allows different samples to be mounted without the need for refocusing. To achieve this, special plates are mounted onto the lid in such a way that when the box is closed the plate surface lies at a fixed distance from the front face of the CAC. Once initial focusing has been performed on a sample, another specimen can then easily be mounted in the same position, the laser having been already focused onto its front face. The plate mounting is demonstrated in figure 3.15, the four posts being mounted onto the lid with neoprene seals in a similar fashion to the quartz windows.

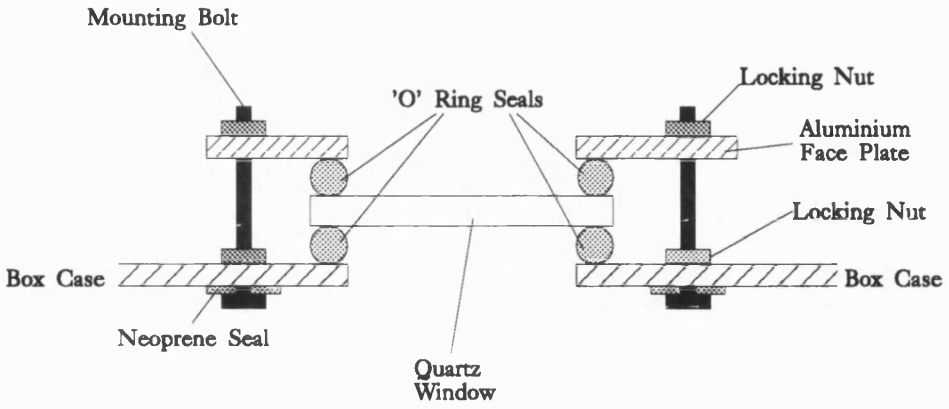

Figure 3.14: Air-tight neoprene seals between quartz windows and box

Although all the interfaces on the box are sealed, to ensure that there are no leaks of oxygen from the atmosphere into the main casing, the CAC is always operated at a positive internal pressure, i.e., any leaks will be of the reducing gas out into the atmosphere. This positive pressure is maintained using a bubbler, the rate of gas flow being increased until a steady stream of bubbles is observed.

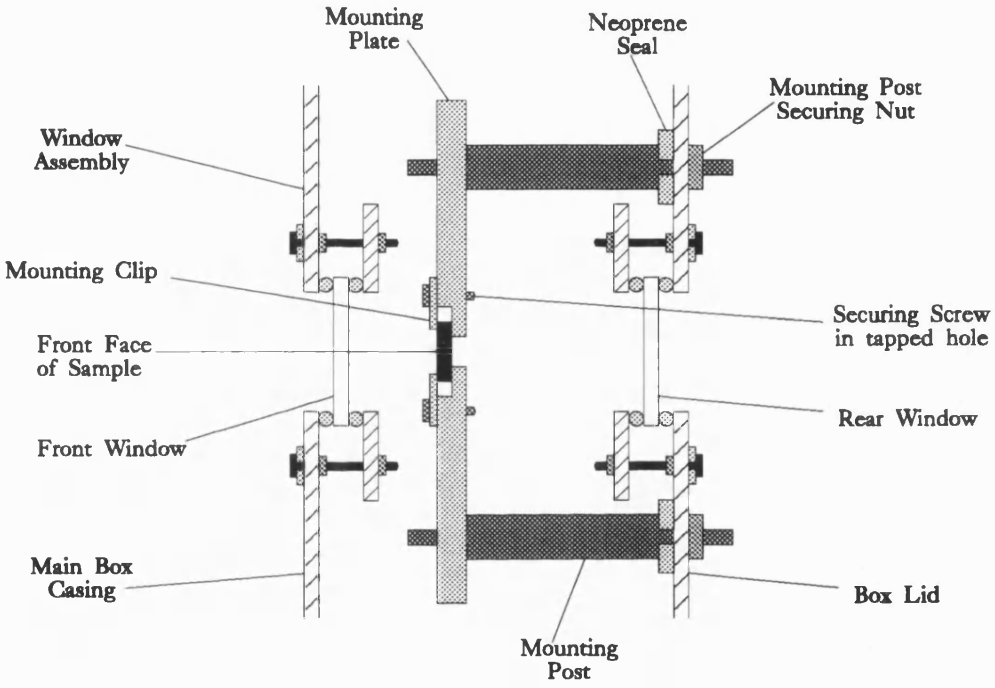

Figure 3.15: Sectional view of sample plate mounting in the CAC (two further mounting post are concealed behind the two shown).

Chapter 4

System Alignment and Calibration

Before any measurements can be taken it is necessary to align the optical components and calibrate the overall system. These are two distinct stages, with the calibration being performed once all alignment processes have been completed. It is also important to check that the laser is producing an axially symmetric spot on the sample and hence will induce a symmetric temperature profile.

4.1 Beam Profiling

In all stages where information on the laser beam shape is required an Optilas model 2180 beam profiler with High Power scan head is used. This consists of a fixed silicon detector array surrounded by a cylinder with a 5μm wide slit cut parallel to the cylinder axis. While measurements are being made, the cylinder is rotated about its axis, causing the slit to be scanned across the detector face.

The image obtained using this method is not a two-dimensional intensity map, but rather a set of finite width strip integrals across the beam. The beam profiler can therefore only be used to produce cross-sectional profiles, or "side-on" views. This is similar to the way in which spectral data from the heated sample is taken (see section 3.2).

The profiler mounting is constructed to allow the head to rotate between 0° and 90° to the horizontal, about an axis normal to the detector face. A set of cross-sectional profiles can be measured for selected profiler-head orientations, and the overall shape of the incident beam can be inferred. Since the mathematical analysis of the temperature profile assumes axial symmetry of the two-dimensional surface temperature distribution, this application of the profiler is used to check for beam symmetry.

The measured cross-sectional profiles reflect any symmetry present in the two-dimensional intensity distribution. The simplest case to consider is a line of symmetry in the incident beam intensity. A profile taken at a head orientation parallel to such a line will also be symmetric, whereas another angle will not be symmetric (these two cases are illustrated in figure 4.1).

The general rule for detecting symmetry is that the line integrals through the two-dimensional point distribution are equal at equal distances from an arbitrary line, i.e.,

$$\int_{\ell} f(p,\theta) = \int_{\ell} f(-p,\theta) \tag{4.1}$$

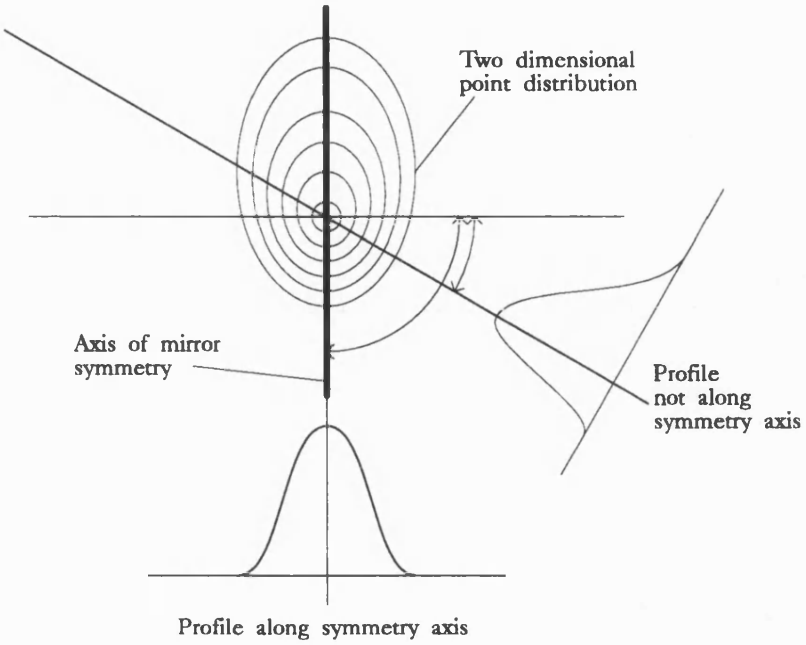

Figure 4.1: Side on profiles measured by beam profiling apparatus, with reference angles to the lines of symmetry present in a two-dimensional intensity distribution.

where $\int_\ell$ is the line integral along any line ℓ parallel to the scan head orientation θ and at a perpendicular distance p from the arbitrary line of symmetry. Verification of axial symmetry requires that all profiles which may be measured are laterally symmetric, since all lines passing through the centre of symmetric distribution are mirror planes. It is also necessary that the profiles are identical in shape (height and width) as this excludes distributions containing a point of inversion (where $f(-x,-y) = f(x,y)$ in Cartesian coordinates and hence $f(-r,\theta) = f(r,\theta)$ in radial coordinates).

In most stages of the alignment process the beam profiler is used to check that the laser is producing a circular beam with a Gaussian irradiance profile. For this a set of beam profiles are taken with the detector-head at a selection of angles

between 0° and 90° to the horizontal, the profiles then being compared as above to determine the existence of axial symmetry in the incident beam.

4.2 Alignment

The alignment process can be subdivided into two parts. The first involves setting up the laser focusing system to provide a suitable heating spot on a sample surface. The second part then uses this heating system to enable the temperature measurement and image focusing optics to be aligned.

4.2.1 Laser Focusing

The first optical component to be checked is the heating laser itself. As stated previously it is necessary for the laser to be producing a Gaussian (TEM_{00}) beam for a single, axially symmetric temperature peak to be generated. The beam profiler is therefore placed after the exit aperture of the laser and a set of profiles taken for angles between 0° and 90°. These profiles can also be used to calculate the beam width as it emerges from the laser, this value being used in the determination of the spot diameter on the sample surface. If the beam is not symmetric, and hence is not operating in the Gaussian mode it is necessary to realign the laser by altering the positions of the end mirrors and the mode selection apertures. This process is discussed in the relevant operational manuals for the laser.

After the laser operation has been verified it is necessary to position and align

the beam expander. To avoid distortion or misdirection of the laser beam, the beam expander axis must coincide with the optical axis of the beam: the beam passes through the optical centres of the lenses used to construct the expander, and emerges with its optical axis unchanged.

If the expander axis is at an angle to the incident beam axis, the emerging beam has an altered optical axis (i.e., the beam is deviated), and a coma is observed on the profiler. By taking measurements with the beam profiler head set at different scanning angles to the horizontal, the angle at which the coma is most evident is found. To determine the extent of misalignment of the beam expander, the head scanning angle is set to this angle of maximum coma. A set of profiles are then taken with the profiler positioned at different distances from the exit aperture of the beam expander, the profiler movement being maintained parallel to the axis of the laser beam. Since the emerging beam axis is not parallel to the laser axis, the position of the beam on the profiler head will move. The distance the beam axis moves for a given profiler displacement is used to calculate the angle of the beam axis to the laser axis by standard trigonometric analysis. When the expander axis is parallel to the beam axis, the profile of the emerging beam has the same shape and symmetry as the incident beam, with its diameter increased by a factor of 10, since a 10:1 beam expander is used in this system.

The final alignment process is to ensure that the focusing lens (L_1) is centred on the beam axis, and is perpendicular to the beam. This is a complicated procedure since the angles of the two beam guiding mirrors (M_1 and M_2) must also be checked. The focusing lens position for this particular system is fixed, so the mirrors must be used to guide the beam through lens L_1 at the correct angle.

A similar technique to the expander positioning is used where a set of profiles is taken at different displacements from the focusing lens. The mirror angles are adjusted to give a beam coincident with the optical axis of the focusing lens (L_1). This condition is met when the position of the beam on the profiler is unchanged with profiler displacement.

4.2.2 Collection and Image Formation Optics

When aligning the light collection and image formation optics, it is essential that they are set up to examine the same area of sample surface heated by the laser. To achieve this, an artificial sample has been made by melting a small diameter hole through a thin steel shim. The shim is placed at the focal point of the lens L_1, and the laser power increased until a small hole appears. This is seen as a sudden decrease in light intensity being emitted by the sample surface, since the laser passes through the hole and there is no heating of the sample.

With the laser turned off and a small screen placed over the exit aperture of the laser, a diffuse light source is placed behind the shim hole. This source is positioned such that a small light spot is observed on the screen, coincident with the centre of the exit aperture of the laser. This ensures that the light source is in the same optical path as the laser beam. The light passing through the holed shim from the diffuse source can then be used as a suitable image to align the detection optics.

Before any lenses are added to the system a screen is erected on a moveable stage,

positioned after the filter (F_1 in figure 3.2). The central position of the light spot passing through the shim is marked on this screen and this can then be used as a reference point for the optical axis of the lens systems. This screen can be moved longitudinally along the optical axis of the system and any lenses added can be positioned to form a new image coincident with the mark, ensuring alignment of all optics to the same axis. Another useful technique in the positioning of the spectrograph uses one of the spectrograph slits with a thin paper screen attached to the outer surface. This special screen can be used to locate the correct longitudinal position of the slit (parallel to the light optical axis) where a focused image is formed. A standard slit can be substituted to find the exact lateral (x–y) position, ensuring that the image is centred on the slit. The actual alignment process now depends on the type of optical system used for the experiment, the three cases introduced in sections 3.2.2 to 3.2.4 being discussed in turn.

4.2.2.1 Circular Focusing System

This is the simplest system to align since there is only one lens that needs to be positioned (L_2 in figure 3.3). This lens is adjusted to give a circular image of the shim hole on the movable screen, which is placed in the plane where the spectrograph entrance slit is to be. The spectrograph must now be manoeuvred into a position such that the image formed by the aligned lens (L_2) falls entirely within the entrance slit. The entrance slit should be chosen such that it is just wider than the image, since this reduces the possibility of wavelength smearing in the final spectral image (see section 3.2.5) while retaining the axial symmetry of the final image.

4.2.2.2 Microscope Objective

This system uses an extra lens (L_3 in figure 3.4) after the main imaging lens used in the circular optic system. Once the circular lens system has been aligned it is a simple process to align the extra lens for this system. Again, the movable screen is used in the plane where the spectrograph entrance slit is to be positioned; however in this case it cannot be fixed beforehand since the distance of the second, magnified image will depend on the location of the lens L_3 (see the discussion of this system in section 3.2.1).

The objective lens is located further from L_2 than the intermediate image, since the objective requires a real image to magnify. The lens and the screen should therefore be moved until a circular, magnified image of the shim hole is observed, with its centre coincident with the centre of the unfocused beam (marked on the screen). This image should be no larger than the vertical dimension of the spectrograph slit to ensure that there is no loss of edge information.

The spectrograph is positioned such that the focused, enlarged image formed by lens L_3 is coincident with the spectrograph slit. The actual horizontal positioning of the slit is not crucial since this focusing system can be used to examine any line across the image. It is more useful to measure across a diameter, enabling a peak temperature measurement to be made. If the image is very large, it may be necessary to measure along a line some distance from the centre to maintain the image vertically within the slit. For this microscope objective system the smallest slit should be chosen to reduce the wavelength smear to a minimum.

4.2.2.3 Cylindrical Focusing

This is a more complex system to focus as it requires the correct positioning of three lenses. To begin with, only the lens which replaces the original imaging lens (L_2 in figure 3.3) is positioned, the two cylindrical lenses being omitted from the system. This lens and the movable screen are positioned to produce a slightly magnified image with a centre coincident with that of the original, unfocused spot which was marked on the screen. The distance between the lens and the screen should equal the focal length of lens L_2, since lens L_2 is used to form a focused image from a parallel beam. As stated in section 3.2.1, it is necessary to have enough distance between these two optical components to put two cylindrical lenses in the lens–screen gap.

After the imaging lens has been aligned, the primary cylindrical lens (L_4) can be positioned. Initially, only its horizontal placement can be aligned, since the final slit image can only be viewed when both mirrors are in place. This lens forms a very wide elliptical image on the movable screen which is not in focus horizontally. At this stage it is only necessary to position the centre of this 'image' coincident with the marked spot. Since the cylindrical lens does not form a fully focused image on the screen, it is impossible to use the presence of coma to detect axis misalignment. Therefore to ensure that the lens is perpendicular to the optical path, the centre of the elliptical image must be measured with the cylindrical lens at various positions between the lens L_2 and the screen. Any misalignment becomes evident as the image moves horizontally, as illustrated in figure 4.2. A more accurate alignment is produced with the lens as close as possible to lens L_2 since this gives the maximum path length for beam deviation.

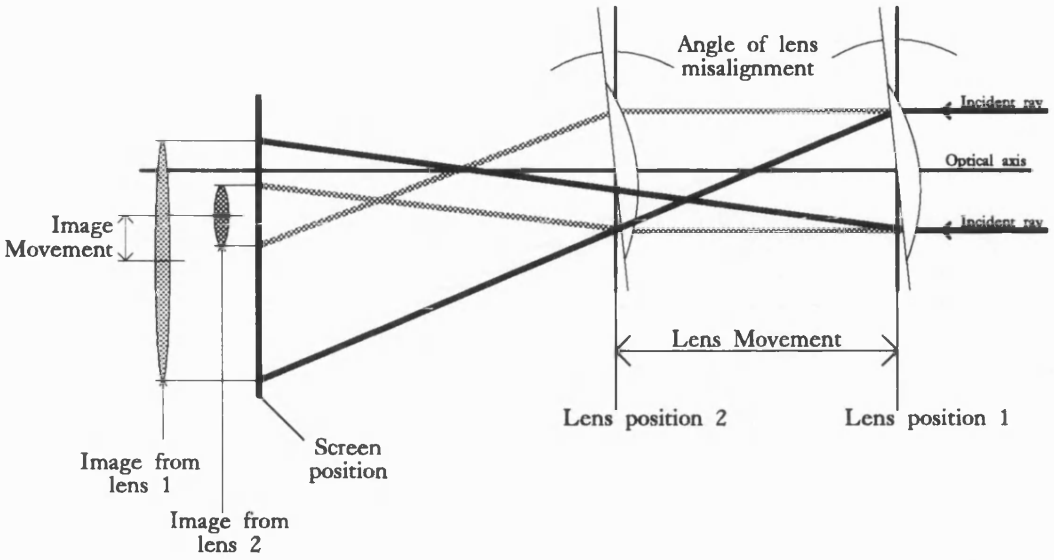

Figure 4.2: Movement of the elliptical image with misalignment of the primary cylindrical mirror.

When the primary cylindrical lens is aligned horizontally, the final imaging cylindrical lens (L_5 in figure 3.8) may be added to the system. The horizontal positioning of the lens must be set first, in a similar manner to the primary lens (L_4). Lens L_5 must not be positioned too close to lens L_4 during the alignment, since it is intended to form a reduced image of the intermediate image focused by lens L_4. A hand held screen is used to locate the intermediate image. The lens (L_5) is positioned such that the elliptical 'image' is formed coincident with the marked spot on the screen, again ensuring that the image does not move with longitudinal position of L_5 (in a similar manner to that described for lens L_4).

Once both cylindrical lenses are centred and fixed with their principle planes perpendicular to the system optical axis, they can be positioned longitudinally (along the optical axis) to form a focused, elliptical image within the spectrograph entrance slit. To reduce the amount of wavelength smear in the spectral image, it

is necessary to form the narrowest possible image horizontally. Therefore the two cylindrical lenses must be positioned to produce the maximum reduction factor available.

4.2.2.4 Changing Focusing Systems

Each time the focusing system is changed, a different alignment procedure needs to be performed. Therefore it is prudent to perform all experimental measurements using one system only, as this removes the need for constant re-alignment. The cylindrical focusing optics are used since they produce a much improved vertical resolution while still maintaining the entire spot image within the slit, and hence do not ignore any of the spectral information obtained from the hot-spot.

4.2.2.5 Vertical Magnification Factor/Spatial Resolution

The different focusing optics produce widely different focused images in the spectrograph entrance slit, some of which (for example the cylindrical system) magnify the image vertically. It is necessary, before any thermal properties can be calculated from the temperature profile, to determine the spatial resolution achieved. The actual magnification of the system can be determined theoretically using the optical properties of the lenses (see section 3.2.1 for an example for the circular lens case); however it is sensible to verify this magnification factor. This is a simple process since a known radius sample is being examined. A spectral image of the sample is taken, and the number of vertical tracks the image covers

counted (n_t). The actual dimension of the hole in the shim (r_h) can be measured using a travelling microscope, or using a Scanning Electron Microscope (SEM). The magnification factor is then determined from:

$$M = \frac{23 \times 10^{-6} \cdot n_t}{r_h} \tag{4.2}$$

where all dimensions are in metres, and 23×10^{-6} is the vertical height of each CCD pixel.

4.3 Qualification of the Laser Beam

The mathematical analysis used for determining the temperature profile generated on the sample surface assumes that the temperature has an axially symmetric distribution (see section 5.6). To generate such a distribution, it is necessary for the heating induced by the laser to also be axially symmetric. The laser is operated in the Gaussian TEM_{00} mode since this has a symmetric shape and a single intensity maximum at the beam axis, which will produce a single maximum in the temperature distribution.

As part of the quality assurance procedure for an experimental system used to provide data for use in other systems and theoretic models, it is necessary to qualify that the system is operating to the specified requirements. Therefore a set of beam profiles must be taken and compared with those expected for an ideal system, ensuring that the optical system is providing a heating spot which has a shape suitable for the mathematical analysis of any experimental data.

4.3.1 Two-dimensional Profile

The profile of the focused laser spot must be axially symmetric for all laser powers that may be used for sample heating. To verify this, the scan head is positioned at the focal point of the lens L_1. A complete set of profiles for scanning head angles between 0° and 90° are then recorded at various laser power settings between threshold and maximum. Profiles are recorded approximately every 10°, corresponding to a set of 10 cross-sections for each power setting. For the laser used in this experiment, the flash lamp current varies between 21A and 36A (approximately 5W and 16W); however at high powers it is necessary to attenuate the output laser power using neutral density filters to avoid damage to the detector array. For each laser power setting the angle profiles are compared to ensure that the width and height of the intensity distribution is consistent, and hence axially symmetric (see section 4.1). The overall beam width and height can then be calculated from the profile sets. Figure 4.3 shows the relationship between the beam waist (width) and the scan head orientation for an arbitrary power setting and the 70mm focusing lens (described in section 3.1).

The heating system alignment process involves setting the mirrors and lenses such that the output heating pulse is axially symmetric; however it is prudent to verify that the system is still aligned once all the collection and focusing optics have also been aligned.

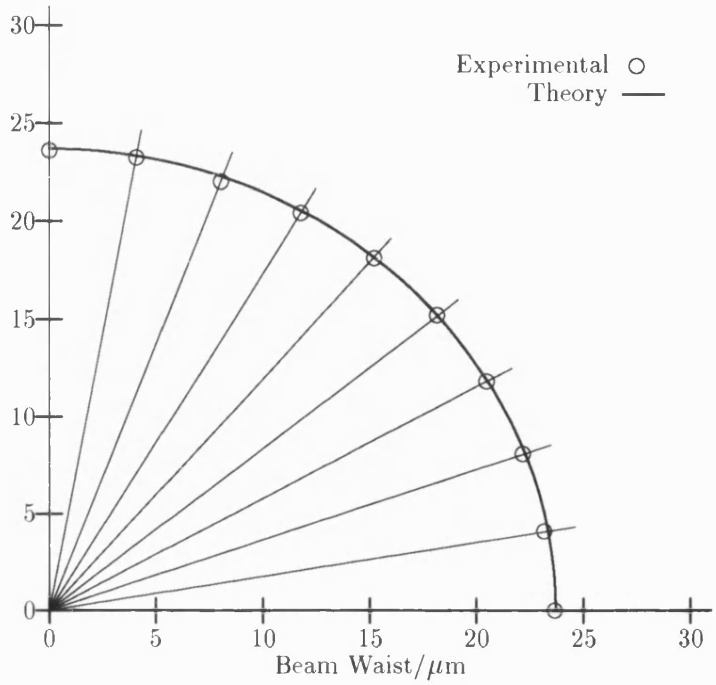

Figure 4.3: Beam width as a function of scan head angle for the 70mm focusing lens (Theory line corresponds to beam waist of 23.70μm from table 3.1).

4.3.2 Gaussian Beam Parameters

Once the profile at the focus has been qualified, the parameters governing the Gaussian beam propagation can be determined. The scan head orientation is now unimportant since the previous stage confirmed that the beam is axially symmetric. The profiler is now used to measure beam cross-sections at various distances from the focusing lens L_1. From these sections, beam width and height can be determined as a function of longitudinal distance along the optical axis of the beam, and a value for the beam waist determined. Figure 4.4 shows a typical set of data for the beam head positioned at various distances along the optical

axis of the laser beam. The graph shows the beam width at the 13.5% peak height level, together with the theoretical beam width given the optical characteristics quoted in section 3.1. The particular curve shown here is for the 7cm focal length case. The horizontal axis is given in terms of the micropositioner reading on the optical bench upon which the profiler was mounted, the beam waist being observed at 109.8mm.

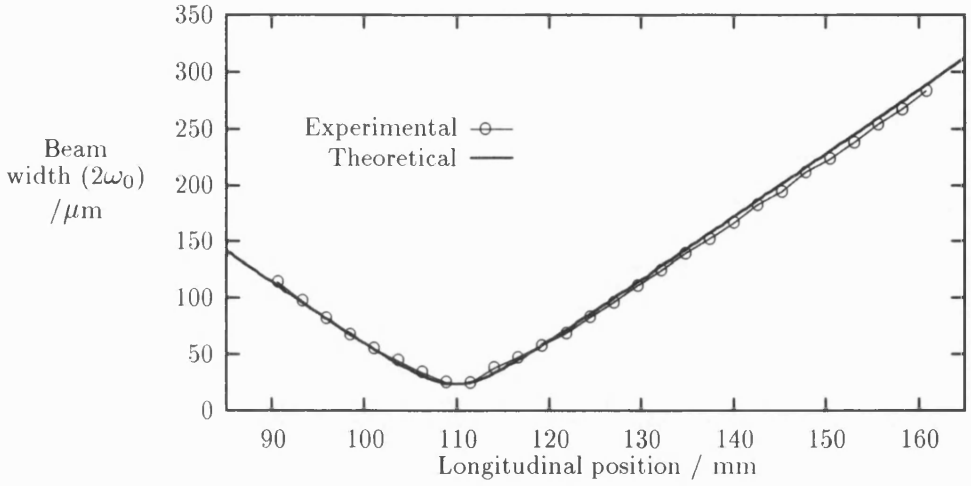

Figure 4.4: Beam width as a function of longitudinal distance from L_1.

4.3.3 Time Stability

For a stable temperature distribution to be generated on the sample surface it is necessary for the heating to be stable with respect to time. The beam profiler used in this experiment can record the time development of beam intensity profiles. These can then be used to determine any time variation of heating spot width, intensity and position with time. Since the previous qualification stages have

confirmed the axial symmetry and Gaussian nature of the beam, the beam head can be positioned anywhere along the longitudinal axis (provided the beam is not wider than the detector), and at an arbitrary head orientation. Figure 4.5 shows the time dependence of the peak height both with and without the laser stabiliser.

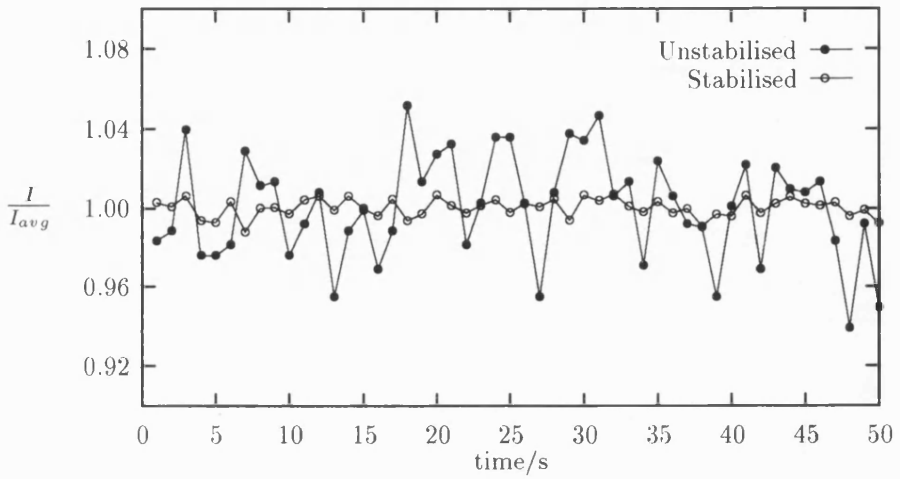

Figure 4.5: Laser beam peak height variation with time

4.4 Calibration

Once the optical systems are fully aligned it is necessary to calibrate their physical properties. Two separate calibration procedures need to be performed before any experimental measurements can be analysed. These ensure that the data recorded on the CCD detector can be converted correctly into the absolute units required by the mathematical analysis process. The first calibration procedure determines the wavelength of light detected by any specified pixel position on the CCD detector. This calibration is used in the temperature fitting stage of the

analysis (section 5.7). The second calibration procedure determines the spectral response of the optical system. As the optical components of the system do not have uniform spectral transmission coefficients, the intensities measured by the CCD are not the absolute values emitted by the sample itself, but values modified by the optical components. Each individual component has its own transmission characteristics, but the overall response is a linear combination of all of these. The spectral calibration is used to calculate a set of correction coefficients to convert the experimental intensity data into absolute values.

4.4.1 Wavelength

A mathematical method is required to enable the pixel position at which experimental data is recorded to be converted to a corresponding wavelength. The spectrograph is designed using a concave, super-corrected holographic grating to produce a linear wavelength spread horizontally across the two-dimensional plane image formed at its focus, the spread being determined solely by the grating employed. The spectrograph used in this experimental system is a Jobin-Yvon CP200 with a grating ruled at 200g/mm. This gives a corresponding wavelength spread of 190nm to 820nm over an image width of 25mm, and a resolution of 25.2nm/mm. The CCD detector is positioned coincident with the focal plane of the spectrograph, however its horizontal position relative to the spectral image determines the pixel–wavelength relationship (see section 3.2.5). Assuming that the image to be analysed spectrally is formed directly in the entrance slit of the spectrograph, the CCD position is the only determining factor in the wavelength calibration. In most experiments the long wavelength end of the spectrum is of

the greatest interest as this is where the peak in the spectral irradiance occurs, and hence is where the most accurate information about the temperature can be found. The CCD is therefore positioned to detect the long wavelength end of the spectral image.

A theoretical value for the wavelength dispersion can be calculated from the physical dimensions and arrangement of the spectrograph/CCD combination. The spectrograph produces a wavelength resolution of 25nm/mm at its focal plane assuming a 200g/mm grating is used. The CCD surface is positioned in this plane, and has an active array of 13.25mm×8.83mm, consisting of 576×384 pixel elements, each one 23μm square (including a thin, non-detecting separator zone). The active area covers only half of the 25mm wide spectrograph image and so a portion of the spectral image can be selected, depending on the particular range of wavelengths required for the experiment, by positioning the array at a specific position across the image in the plane. The range of wavelengths detected by a CCD pixel is determined from the dispersion value for the spectrograph, and for a 23μm pixel gives 0.5797nm. Therefore this is the minimum resolvable wavelength difference. Since the CCD surface is movable with respect to the image, a theoretical value can only be calculated for the wavelength difference between pixels. To determine the actual wavelength detected by each pixel on the CCD surface, a wavelength calibration is required to calculate the 'base wavelength', or the shortest wavelength detected by the CCD at its selected position on the image.

The experimental system used for the calibration is the same as that for measuring actual temperature data, without laser heating. The sample is replaced by a

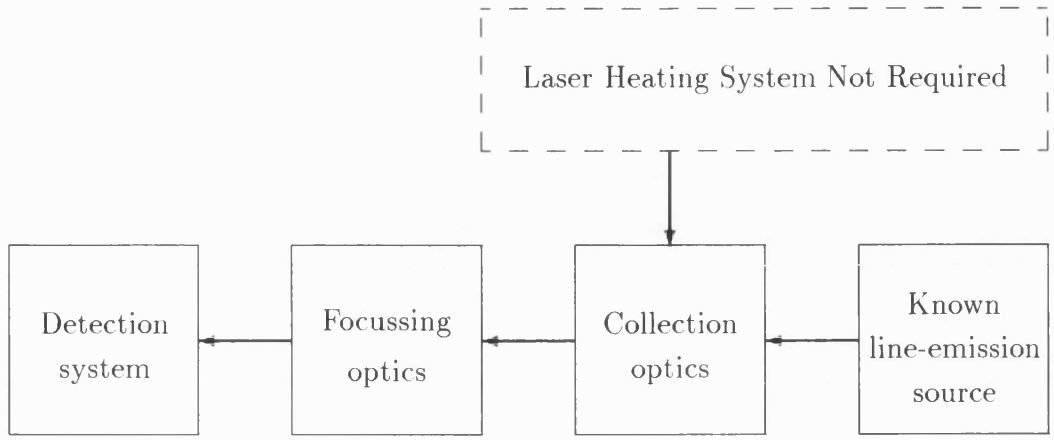

Figure 4.6: Schematic view of the optical system used for wavelength calibration

known line emission source, as illustrated in figure 4.6. Any of the focusing systems previously discussed may be used since they do not directly affect the positioning of the spectral image on the CCD surface; however it is wise to use the same system as that for actual experiments to avoid discrepancies in the optical paths. The smallest spectrograph entrance slit must be used for the calibration procedure to reduce the possibility of wavelength overlap (section 3.2.5). The spectrograph used in this experiment has a selection of three slits: 250μm, 100μm, 50μm. As an example of the overlap that may be observed, two data sets are shown in figure 4.7 for the 50μm and 250μm slits, both being taken using a single HeNe laser as the input source. The diagram clearly shows that the HeNe line is spread over ten vertical CCD tracks for the 250μm wide slit, whereas the 50μm wide slit is concentrated on one vertical position with a small spread to the sides. These values suggest a pixel width of approximately 25μm, which agrees with the actual pixel size of 23μm.

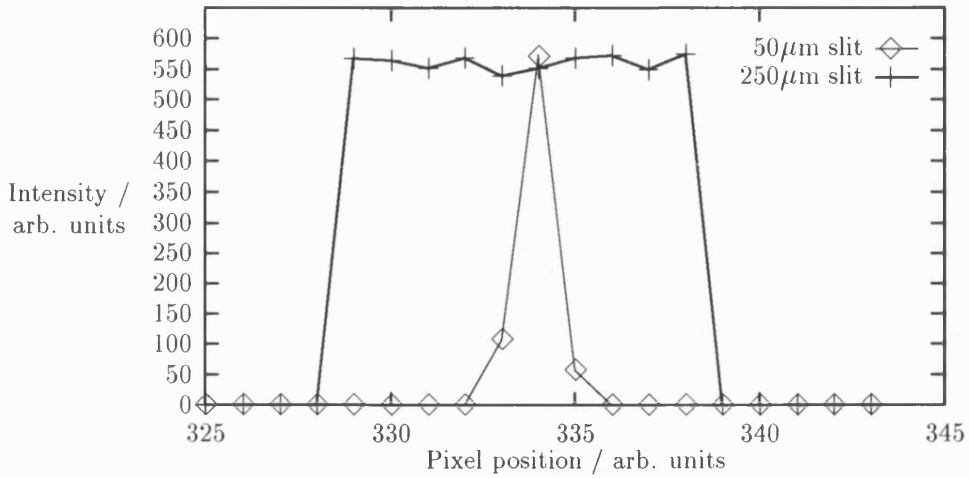

Figure 4.7: Comparison of 50μm and 250μm wide slits for the single 633nm red line of a HeNe laser.

The source is positioned such that the resulting image on the slit is as large as possible; however it need not be at the focus of the collecting lens L_1 since spatial analysis of the source is not required. There is also no requirement for the image to be formed entirely within the slit, again because no spatial analysis is to be performed. However it is advantageous to have an image as tall as possible (within the limits of the height of the slit) as it will then cover the maximum number of CCD tracks and allow many separate calibrations to be performed and compared.

Typical sources used in the calibration procedure are: a HeNe laser (red 632.8nm line), a Hg vapour lamp (550nm and the 578nm doublet), a Cd discharge lamp (509nm and 660nm). These readily available sources in particular are used since they have sharp emission lines. Figure 4.8 shows the wavelength spectra for these lines, superimposed onto one set of axes. In some cases (especially when using

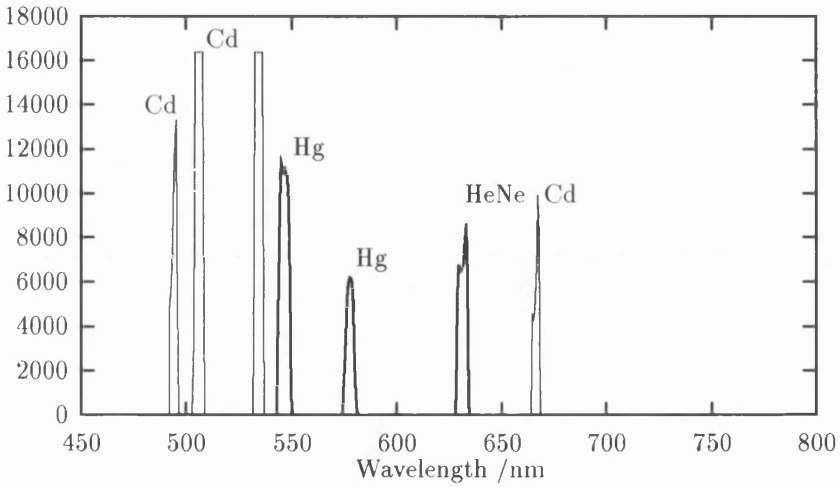

Figure 4.8: Spectral lines used in wavelength calibration procedure.

laser sources) neutral density filters may be required to reduce the intensity of light entering the spectrograph and hence make the CCD detector exposure times for the sources comparable.

The first visual check made when examining a calibration data set is the horizontal position of the peaks as a function of vertical position on the CCD detector. If the detector is aligned correctly, the intensity peaks appear at the same horizontal pixel position across the whole CCD array, since the wavelength spread is parallel to the horizontal axis of the array. Any tilt between the spectrograph and the CCD detector would be manifested as a change in horizontal peak position as a function of vertical track. The actual angle of tilt can be then measured using standard trigonometric analysis. Before proceeding any further it is essential that any tilt be corrected, and a new calibration data set recorded since the wavelength calibration for a tilted set would depend on the particular vertical

position considered. At this point the importance of having a large vertical image is evident; the more vertical CCD tracks the image covers the more accurately the CCD can be positioned rotationally.

To perform the calibration, the intensity peaks must be matched with published values for the significant emission lines of the source in question. In general, for laser sources which are monochromatic over the wavelength range covered by this experiment, this is a simple process. Sources with more than one line are more complex as not all the lines in the published spectrum are necessarily detected, again because of the spectral range of the experimental system. Therefore the lines must be matched taking into account their relative peak intensities as well as their spacing, given that there is a linear pixel/wavelength relationship. Once the lines have been matched, there are two alternatives for determining the calibration relationship from the different data sets. Both use a linear regression technique, assuming a relation of the form

$$\lambda = \lambda_0 + n\Delta\lambda, \tag{4.3}$$

where λ_0 is the wavelength of the shortest wavelength detected by the CCD, n is the pixel number being considered, and $\Delta\lambda$ is the wavelength dispersion, i.e., wavelength increment between pixels. The first method involves performing a regression analysis on each individual data set to calculate values for λ_0 and $\Delta\lambda$. These can then be used to calculate mean values over all the data sets. This method cannot be performed for laser sources where only one peak position is measured, since the regression process requires at least two points for a calculation. The second method combines all peak measurements from all sources in one single

regression to produce a single pair of values, λ_0 and $\Delta\lambda$.

The second method is used to determine values for both λ_0 and $\Delta\lambda$. The value of $\Delta\lambda$ can then be compared with the values calculated previously from the physical dimensions of the spectrograph/CCD arrangement. Any discrepancy in these two values may be due to incorrect spectral lines being attributed to the peaks in the data sets. This may be investigated using the first regression technique by examining individual $\Delta\lambda$ estimates to pinpoint wrongly analysed data sets. Using these regression results reduces the amount of peak matching required during the calibration procedure.

4.4.2 Spectral Response Coefficients

The optical systems used are constructed from individual optical components, lenses, filters etc. The light emitted from the hot sample passes through each of these components until it forms a focused image on the surface of the CCD detector. However each component has its own spectral response, i.e., it responds differently to light depending on its wavelength. For any spectral analysis to be performed it is imperative that absolute values for the irradiance of the light from the sample are known. Therefore the purpose of the spectral sensitivity calibration is to correct for the varying optical responses of the individual elements in the optical systems, and to produce a set of absolute irradiances, which can be spectrally analysed to give a radial temperature profile.

It is assumed that the response of the system is dependent only on the wavelength of the light passing through it, and is independent of the optical path. This only breaks down for strongly focusing systems, since the reflection and transmission coefficients for transparent optics are dependent on incident angle. Preliminary experiments showed this assumption to be good for this particular experimental set up, the spectral correction coefficients being uniform across the entire data set measured. Under this assumption a single correction factor is required for each wavelength measured, rather than one for every individual pixel on the CCD image, making the process of spectral correction much simpler.

The overall set of spectral response coefficients is specific to the optical system used in the experiment. Therefore it is necessary to perform a calibration for every system used in the experimental analysis of a heated sample. There are three focusing systems: circular (section 3.2.2), microscope objective (section 3.2.3) and cylindrical (section 3.2.4) which all use different optical components, so three calibration procedures must be performed. Before the spectral calibration set can be determined it is necessary to have already performed an accurate wavelength calibration because the experimental data set for the white light source must be compared directly with the source's spectral irradiance data and colour temperature. The comparison can only be made if the wavelength to which each CCD pixel corresponds is known.

The same experimental set up as for the wavelength calibration is used with the spectral line-emitters being replaced by a single, known colour temperature source. The source is specifically not placed at the focal point of the lens L_1 (in figure 3.2) as this ensures that a non-focused patch of light, rather than a complete image,

is incident on the spectrograph entrance slit. Not having a focused image means that there is no requirement to do any spatial analysis on the resultant CCD image.

For this particular calibration a 12V, 100W tungsten halogen projector lamp with a sandblasted quartz envelope was used as the source. The lamp was calibrated at NPL [36] to a colour temperature of 2977K, with a complete set of relative irradiance values for wavelengths between 300nm and 800nm, spaced every 5nm. These irradiance values were normalised to give a relative value of 100 at a wavelength of 550nm. The quartz envelope provides a diffusely emitting surface for the optics to image. As in the case of the wavelength calibration, the image formed by the focusing optics was arranged to be as large as possible and need not be contained within the dimensions of the slit. This is a simple process for a large source such as a tungsten lamp, since the focusing system produces a magnified image of the source. It is acceptable for the image to be large since no spatial analysis of the image is performed. The large image also ensures that the maximum number of vertical CCD tracks are covered by the image, allowing more accurate calculations of the spectral calibration coefficients to be performed.

Once a full CCD image has been recorded, the data along each slice is normalised to a selected wavelength position, denoted λ_n, and the wavelength at all the data points calculated from the wavelength calibration performed previously. The wavelength of the HeNe laser line (i.e., 632.8nm) has been chosen as the normalisation wavelength λ_n since this is easily located during the wavelength calibration, and is in the centre of the data set obtained. This assumes the CCD is positioned to detect the longest wavelengths of the spectrograph image, this being the opti-

mum position for imaging the spectral irradiance peak for lower temperatures.

The resulting data is a complete set of normalised intensity–wavelength points, one set for each slice on the CCD detector for which data was recorded. The irradiance values for the calibrated source must now be re-normalised to the same wavelength as the experimental data to ensure that both sets of data are on the same absolute scale. Since the calibration set is not measured at the same wavelengths as the experimental data set, it is necessary to interpolate irradiance values for the calibration set. A typical interpolation method uses a cubic spline fitted through the entire re-normalised calibration set, and the resulting cubic curves are then used to calculate values at the exact wavelengths measured in the experimental data set. The Planck curve corresponding to a colour temperature of 2977K is not suitable for the interpolation since it deviates from the experimentally measured irradiances at long wavelengths.

At this stage there are now two complete irradiance sets: one the normalised experimental data, the other the re-normalised, interpolated calibration set. A comparison can now be performed between a set of experimental data and the calibration set to produce multiplication factors which convert the experimental data into the calibrated data set:

$$m(\lambda) = \frac{C(\lambda)}{I(\lambda)}, \tag{4.4}$$

where C is the calibration set value, I is the experimental data, and m is the calculated multiplication factor. These factors are the sensitivity coefficients that may be used to correct for the spectral sensitivity of the optical systems components.

The re-normalisation of the source irradiance values ensures that the multiplying factor calculated at the selected normalisation wavelength λ_n is always 1, since $C(\lambda_n)$ equals $I(\lambda_n)$.

A set of correction factors is calculated for each vertical position on the CCD detector image. At wavelength positions which give an irradiance value of zero, no multiplication factor can be found to convert this into the calibrated data set value, so a default multiplication factor of zero is assigned to discard information from that pixel.

The multiplication factors calculated at each wavelength are now considered in turn, and used to determine a mean value of spectral sensitivity for that wavelength. Any value of zero is ignored in this calculation, since the irradiance value at that point must also have been zero. If there are any wavelengths for which all the calculated correction factors are zero, the overall factor also defaults to zero.

There may be instances towards the edge of the detected image where the normalised measured irradiances are very small. At these points the multiplication factors may become very large and susceptible to noise ($m \propto 1/I$). If the multiplication factor has a large associated error, then when the sensitivity correction is performed for a true experimental data set, the irradiances at the edges of the data set will be unreliable. The percentage error in m can be calculated from

$$\frac{\sigma_m}{m} = \frac{\sigma_I}{I}, \tag{4.5}$$

and the corresponding error in the sensitivity corrected experimental set calculated from

$$\frac{{\sigma_{I_c}}^2}{I_c} = \frac{{\sigma_m}^2}{m} + \frac{{\sigma_{I_r}}^2}{I_r}, \tag{4.6}$$

where I_r is the raw experimental data, and I_c is the sensitivity corrected data. These points are included in the calculation of multiplication factors and the problem is addressed in the sensitivity correction stage of the mathematical analysis A typical set of correction factors are shown on figure 4.9, the ripple introduced by the dichroic mirror being clearly evident.

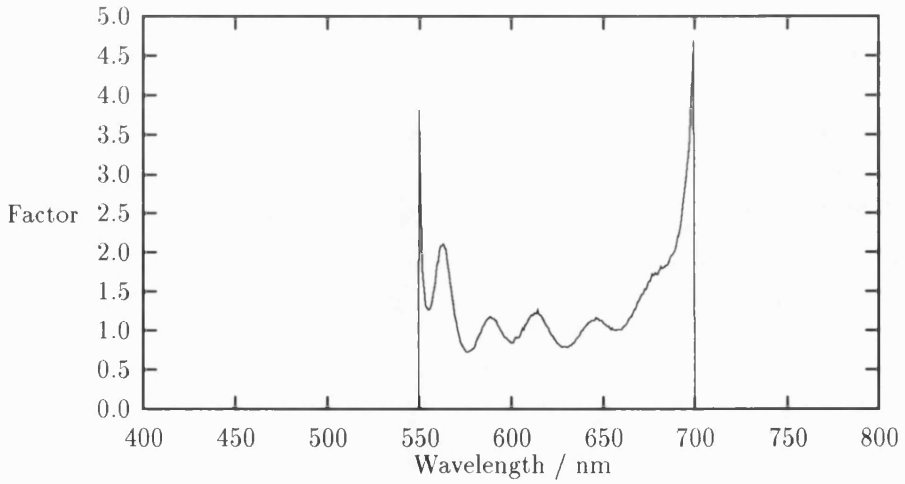

Figure 4.9: Typical set of spectral correction factors

Chapter 5

Mathematical Analysis Procedure

There are several mathematical processes required to convert from a set of two dimensional CCD data into a radial temperature profile. The first procedures act on the full CCD image as a whole, and include the correction for the spectral sensitivity of the experimental system, followed by a two-dimensional smoothing process to remove any spots or local artefacts from the image. Each vertical track (constant wavelength) is then considered in turn and the centre of the data set located. The data is symmetrised, smoothed and Abel inverted to convert to a radial position–wavelength distribution. Finally, the temperature is fitted to the wavelength dependent data at each radial position in turn, producing a set of temperature–radial position values. Each of these stages is now discussed in more detail.

5.1 Spectral Sensitivity Correction

The optical components of the system do not have a uniform response to all wavelengths of light. Before any analysis can be performed the absolute light intensity values emitted by the hot sample must be calculated.

The spectral response coefficients discussed in section 4.4.2 consist of one multiplicative correction factor for each measured wavelength. For a selected data point at horizontal (wavelength) position i and vertical position j, this correction can be expressed mathematically as:

$$I_c(\lambda_i, y_j) = m_i \times I_u(\lambda_i, y_j)\,, \tag{5.1}$$

where I_c and I_u are the corrected and uncorrected intensities respectively, and the m_i are the correction factors at the wavelengths λ_i.

To prevent excessive noise being added to the data by the correction method, there are certain numerical restrictions imposed on the correction coefficients.

An obvious restriction is that the correction coefficient cannot be negative, as this would imply that negative intensities are being measured by the detection system. This is checked for at the calibration stage, rather than at the final correction stage, as it implies errors in the calibration process (see section 4.4.2).

A more important restriction, in terms of the analysis of a data set, is a limit on

the magnitude of the positive correction factors. Because of the system response, there is only a small region of the wavelength spectrum in which data can be obtained. At the edges of this region the response is much smaller than at the centre, and hence the correction factors are much greater. This is demonstrated by the typical spectral correction set shown in figure 4.9. If a new data set is wider than the range of the calibration, then the large correction factors at the edges may cause spikes to appear in the corrected data set. Such spikes would cause incorrect temperatures to be calculated as the intensity values at the edge will not correspond to the true intensities. This effect may be observed when a temperature profile is measured which is much cooler (or hotter) than the calibration set, since the peak irradiance in the Planck distributed light would then be moved to longer (or shorter) wavelengths. The magnitude check is performed at the mathematical correction stage, rather than during the initial calibration process, as this allows different limits to be applied, depending on the shape of data recorded.

5.2 Removal of Localised Irregularities

After initial experiments were performed, it became apparent that two forms of localised irregularity can occur in a data set. These took the form of either a dark spot, or a dark ring with a bright centre. Figure 5.1 demonstrates a data set which has a large number of such spots, and figures 5.2(a) and 5.2(b) illustrate enlarged images of typical dark and light spots respectively.

An initial explanation for these spots could be that some of the pixels of the CCD detector are not performing as they should, i.e., there is a pixel "drop-out". In the

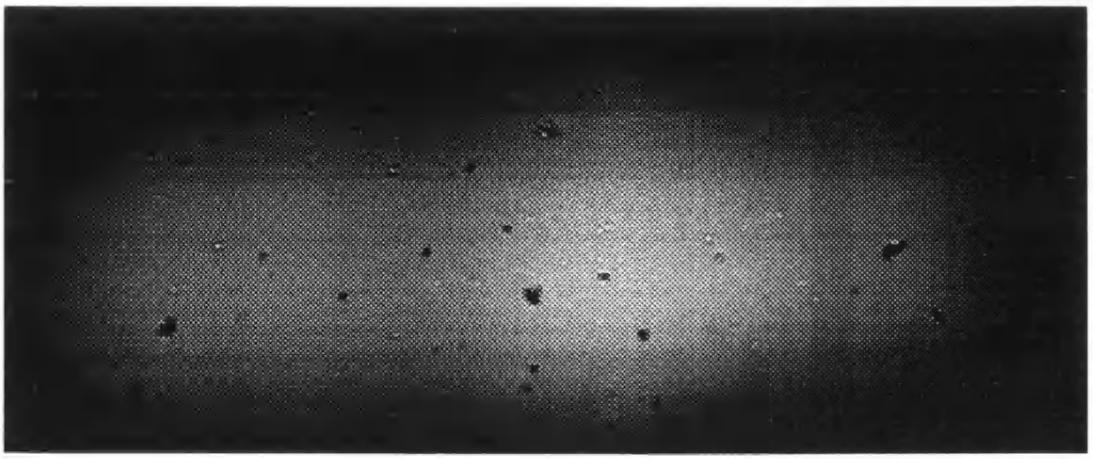

Figure 5.1: Full image of data set with dark and light spots

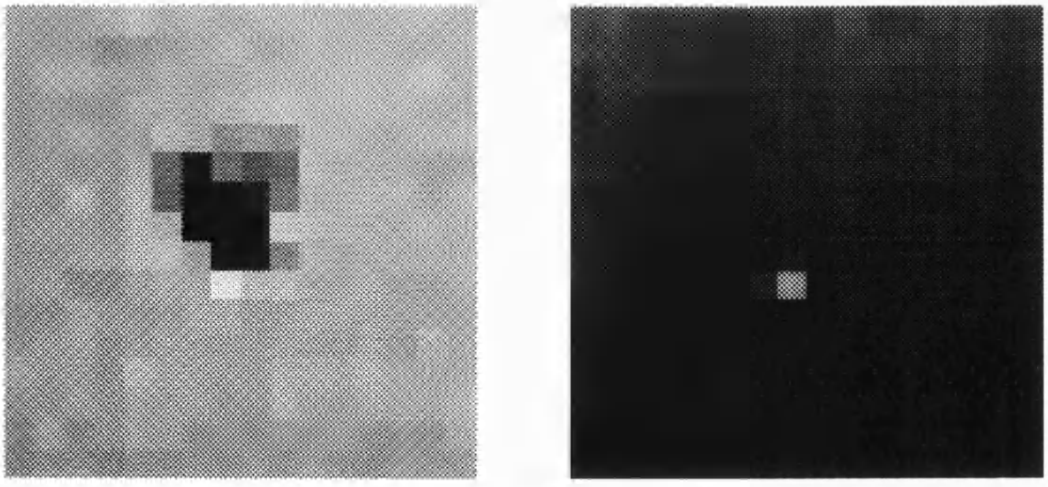

(a) Enlarged image of dark spot

(b) Enlarged image of light spot

Figure 5.2: Examples of localised dark and light spots in an image

example shown in figure 5.2(a) it can be seen that the dark spot would require at least 9 pixels to be completely non-functioning. This example (figure 5.1) contains many dark spots, and would require much of the CCD detector to consist of "dead" pixels. The drop-out hypothesis does not explain the existence of the light centres to some of the spots (figure 5.2(b)). The centre of these spots is much lighter than the surrounding image, and implies that the pixels were responding more efficiently than should be expected. The position (and existence) of the spots is also not consistent between data sets acquired on different days. These three observations suggest that the irregularities cannot be a consequence of dead pixels, as the dark spots would then necessarily be static, usually one pixel across, and light spots would not occur.

A more reasonable alternative hypothesis is the formation of ice-crystals and water droplets on the surface of the CCD detector. These are a direct result of the interior of the CCD casing not being completely dry before the Peltier cooler is switched on (see section 3.2.6). The ice-crystals prevent light falling on a small collection of pixels, by scattering the light incident on them and hence produce a small dark area on the CCD. It was observed that the light centred spots only occurred when the Peltier cooler was set between -5°C and 10°C, which suggests that these were caused by condensation of water droplets, rather than ice-crystals. The droplet acts as a thin lens and focuses the incident light to a smaller spot, causing the bright centre, whilst decreasing the intensity of light falling in the area around the centre. The mechanisms for the effects of the ice crystals and water droplets are demonstrated in figures 5.3(a) and 5.3(b) respectively.

The simplest method to avoid these irregularities is to ensure that the CCD cavity

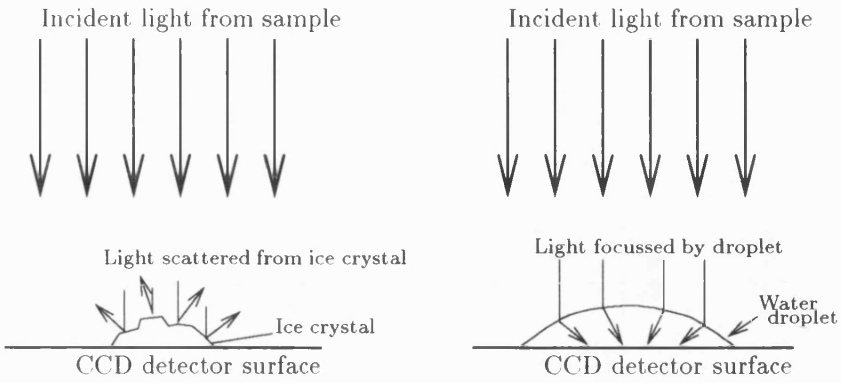

(a) Ice crystal (b) Water droplet

Figure 5.3: Effect of ice and water on the CCD detector surface.

is completely dry before any measurements are made with the detector at a reduced temperature. However in practice a completely dry detector casing cannot be guaranteed, and a procedure must be available to remove any spurious spots which do occur in a data set.

5.2.1 Filtered Fast Fourier Transform

The general method for the removal of "artefacts" in an n-dimensional data set is the application of a filtered n-dimensional Fast Fourier Transform (FFT). The noise seen on the data sets is small, compared to the overall dimension of the data set. When the Fourier Transform is taken, this noise appears in the higher spatial frequency components, whilst the data itself is contained in the low order components. The usual method for performing smoothing on such a transformed data set is to pass it through a lag-window, designed to reduce the amplitude of the high order components, leaving the lower order either unchanged, or modified

by only a small amount. This process can be represented mathematically by modifying the inverse Discrete Fourier Transform equation

$$f(x) = \sum_{k=-\infty}^{\infty} F(k\omega)e^{ik\omega t}, \tag{5.2}$$

to include a multiplication factor λ_k associated with each frequency $k\omega$

$$f(x) = \sum_{k=-\infty}^{\infty} \lambda_k F(k\omega)e^{ik\omega t}. \tag{5.3}$$

There are a number of lag windows that may be used. For the data measured in this experiment, three windows were considered: the Heaviside (or step function) window, the Tukey–Hanning window, and the Parzen window, which are now discussed in turn.

5.2.1.1 Heaviside Window

The simplest form of lag window is the Heaviside window. The functional form of the Heaviside (in 1-dimension only) is

$$\lambda_k = \begin{cases} 1 & k \in [0, M] \\ \\ 0 & k \in (M, N] \end{cases} \tag{5.4}$$

where M is the truncation point of the Heaviside (i.e., its width), and N is the width of the data set. M is less than N. The window's effect is to remove all

the spatial components above a frequency corresponding to the width M, while leaving the lower frequencies untouched. This lag window is not very suitable for smoothing, as the sharp spatial frequency cut-off introduces a substantial amount of ripple into the spatial coordinates.

5.2.1.2 Tukey-Hanning and Parzen Windows

Two windows commonly used in time-series analysis are the Tukey-Hanning, and the Parzen windows [37]. The Tukey window is represented by the function

$$\lambda_k = \frac{1}{2}\left(1 + \cos\frac{\pi k}{M}\right) \qquad k \in [0, M] \tag{5.5}$$

whereas the Parzen window is defined by two piecewise functions

$$\lambda_k = \begin{cases} 1 - 6\left(\frac{k}{M}\right)^2 + 6\left(\frac{k}{M}\right)^3 & k \in [0, M/2] \\ 2\left(1 - \frac{k}{M}\right)^3 & k \in [M/2, M] \end{cases} \tag{5.6}$$

In both cases M is the truncation point of the lag window, above which no frequency components are included. These two curves have similar shapes over their central region; however the Parzen window has a slightly smoother tail which reduces the possibility of introducing ripples to the smoothed data set, as in the Heaviside case.

5.2.1.3 Comparison of lag windows

The one dimensional forms of these windows are shown in figure 5.4. To allow a direct comparison of the window forms, the characteristic lengths (or truncation points) of the three curves are matched according to the equation set

$$M_H = \frac{3}{8}(M_T - 4) \tag{5.7a}$$

$$M_P = 1.39 M_T \tag{5.7b}$$

where M_H, M_T and M_P are the one dimensional truncation points for the Heaviside, Tukey–Hanning and Parzen windows respectively. The derivation of these equations can be found in Ref. [37]. In the case of figure 5.4 the truncation point for the Tukey window (M_T) has been arbitrarily chosen as 100, with the other points being calculated as $M_P = 139$, and $M_H = 36$.

The effect of each window is demonstrated by considering a small area of an experimental data set containing a number of both dark and light spots, as shown in figure 5.5. The full set is 576 pixels wide and 384 pixels high, with the extracted area being 50 pixels square. For a comparison of the windows to be performed, it is necessary to match their truncation points in both axes simultaneously. Since the data in this experiment is two dimensional, the windows chosen for smoothing are elliptical with the major and minor axes specified by two characteristic truncation points, denoted M_x and M_y. Again, both lengths must be variance matched individually.

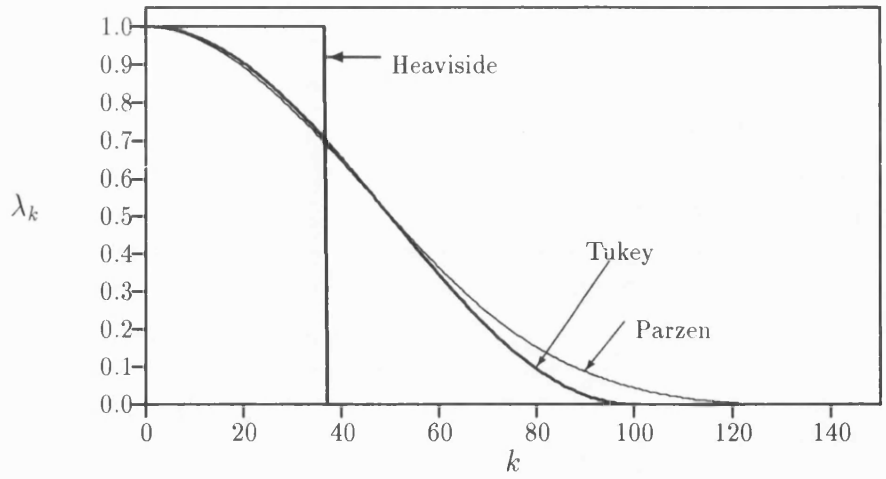

Figure 5.4: Forms of lag window used for filtered Fourier Transform smoothing.

To demonstrate the smoothing process, two window sizes have been chosen arbitrarily (for the Tukey window) as 2/3 and 1/3 the size of the data set (in both dimensions). These two window sizes allow comparison between a wide and narrow window respectively. The sizes of the corresponding Heaviside and Parzen windows have been calculated from equation set 5.7 and are listed in table 5.1.

Window type	Large		Small	
	M_x	M_y	M_x	M_y
Heaviside	70	30	35	15
Tukey	192	85	96	43
Parzen	267	118	133	60

Table 5.1: Lag window sizes used for smoothing comparisons

The smoothing produced by these six windows (three types of two sizes) are shown in figures 5.6 to 5.8. The ripple introduced by the Heaviside window is observed as rings around the spots in the data set (shown in figure 5.6(a)). The

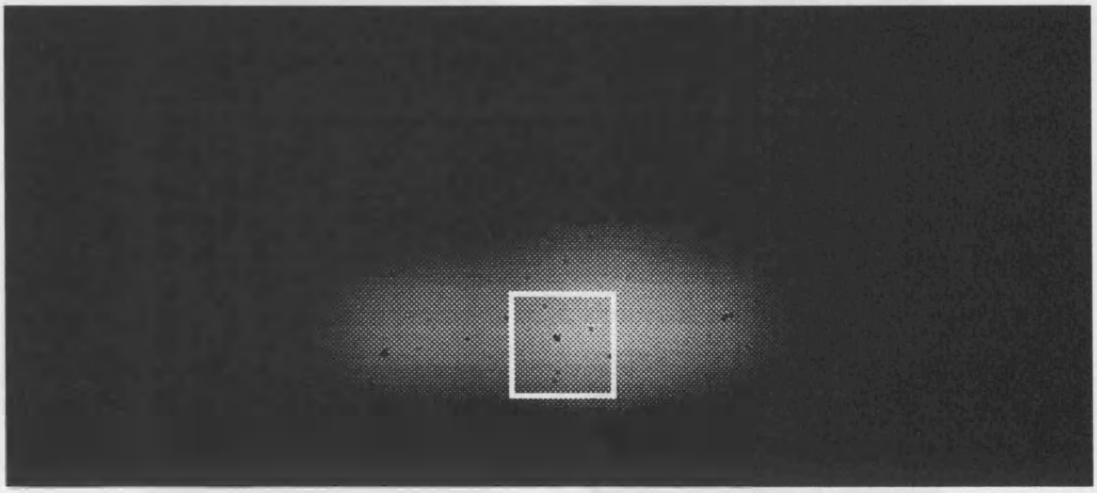

(a) Full set

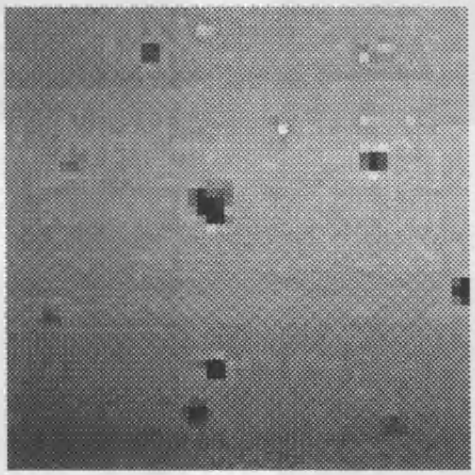

(b) Extracted area in square

Figure 5.5: Full data set with a number of spots

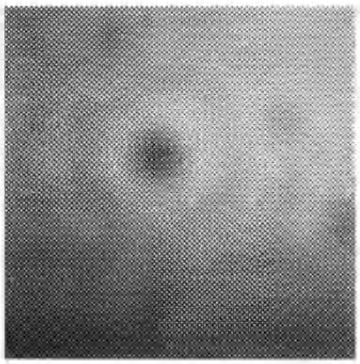

(a) $M_x = 70$, $M_y = 30$

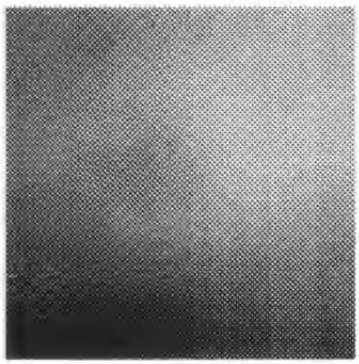

(b) $M_x = 35$, $M_y = 15$

Figure 5.6: Smoothing with the Heaviside Window

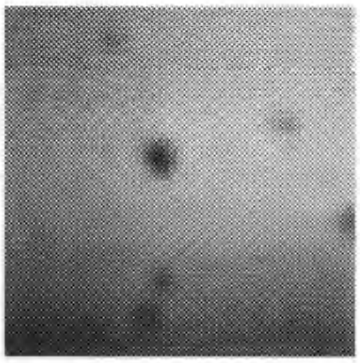

(a) $M_x = 192$, $M_y = 85$

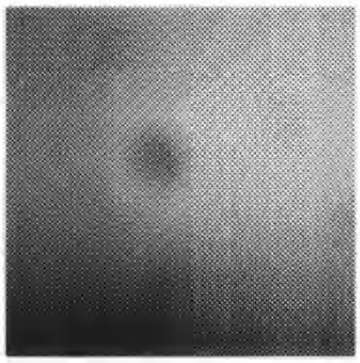

(b) $M_x = 96$, $M_y = 43$

Figure 5.7: Smoothing with the Tukey Window

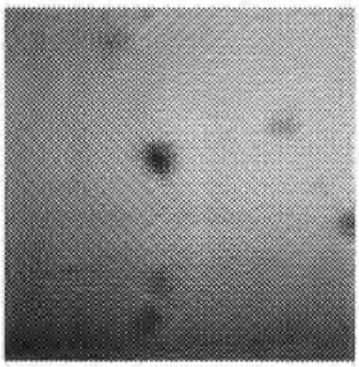

(a) $M_x = 267$, $M_y = 118$

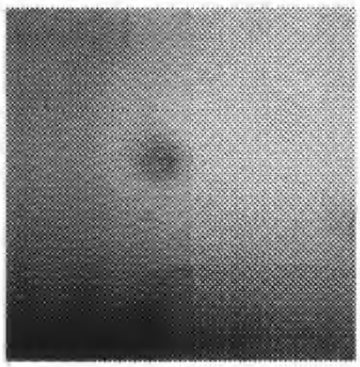

(b) $M_x = 133$, $M_y = 60$

Figure 5.8: Smoothing with the Parzen Window

Tukey and Parzen windows show almost identical effects due to the similarity of their shapes; however the main form of the image is less affected by the Parzen window due to the inclusion of the extra spatial frequencies. In all three windows the smoothing virtually eliminates the spots for the smaller window size; however close examination of the Heaviside smoothed windows shows that the overall shape of the data is slightly altered by the low spatial frequency cut-off. In terms of suitable smoothing windows, the Tukey and Parzen windows eliminate spots, without excessively modifying the data. The choice of truncation point in either dimension is quite arbitrary and would generally depend on the relative sizes of the recorded image and the CCD array: a small image on the CCD requires a larger window to allow full reconstruction of the overall shape of the curve.

5.3 Finding the Centre of the Data Set

The later stages of analysis require that the data be axially symmetric about the centre of the heated spot. Therefore it is essential to locate the spatial centre of the data set before any further analysis can be performed. One assumption of the experiment, given that laser induced heating is employed, is that the peak temperature coincides with the centre of the data, and thus has the largest spectral intensities. Therefore the algorithm must find the centre of the set, given that the peak intensity value should also be at the centre. To enable the conversion from line profiles to radial data using the numeric form of the Abel inversion (section 5.6), the centre is assumed to lie between two data points. The left point of this pair is assumed to be the track centre for the purpose of calculating the average position of the centre over all wavelengths.

As discussed in section 3.2.5 it may be assumed that the data is spectrally split parallel to the axis of the CCD detector, and hence each of the wavelength positions should have an identical centre position. This needs to be checked for during the alignment and calibration procedure (chapter 4). Because of the random noise associated with any experimental process, when a calculation of the centre position is performed, it may not produce identical values for each wavelength. For this reason, the following method is chosen. The centre position is measured for each wavelength position where light is detected. These positions are then assumed to come from a normally distributed set $\mathcal{N}(\mu, \sigma^2)$, where μ is the mean centre position and σ^2 is the variance associated with the set, permitting a simple calculation of mean centre position, together with error bounds. It is this mean value which is then used as the centre for all the wavelength positions considered in later analysis.

Three typical methods for finding the centre position of a data set are: peak data value, equal integral, parabolic curve fitting, which are now discussed in turn, together with their associated advantages and disadvantages.

5.3.1 Peak data value

The simplest assumption is that the peak value of the data set is at the track centre. However this method is very unstable, as there may be large artefacts in the data set (as described in section 5.2) which cause the measured centres to vary greatly, depending on the relative positions of any such artefact to the true centre. It is also susceptible to random experimental noise around the peak value.

These two factors may cause the measured centres at each wavelength position to vary greatly over the entire data set.

5.3.2 Equal Integral

Axial symmetry implies that the total irradiances to either side of the spot centre are identical. Therefore this method finds the point for which the integrals to each side are equal:

$$\int_0^c I(x)\,dx \;=\; \int_c^N I(x)\,dx \tag{5.8}$$

where c is the centre point to be located, and N is the size of the data set.

Obviously, as the data consists of discrete points, the actual implementation uses a summation method, rather than integrals. It is also unlikely that a single point on the curve will have exactly equal integrals to each side; hence the point to the left of the 'equal integral' position is referenced. This point is determined by the maximum value of c for which the summation

$$\sum_{n=0}^{c} I_n(x) \;<\; \sum_{n=c+1}^{N} I_n(x) \tag{5.9}$$

holds. This is most easily achieved by starting with c as the middle data position in the set (i.e. $N/2$), and using a bisection type algorithm to find the centre. A linear search through the data set may result in a much larger number of

calculations being performed, depending on both the size of the data set and the relative position of the centre within this set.

One disadvantage of this method is that it does not find the peak value if the data is very skew, but will select a point someway down the wider side. However it is quite immune to random noise, as the process of integrating will improve the signal/noise ratio. This is in contrast to the peak finding method, which is very susceptible to noise, but does locate the peak of the recorded data (even though this peak may be due to noise in the data set).

5.3.3 Parabolic Curve Fitting

This method is designed to find the peak value (and hence the theoretically assumed centre of the data set) taking the overall shape of the curve into consideration. Laser heating with a TEM_{00} beam induces a single hot spot on the surface with a monotonically decreasing temperature distribution around the centre. By fitting a parabolic curve to the section of the curve around the centre, the data is forced to have a single maximum point, and thus be monotonically decreasing. However it is essential that only the non-zero data values are considered, and so the range of suitable values must be determined before a fit can be performed.

This method requires an initial estimate of the centre position so that a suitably small section of curve may be selected. This estimate may be made using either one of the previous methods (finding the peak, or equal integral position). The equation of the parabola fitted through the points surrounding the estimated cen-

tre is calculated using a non-linear regression technique. The resulting quadratic coefficients are then used to locate the position with zero gradient, and hence the maximum point. The position of the maximum, in general, occurs between two data points. To comply with the implementation of the Abel inversion stage, the point to the left of this centre position is then used as the reference point.

5.4 Smoothing Along Tracks – optional

The previous smoothing stage (section 5.2) is designed to remove any of the localised irregularities that may be present, whilst leaving the overall shape of the curve intact. This optional smoothing stage is then designed to smooth further the data in the direction in which the Abel Inversion is performed. Obviously, if the data set has few (or no) artefacts, the previous smoothing stage may not necessarily have been performed.

There are numerous smoothing methods, and one of the simplest is the unweighted moving average method. In this the smoothed value at a selected point is the mean of the point itself and a number of its neighbours, which can be expressed as:

$$I_s(x_i) = \frac{1}{2S+1} \sum_{k=i-S}^{i+S} I_u(x_i), \tag{5.10}$$

where I_s is the smoothed function, I_u is the unsmoothed function and S is the one-sided width of the averaging window.

A slightly more advanced method is the weighted version:

$$I_s(x_i) = \frac{\sum_{k=i-S}^{i+S} W(x_k) I_u(x_k)}{\sum_{k=i-S}^{i+S} W(x_k)} \tag{5.11}$$

with $W(x_k)$ being the weight of the k^{th} data value. These weights can either be calculated from the variances associated with each specific data point (generally only useful if each data point is calculated from a separate data set in such a way that a variance may be determined), or be general to any data set, to make the smoothing less susceptible to artefact noise. A typical weighting function that is used is defined as

$$W(x_{i+j}) = 1 - \left|\frac{j}{S+1}\right| \qquad \forall\, j \in [-S, S] \tag{5.12}$$

where S is the width of the averaging window, and j is a local index. For example, it S is chosen as 4 (corresponding to a 9 data point window) the weights used would be 1/5, 2/5, 3/5, 4/5, 1, 4/5, 3/5, 2/5, and 1/5. This means that points further from the position being considered would have less direct effect than nearer points.

The moving average methods are only suitable for data with small amounts of random noise, since the process merely spreads any errors through the surrounding points, and hence cannot remove large errors on any data values. Therefore it is not suitable for data sets with local artefacts (as described in section 5.2) which have not been removed prior to this smoothing stage.

Other alternative smoothing methods may be used, such as Fourier Smoothing (as discussed in section 5.2.1, but applied to only one dimension) or cubic splines [38].

5.5 Symmetrising Along Tracks

The Abel Inversion (section 5.6) requires that the temperature distribution is axially symmetric (see chapter 6). The raw data obtained from the experiment is not entirely symmetric due to random noise present during the measurement, so the data must be symmetrised.

Any function $f(x)$ (whether analytic or discrete data) can be divided into two functions: an even function $e(x)$ (where $e(-x) = e(x)$), an odd function $o(x)$ (where $o(-x) = -o(x)$). This is represented as

$$f(x) = e(x) + o(x). \tag{5.13}$$

The process of symmetrisation is designed to calculate the even function $e(x)$, effectively removing the odd function $o(x)$ from the original. Using the definitions of $e(x)$ and $o(x)$, the alternative equation

$$f(-x) = e(x) - o(x) \tag{5.14}$$

can be written. Adding the two equations provides the method for calculating $e(x)$:

$$e(x) = \frac{1}{2}\left(f(x) + f(-x)\right). \tag{5.15}$$

In terms of the discrete data sets used in this experiment, where each set is a vertical track, this equation can be written:

$$I_{symm}(x_{c+d}) = \frac{1}{2}\left(I(x_{c-d}) + I(x_{c+d})\right) \tag{5.16}$$

where c is the coordinate of the centre of the data set, and d is the displacement from the centre of the point being calculated. This method is known as two-sided averaging.

An alternative method for calculating $e(x)$ can be derived by taking the Fourier Transform of equation 5.13 [39]:

$$F(s) = 2\int_0^\infty e(x)\cos(xs)\,dx - 2i\int_0^\infty o(x)\sin(xs)\,dx \tag{5.17}$$

where s is a spatial frequency. The even part of the function will thus be transformed into the real component of the complex Fourier spectrum, and the odd part into the imaginary component. For experimental data, the real component of its discrete transform may be inverted to produce the even (symmetric) part of the original data:

$$e(x) = \mathscr{F}^{-1}\Big[\Re\Big[\mathscr{F}\left[f(x)\right]\Big]\Big] \tag{5.18}$$

Both methods outlined here give identical results for the symmetrisation process

since they both evaluate the same equation (5.15). The Fourier method may be advantageous in that it can be included into either of the smoothing stages.

5.6 Abel Inversion

The Abel Inversion is the main stage of the analysis procedure. The data is recorded as a series of line profiles across the sample surface (see section 3.2.7), but the final result required is a radial temperature distribution. This stage performs the conversion between the profiles and the radial distribution. The actual transform is too complex to be dealt with in this present chapter, and a full treatment is given in chapter 6, where both the Abel Transform pair, and the more general case of the Radon Transform pair, are discussed. The simplest numerical form of the Abel Inversion: the Nestor and Olsen method, is also derived in chapter 6.

The Abel Inversion (especially the Nestor and Olsen implementation) is susceptible to noise in the data since gradients are required in the calculation. This simple method is suitable for application to the data taken in this experiment (assuming that it is not particularly noisy) since the data is smooth and has no step discontinuities. The previous smoothing stages may be used to reduce the noise present in a data set, allowing a more stable inversion process. The numerical equation used in the Nestor and Olsen method is given by the equations

$$I(\lambda, r_k) = \frac{-1}{\pi} \sum_{n=k}^{N} B_{kn} I_n \quad \forall k \in [0, N] \tag{5.19a}$$

where

$$B_{kn} = \begin{cases} -A_{kk} & \text{for } n = k \\ A_{kn-1} - A_{kn} & \text{for } n > k \end{cases} \tag{5.19b}$$

$$A_{kn} = \frac{((n+1)^2 - k^2)^{1/2} - (n^2 - k^2)^{1/2}}{2n+1} \tag{5.19c}$$

and $I(\lambda, r_k)$ is the calculated intensity at wavelength λ and the k^{th} radial position from the centre (centre is at $k = 0$).

One inversion is performed for each wavelength measured by the CCD (only on the pixels which detect light). This assumes that a track is a profile measurement of the whole sample for a given wavelength λ. Therefore the result of the inversion stage is to convert from a function of y (vertical position on the CCD with zero as the centre of the spot) to a function of r (the radial distance from the centre of the spot):

$$I(\lambda, y) \rightarrow I(\lambda, r). \tag{5.20}$$

5.7 Fitting for Temperature

Once the data has been converted into a function of wavelength in one dimension, and radial distance from the centre of the hot-spot in the other, the temperature can be found. By considering each radial position in turn, the intensity–wavelength data can be compared to the Planck curve:

$$I(\lambda, T) = \frac{2\pi hc^2 \varepsilon \lambda^{-5}}{e^{hc/k\lambda T} - 1} \tag{5.21}$$

to determine the temperature distribution across the sample. There are many ways of performing this comparison; however the usual method is some form of regression or curve fitting. For this particular data, four methods have been selected: three linear regression models and one non-linear curve fit.

5.7.1 Wien Approximation

The Planck black-body equation (5.21) is a non-linear equation. To perform a linear regression, a linearised approximation must be used, a suitable form being derived from the Wien equation (as described in section 2.3):

$$I(\lambda, T) = \frac{2\pi hc^2 \varepsilon \lambda^{-5}}{e^{hc/k\lambda T}}. \tag{5.22}$$

This numeric forms of these two equations are very similar and only begin to differ for very high temperatures and at long wavelengths (above ≈700nm), as demonstrated in figure 5.9. As the experimental range of the apparatus is between 550nm and 750nm (maximum) the use of the Wien approximation for linear analysis is reasonable.

The Wien equation (5.22) is non-linear, but is linearly reducible to the form:

$$\ln\left(\frac{I}{2\pi hc^2 \lambda^{-5}}\right) = -\frac{1}{T} \cdot \frac{hc}{k\lambda} + \ln \varepsilon \tag{5.23}$$

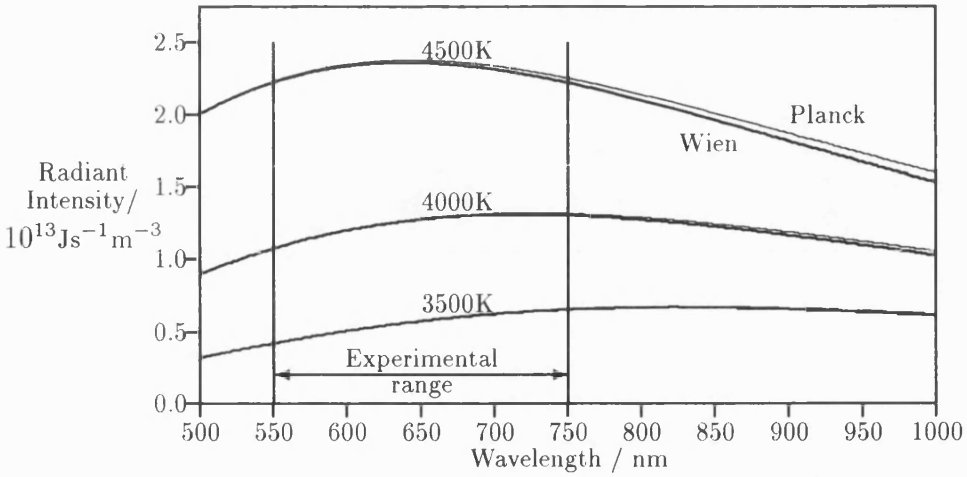

Figure 5.9: Comparison of Wien and Planck curves at Selected Temperatures

which is linear in $1/T$. If the experimental I–λ data are transformed into this linearised Wien approximation, standard linear regression procedures may be used to calculate the corresponding temperature and emissivity.

5.7.2 Unweighted Linear Regression

This is the simplest model for normal regression procedures. It assumes that all the experimental data points have an equal and independent variance, denoted σ^2. By using the linearised Wien approximation (equation 5.23), a straight line can be fitted using the modified co-ordinates

$$y = \ln\left(\frac{I}{2\pi hc^2\lambda^{-5}}\right) \tag{5.24a}$$

$$x = \frac{hc}{k\lambda} \tag{5.24b}$$

in a '$y = mx + c$' system. The temperature of the sample at the radial position in question is then determined as $-1/m$. The emissivity of the sample can also be determined, assuming absolute intensities are known, as e^c.

Due to the linear reduction process modifying the data values used in the regression procedure, the assumption of equal point variances is not suitable for the x–y co-ordinate system. The raw I–λ data (prior to linear reduction) can not be assumed to have equal variance, due to the experimental measurement process and the previous mathematical analysis stages, the Abel Inversion in particular. Therefore the unweighted regression process cannot be used for the x–y reduced system to gain accurate temperature values since the assumption that all points are equally important is invalid.

5.7.3 Weighted Linear Regression

To account for the modification of the point variance because of the linear reduction to the Wien approximation, it is possible to set up a weighting function where individual points can be weighted down (given less importance) depending on their relative position within the data set. Then these weights can be used in a weighted regression procedure to obtain the temperature and emissivity.

Since the various mathematical stages (some of which are optional) have alternative implementations (for example the three different lag windows in the FFT filtering stage (section 5.2)), it would be extremely time consuming to calculate weighting functions to correct for the systematic errors connected with all com-

binations of analysis methods. The data also have associated experimental error from the measurement process, implying that a full set of weighting functions cannot be calculated. However the weighted linear regression algorithm is useful in the calculation of iteratively reweighted least squares (section 5.7.4).

5.7.4 Iteratively Reweighted Regression

The unweighted model is adequate if the data being analysed has a small amount of noise which has equal variance. The data obtained from this experiment do not in general have equal variances, as a result of the many mathematical processes required to get the data into a form which can be fitted.

Iterative reweighting [40–42] is a standard method for performing linear regression analysis when the data set has outliers (points far from the general trend of the data). It has the effect of locating any points which are substantially different from the majority of the data set, downweighting them to reduce their effect on the fit. Iterative reweighting is based on a standard linear regression procedure, with the weights of each point in the fit being determined as a function of the final residuals at that point. This can be represented by considering the minimisation of the residual sum of squares:

$$\mathrm{RSSQ} = \sum_{i=1}^{n} w_i \left(Y_i - (\mathbf{X}\hat{\mathbf{\Theta}})_i\right)^2, \tag{5.25}$$

where $\hat{\mathbf{\Theta}}$ is the estimated parameter vector for the regression, and w_i is the weight of the i^{th} point in the data set. The individual weights are calculated as a function

of the final residuals:

$$w_i = w(Y_i - (\mathbf{X}\hat{\mathbf{\Theta}})_i), \tag{5.26}$$

with $\hat{\mathbf{\Theta}}$ being the final estimate of the fit parameters. The procedure for performing the regression is now discussed briefly.

First a normal, unweighted linear regression is performed, and the corresponding residuals calculated for each data point. An estimate $\hat{\sigma}$ of the standard deviation σ, assuming that all the points have equal variance, is then found using

$$\hat{\sigma} = \frac{1}{0.6745} \cdot \text{median } \{|r_i|\} \tag{5.27}$$

where r_i is the residual of the i^{th} point. A set of normalised residuals are then generated:

$$u_i = \frac{r_i}{\hat{\sigma}}. \tag{5.28}$$

These are used in the calculation of the weighting function:

$$b(u) = \begin{cases} \left(1 - (u/c)^2\right)^2 & |u| \leq c \\ 0 & |u| > c \end{cases} \tag{5.29}$$

where c is an arbitrary constant, whose value depends on the overall magnitudes of the data under analysis, and the size of residual that would be considered too

excessive to consider in further regressions. A large value of c causes points with large normalised residuals to be included in the subsequent regression procedures, with higher weighting factors than with a small value of c. The use of normalised residuals u_i enables similar data sets with widely different absolute magnitudes, but variances of the same order, to be analysed using identical values of c, with no effect on the fit results. This is especially important for this particular application as the light from the centre of the hot-spot must be of higher intensity than light from the edge of the sample, simply because of the difference in temperature.

Once the weights of all the data points have been evaluated, a new regression is performed; however this time it is a weighted linear regression, with the weights determined from equation 5.29, rather than an unweighted regression as used in the preliminary fit. A new set of residuals are computed from this revised fit, and the whole process is iterated. The iteration procedure is complete when the individual weights of the data points converge, that is they do not change between successive regression processes. Once the weights have converged, the values of the regression parameters for the line will also have converged to the best fit. It is important to note that all of the individual weights must be tested for convergence, as it is theoretically possible for the parameter values (and hence the line) to converge to a local minimum while the actual weights are still changing. Testing all the weights ensures that the global minimum in the weighted sum of squared residuals has been located, and the line is indeed the best-fit line.

Clearly this method will downweight all points that are substantially different to the majority of the data set. Therefore it is ideal for data which has a large amount of noise in a localised area, for example where an ice crystal has caused

a dark spot (as discussed in section 5.2), and has not been smoothed using the filtered Fourier Transform method (section 5.2).

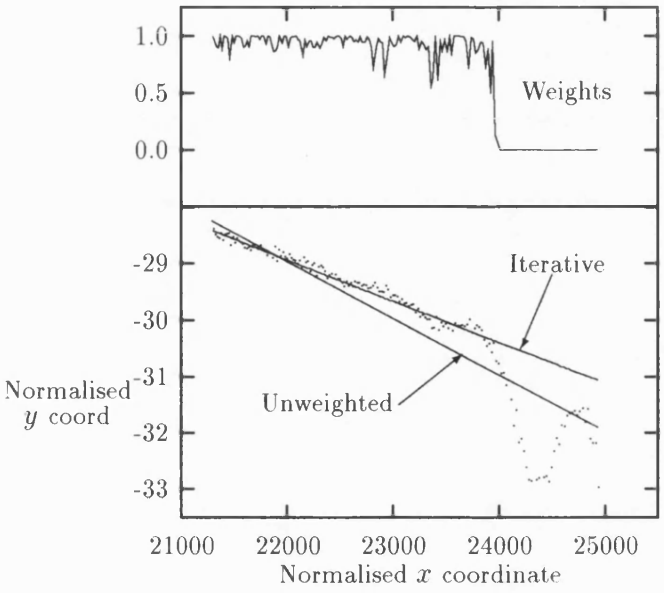

Figure 5.10: Typical fit using the Iterative Reweighting Technique, together with the calculated weights for each point.

The results of using this technique are illustrated by the fit to the data shown in figure 5.10. At the edges of the sample the temperatures are much smaller than at the centre. As a result the image intensities are much smaller, particularly in the short wavelength region as the Planck curve peak is moved further into the red. After the correction the small intensities may still be evident as ripples, and cause the fitted line to be too steep (as shown in figure 5.10). Iterative reweighting allows these points to be located and weighted out to fit the true line.

5.7.5 Non-linear curve fitting

The three linear regressions described rely on using an approximation to the Planck equation (5.21). To fit to this equation directly, non-linear methods are required [43]. Non-linear fitting methods are also (in general) iterative, requiring numerical analysis to find a fit to a curve. The aim of non-linear fitting is identical to the linear regressions: to minimise the sum of squared residuals between the experimental data and the theoretical function, given estimates of the various parameters.

There are many different algorithms for calculating a non-linear fit, Gauss-Newton being one of the simplest [44–46]. The particular algorithm chosen for this experiment is a modified Gauss-Newton approach, implemented as part of the NAG mathematical library [45]. The theory behind general non-linear regression and the model used here is beyond the scope of this text.

5.7.6 Comparison of Fitting Techniques

The four fitting techniques mentioned above (sections 5.7.2 to 5.7.5) all have uses in specific situations. The prime consideration in choosing a particular method is the accuracy and resolution of the result. The simplest example of this can be illustrated by considering the linear regression method (section 5.7.2) defined by equations 5.24(a) and 5.24(b). The temperature resolution of the model can be determined by using the equation set:

$$m = -\frac{1}{T} \tag{5.30a}$$

$$\Delta m = \frac{1}{T^2}\Delta T = m^2 \Delta T \tag{5.30b}$$

$$\Delta T = \frac{1}{m^2}\Delta m = T^2 \Delta m \tag{5.30c}$$

$$\frac{\Delta m}{m} = \frac{\Delta T}{T} \tag{5.30d}$$

where T is the temperature being measured, and m is the calculated gradient.

The regression process gives a value for the gradient, and an estimate of the error in the gradient, making it possible to give error estimates for the temperature. From equation 5.30c it is clear that the error ΔT in temperature varies as T^2, so for a given gradient error Δm, the associated error found in the temperature is much greater for high temperatures. Experiment has shown that the gradient error that can be expected from a good data set is of the order of $5 \times 10^{-5} K^{-1}$. This corresponds to an error in the temperature of 50K and 1250K for points with true temperatures of 1000K and 5000K respectively.

When the temperature on the sample exceeds approximately 3000K, the peak in the Planck curve moves into the spectral range of the experimental system. At this point the non-linear regression process may be used, rather than a linear approximation, since the shape of the curve makes it ideal for fitting the trends in the Planck equation. This model can be used for increased temperature until the peak of the Planck curve moves out of the spectral range (<550nm) where the λ^{-5} term dominates and no temperature information can be derived.

Chapter 6

The Radon and Abel Transforms

6.1 Introduction to the Transforms

The Abel Transform is a standard technique for the calculation of radial distributions. It is the degenerate case of the Radon Transform [47] under the assumption that there is radial symmetry, i.e., there is no angular dependence. The Radon transform and its inverse are used in many applications, from X-ray tomography in medicine, to aperture synthesis in astrophysics. The Abel transform (and its inverse) are more limited because of the symmetry requirement, but their use is prevalent in plasma physics for the measurement of emission coefficients.

The Radon transform was developed by Johann Radon in 1917 [47]. It is a general mathematical transform which can be applied in any number of spatial dimensions, but is generally used in either two or three. The Radon transform converts a distribution into a set of line or surface integrals. Conversely, the inverse transform

converts back from the integrals to the distribution itself. The inverse transform is more practical than the forward transform as it is more common for a measurement process to calculate the integrals, rather than the full distribution. For example, measuring the emission coefficient in a plasma column directly is physically impossible. To measure such properties, remote sensing must be employed, with the detector recording integrals through the distribution. The inverse transform is then applied to reconstruct the distribution of radiance throughout the column [48].

6.1.1 The Radon Transform

6.1.1.1 Mathematical Representation of the Radon Transform

Two dimensions: Consider a two-dimensional point distribution $f(x,y)$ defined in real space $\mathbf{R}^2$. If an arbitrary line ℓ exists in the distribution, the integral along all possible lines is called the Radon transform of f, given by:

$$\check{f} = \mathscr{R}f = \int_{\ell} f(x,y)ds, \tag{6.1}$$

where ds is a small section of the line ℓ.

To derive the functional form of the Radon transform, it is necessary to set up both Cartesian (x,y) and polar (p,ϕ) coordinate systems as illustrated in figure 6.1.

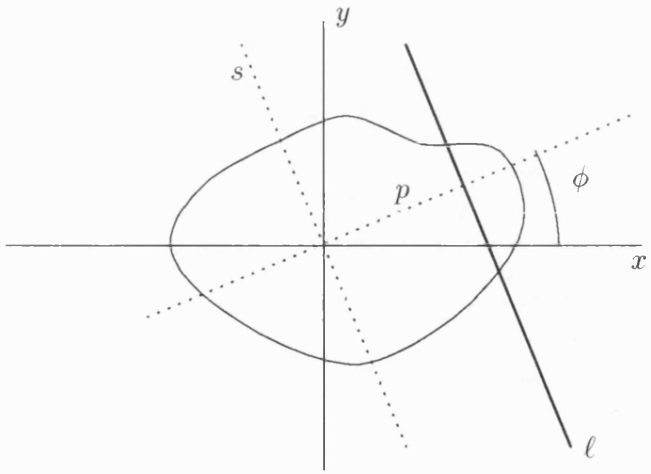

Figure 6.1: Coordinate set used in Radon Transform analysis

The line ℓ is defined in polar coordinates as

$$p = x\cos\phi + y\sin\phi. \tag{6.2}$$

The integral along this line given by equation 6.1 is now modified to

$$\check{f}(p,\phi) = \int_{\ell} f(x,y)ds. \tag{6.3}$$

By rotating the Cartesian coordinates axes such that s is parallel to ℓ and p is perpendicular to ℓ to give

$$x = p\cos\phi - s\sin\phi \tag{6.4a}$$

$$y = p\sin\phi + s\cos\phi, \tag{6.4b}$$

the integral equation can be modified to

$$\check{f}(p,\phi) = \int_{-\infty}^{\infty} f(p\cos\phi - s\sin\phi, p\sin\phi + s\cos\phi)ds. \tag{6.5}$$

By using vector notation the above integral can be simplified. Let $\mathbf{x} = (x, y)$, then $f(\mathbf{x}) = f(x, y)$, also let $\xi = (\cos\phi, \sin\phi)$ and $\xi^{\perp} = (-\sin\phi, \cos\phi)$ where $\xi^{\perp}$ is a unit vector perpendicular to ξ. Introducing a scalar parameter t, the integral can be reduced to

$$\check{f}(p,\phi) = \int_{-\infty}^{\infty} f(p\xi + t\xi^{\perp})dt. \tag{6.6}$$

By writing the equation of the line ℓ (6.2) in terms of the vectors introduced, i.e.,

$$p = \xi \cdot \mathbf{x} = x\cos\phi + y\sin\phi, \tag{6.7}$$

and integrating over the entire space $\mathbf{R}^2$ using a Dirac δ function to select the appropriate plane, the transform equation becomes

$$\check{f}(p,\phi) = \iint f(\mathbf{x})\delta(p - \xi\cdot\mathbf{x})dx\,dy. \tag{6.8}$$

The double integral can now be replaced by an integral with respect to $\mathbf{x}$ giving the Radon transform equation in two dimensions:

$$\mathscr{R}f(\mathbf{x}) \;=\; \check{f}(p,\xi) \;=\; \int f(\mathbf{x})\delta(p - \xi\cdot\mathbf{x})d\mathbf{x}. \tag{6.9}$$

Three dimensions: It is a simple procedure to expand the previous argument to three dimensions. Let $\mathbf{x}$ be a vector in $\mathbf{R}^3$ defined by $\mathbf{x} = (x, y, z)$ with $d\mathbf{x} = dx\,dy\,dz$. The vector ξ is now defined by the equation

$$p = \xi \cdot \mathbf{x} = \xi_1 x + \xi_2 y + \xi_3 z, \tag{6.10}$$

and still has unit length. However, ξ now defines a plane in $\mathbf{R}^3$ rather than a line in $\mathbf{R}^2$, and the Radon transform equation is calculated by integrals over these planes instead of line integrals, although it still has the same form:

$$\mathscr{R}f(\mathbf{x}) = \check{f}(p, \xi) = \int f(\mathbf{x})\delta(p - \xi \cdot \mathbf{x})d\mathbf{x}. \tag{6.11}$$

Physically p is now the perpendicular distance of the plane from the origin, and the vector ξ is a unit vector which defines the planes orientation. It is now necessary to know all the plane integrals $\check{f}(p, \xi)$ for the Radon transform to be evaluated.

n dimensions: A point in n dimensional space ($\mathbf{R}^n$) is defined by

$$\mathbf{x} = (x_1, x_2, x_3, \ldots, x_n), \tag{6.12a}$$

and an $n-1$ dimensional hyperplane in n dimensional space ($\mathbf{R}^n$) is defined by

$$p = \xi \cdot \mathbf{x} = \xi_1 x_1 + \xi_2 x_2 + \xi_3 x_3 + \ldots + \xi_n x_n, \tag{6.12b}$$

with a unit vector ξ from the origin of $\mathbf{R}^n$, and normal to the plane p.

Again, by using the δ function form, the Radon transform is given by:

$$\mathscr{R}(f(\mathbf{x})) = \check{f}(p,\xi) = \int f(\mathbf{x})\delta(p - \xi \cdot \mathbf{x})d\mathbf{x}. \tag{6.13}$$

The resultant function $\check{f}(p,\xi)$ becomes the integral of the distribution across the entire hyperplane p.

6.1.1.2 Mathematical Representation of the Inverse Transform

The inverse Radon transform is more complex than the forward transform. The derivation [49] of the functional form is generally carried out for two distinct cases; one for odd dimensions, the other for even dimensions, which can be represented by the equations:

Odd dimension:

$$\mathscr{R}^{-1}(\check{f}(p,\xi)) = f(\mathbf{x}) = \frac{1}{2(2\pi i)^{n-1}} \int_{|\xi|=1} \left(\frac{\partial}{\partial p}\right)^{n-1} \check{f}(\xi \cdot \mathbf{x}, \xi)\, d\xi \tag{6.14a}$$

Even dimension:

$$\mathscr{R}^{-1}(\check{f}(p,\xi)) = f(\mathbf{x}) = \frac{1}{2(2\pi i)^{n-1}} \int_{|\xi|=1} d\xi \int_{-\infty}^{\infty} dp\, \frac{\left(\frac{\partial}{\partial p}\right)^{n-1} \check{f}(p,\xi)}{p - \xi \cdot \mathbf{x}} \tag{6.14b}$$

Generally, the inverse transform is of more use in two dimensions, simply because it is extremely difficult to measure surface integrals experimentally. The required line integrals are easily measured. For example X-ray absorption through a sample is calculated by measuring the X-ray intensity as a beam emerges from a sample, and comparing this with the incident intensity. The two dimensional form of the inverse transform is given by

$$f(r,\theta) = \frac{-1}{2\pi^2}\int_0^{\pi} d\phi \int_{-\infty}^{\infty} \frac{\check{f}(p,\xi)}{p - r\cos(\phi-\theta)} dp. \tag{6.15}$$

which corresponds to the reconstruction of a distribution from a set of line integrals through the distribution.

6.1.1.3 Physical Meaning

The physical meaning of the transform is more easily understood, if a two dimensional distribution is considered. For a two dimensional point distribution in Euclidean real space $\mathbf{R}^2$ defined as $f(x,y)$ the Radon transform will produce a complete set of side-on, line-profiles denoted by $\check{f}(p,\phi)$, where ϕ is the angle at which the projection is made and p is the perpendicular distance from the centre of the distribution that the projection lies. Two examples of these projections are shown in figure 6.2, namely $\check{f}(p,\phi_1)$ and $\check{f}(p,\phi_2)$. Each of the projections has a constant ϕ, as all the line integrals are constructed at a particular angle through the distribution. However the full profile is still a function of p, because values at all perpendicular distances must be measured to build the complete profile; each discrete value of p contributing one point to the profile.

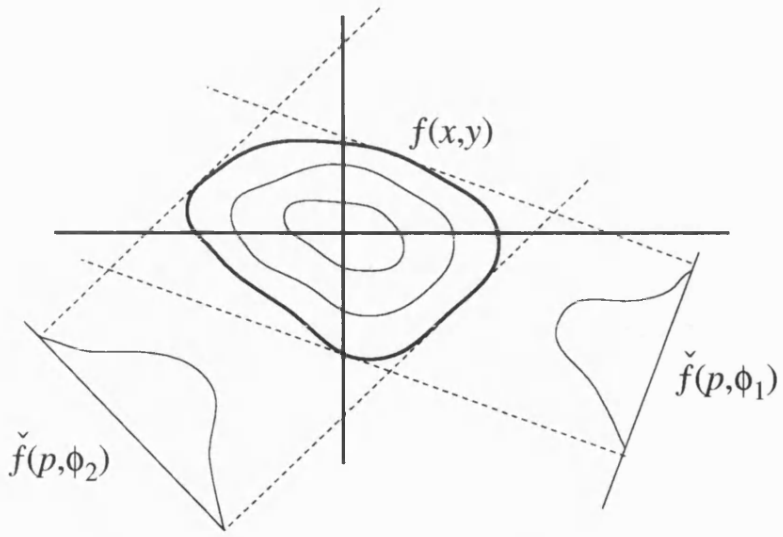

Figure 6.2: Projections of a point distribution $f(x, y)$ at two angles ϕ_1 and ϕ_2.

From the distribution it is possible to make projections at all angles of ϕ between 0 and π. The projections with $\phi \in [\pi, 2\pi)$ are simply the rear views of the projections with $\phi \in [0, \pi)$ and need not be calculated since the two sets are identical. The inverse transform uses the set of profiles to reconstruct the original two-dimensional distribution. To perform this accurately, a large number of such profiles are required, for as many angles ϕ as possible, since fewer profiles results in information about the distribution being discarded.

6.1.2 The Abel Transform

In order to reconstruct the distribution $f(x, y)$ using the Radon transform, the complete set of projections $\check{f}(p, \phi)$ must be measured. In two dimensions this implies that $\check{f}(p, \phi)$ must be measured for $\phi \in [0, \pi)$. However if the distribution has circular symmetry, all of the profiles will be identical regardless of the angle

ϕ at which the projection was made. This can be represented as:

$$\check{f}(p,\phi) \rightarrow \check{f}(p) \qquad \forall\ \phi \in [0,\pi). \tag{6.16}$$

Figure 6.3 demonstrates the symmetry aspect, showing that only one side-on projection is required. The point distribution can now be defined by $f(r)$, rather than $f(x,y)$, as there is no ϕ dependence, and the forward Abel transform will produce the side-on projection $\check{f}(p)$.

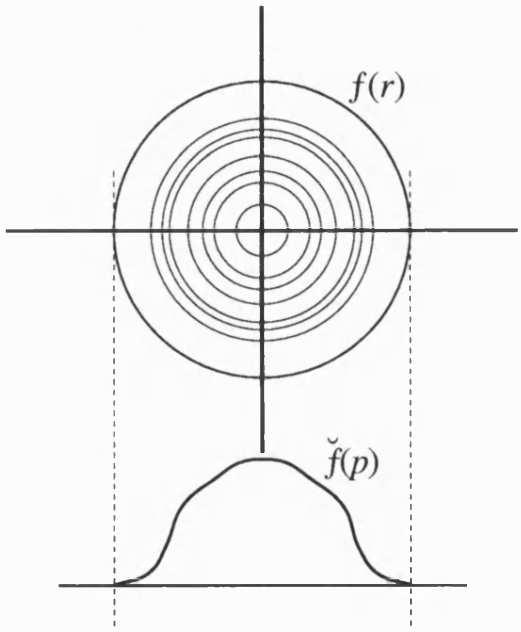

Figure 6.3: Radial symmetry requiring a single side-on projection

The Abel transform pair, applicable to two dimensional circular symmetry, have been derived from the Radon transform pair by Bracewell [39]. Transform pairs for hyperspherical symmetry in n dimensions can be derived [49]; however these are not required for this experiment.

The forward transform is given by:

$$\mathscr{A}(f(r)) = \check{f}(p) = 2\int_p^\infty \frac{f(r)\,r}{(r^2-p^2)^{1/2}}dr, \tag{6.17a}$$

and the inverse transform by:

$$\mathscr{A}^{-1}(\check{f}(p)) = f(r) = \frac{-1}{\pi}\int_r^\infty \frac{d\check{f}(p)}{dp}\frac{1}{(p^2-r^2)^{1/2}}dp. \tag{6.17b}$$

These two equations form the core of the analytical process used to extract temperature distributions from the images of the heated samples.

6.2 Numerical Implementations

Experimental measurement produces line integrals at discrete intervals, rather that a continuous distribution. As a result the integral equations given previously have to be modified in order for the calculations to be performed. Because the inverse transform is usually the only one of importance in most experimental situations, various implementations have been derived by several groups. The forward transform is not generally of any use in experimental applications, as the actual process of measurement produces output which is the forward transform of the quantity to be determined.

The simplest implementations of the inverse Abel transform convert the integral into a summation by considering that the output from any measurement is in the

form of small strip integrals across the measured distribution. One such method, and probably the simplest to understand, was proposed by Nestor and Olsen [50]. This became a standard numerical implementation, and the basis from which many more were derived. An outline of the technique for two dimensional line (or strip) integrals is given in section 6.2.1. Improvements on this simple method involve interpolating piecewise polynomials between sets of data points either to smooth the original data [51–53] or to allow these polynomials to be inverted directly from the integral equation [48,54].

Other methods have also been derived for fitting a high order polynomial through the entire data set, again to invert directly from the integral equation. Polynomials that have been applied include Tchebyschev [55] and a combination of Laguerre and Hermite [56]. Fourier methods are also common [57,58] where the Fourier transform of the inverse Abel transform equation is used to remove the problem of the derivative term, since derivatives are easily calculated in Fourier space. Backprojection and other recursive techniques have been suggested [59–61], where the two dimensional distribution is reconstructed from the outside, inner points being calculated from the newly inverted section of the distribution. These techniques are commonly called 'onion-peeling' methods. A brief review of the above (and other) techniques can be found in Ref. [59].

6.2.1 The Nestor and Olsen Method

The Nestor and Olsen method [50] of numerically performing the inverse Abel transform has been used in many physical situations. Its use in measuring ra-

dial temperature distributions in diamond-anvil cells was first reported by Heinz and Jeanloz in 1987 [6]. In this technique, the integral form of the inverse Abel transform (equation 6.17b) is reduced to a summation of the discrete data points making up the side-on projection $\check{f}(p)$. This is represented as:

$$f_k(r) = \frac{-1}{\pi} \sum_{n=k}^{N} B_{kn} \check{f}(p_n) \tag{6.18}$$

where the B_{kn} values are constant coefficients determined from the index numbers k and n (ref. equations 6.28 and 6.29).

6.2.1.1 Mathematical derivation

In figure 6.4 the radial distance from the centre of the sample is represented by r, and the radius of the sample by R. The linear distance of a particular line profile from the centre of the sample is represented by x, with the centre being at $x = 0$. Since the sample is circularly symmetric, only positive x need be considered.

Let the function $I(\lambda, x)$ denote the set of line integrals across the surface, and $I(\lambda, r)$ be the required intensities as a function of radial distance. The function $I(\lambda, x)$ is thus the Abel transform of the function $I(\lambda, r)$; hence to obtain $I(\lambda, r)$ from $I(\lambda, x)$ the inverse Abel transform is required. The inverse Abel transform is given by:

$$I(\lambda, r) = \frac{-1}{\pi} \int_r^{\infty} (x^2 - r^2)^{-1/2} \frac{dI(\lambda, x)}{dx} dx. \tag{6.19}$$

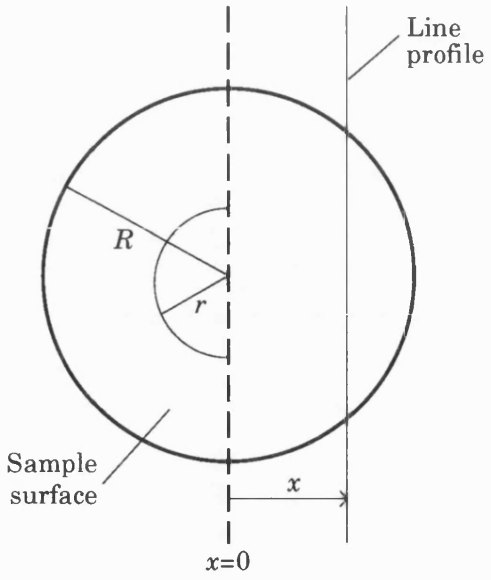

Figure 6.4: Sample surface showing the labelling convention

To calculate the radial distribution at a radius r, only line profiles for $x > r$ are required, hence the lower limit of the integral is r. Since the function $I(\lambda, r)$ is zero for $r > R$, the upper limit in equation 6.19 may be reduced from ∞ to R. The equation can be simplified using a variable transformation such that $u = x^2$ and $v = r^2$, therefore the equation becomes:

$$I(\lambda, r) = \frac{-1}{\pi} \int_{r^2}^{R^2} (u - v)^{-1/2} \frac{dI(\lambda, u)}{du} du. \tag{6.20}$$

The x-axis is now divided into N strips of equal width a, with the position of the n^{th} strip being given by $x_n = na$. The sample is also split into radial sections of width a, with r_k being the radius of the k^{th} radial section (so $r_k = ka$). The surface is now considered to be as shown in figure 6.5, made up of discrete radial (and also linear) divisions.

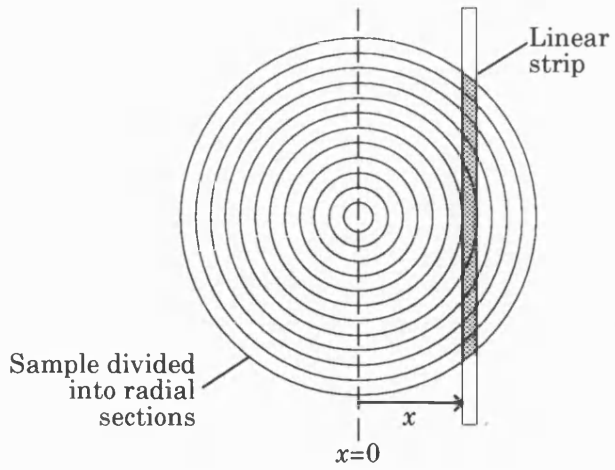

Figure 6.5: Sample surface showing positions of radial divisions with a typical linear strip.

The integral in equation 6.20 can be considered as the sum over all slits from the required radius to the edge of the sample. Therefore it can be rewritten as:

$$I(\lambda, v_k) = \frac{-1}{\pi} \sum_{n=k}^{N-1} \frac{dI(\lambda, u)}{du} \int_{(an)^2}^{(a(n+1))^2} (u - (ak)^2)^{-1/2} du. \tag{6.21}$$

If the slit width is small compared to the dimensions of the sample surface, it is reasonable to assume that I is linear in v $(= r^2)$ across the slit. Figures 6.6(a) and 6.6(b) illustrate this, the function being smooth and the curve being almost linear between the two values $I(\lambda, an)$ and $I(\lambda, a(n+1))$. The assumption of linearity means that the differential term in equation 6.21 may be replaced by a difference term. This is necessary since only discrete values of $dI(\lambda, u)/du$ are available, rather than an explicit form. In terms of variables used here this can be written as:

$$\frac{dI(\lambda, u)}{du} = \frac{I_{n+1}(u) - I_n(u)}{(a(n+1))^2 - (an)^2}. \tag{6.22}$$

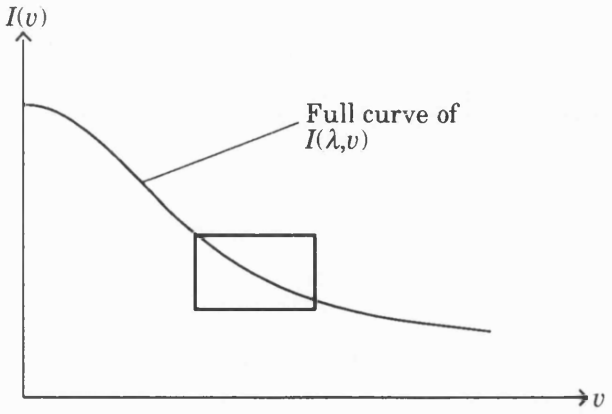

(a)

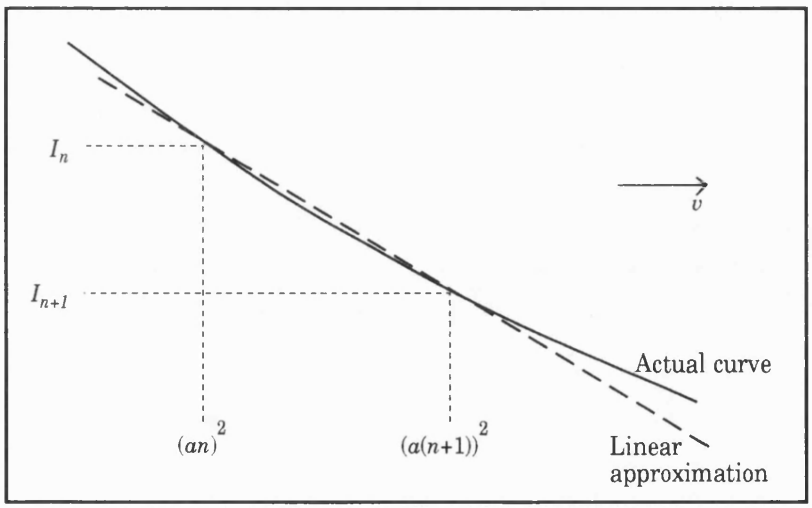

(b) Magnified view of above figure.

Figure 6.6: Intensity I as a smooth function of the distance parameter v $(= r^2)$.

Substituting equation 6.22 into equation 6.21, the following is obtained:

$$I(\lambda, v_k) = \frac{-1}{\pi} \sum_{n=k}^{N-1} \frac{I_{n+1}(u) - I_n(u)}{(a(n+1))^2 - (an)^2} \int_{(an)^2}^{(a(n+1))^2} (u - (ak)^2)^{-1/2} du. \quad (6.23)$$

The integral term can now be evaluated to give

$$I(\lambda, v_k) = \frac{-1}{\pi} \sum_{n=k}^{N-1} \frac{I_{n+1}(u) - I_n(u)}{(a(n+1))^2 - (an)^2} \left[(u - (ak)^2)^{1/2} \right]_{(an)^2}^{(a(n+1))^2}. \quad (6.24)$$

On Expansion of equation 6.24: two separate terms remain; one a function of u, the other independent of u. By transforming coordinates back to x and r, the following is obtained:

$$I(\lambda, r_k) = \frac{-1}{\pi} \sum_{n=k}^{N-1} A_{kn} \left(I_{n+1}(\lambda, x) - I_n(\lambda, x) \right), \quad (6.25a)$$

where

$$A_{kn} = \frac{((n+1)^2 - k^2)^{1/2} - (n^2 - k^2)^{1/2}}{2n+1}. \quad (6.25b)$$

This summation was rewritten by Nestor and Olsen [50] in such a way that calculating differences between data points is not required. Expanding out all terms gives the following:

$$I(\lambda, r_k) = \frac{-1}{\pi} \left\{ \begin{array}{ll} & A_{kk}(I_{k+1} - I_k) \\ + & A_{kk+1}(I_{k+2} - I_{k+1}) \\ + & \ldots \\ + & A_{kN-2}(I_{N-1} - I_{N-2}) \\ + & A_{kN-1}(I_N - I_{N-1}) \end{array} \right\}. \quad (6.26)$$

Terms can be collected together in terms of I:

$$I(\lambda, r_k) = \frac{-1}{\pi} \left\{ \begin{array}{ll} & I_k(-A_{kk}) \\ + & I_{k+1}(A_{kk} - A_{kk+1}) \\ + & \ldots \\ + & I_{N-1}(A_{kN-2} - A_{kN-1}) \\ + & I_N(A_{kN-1})) \end{array} \right\}, \tag{6.27}$$

which gives the final result

$$I(\lambda, r_k) = \frac{-1}{\pi} \sum_{n=k}^{N} B_{kn} I_n, \tag{6.28}$$

where

$$B_{kn} = \left\{ \begin{array}{ll} -A_{kk} & \text{for } n = k \\ A_{kn-1} - A_{kn} & \text{for } n > k \end{array} \right. \tag{6.29}$$

Now that a numeric implementation of the inverse Abel transform has been derived, this may be used in the mathematical analysis of a data set, allowing the reconstruction of the temperature profile on a hot-spot.

Chapter 7

Verification of Experimental System

It is important to ensure that the analysis system reproduces the hot-spot temperature correctly. To perform this, a sample with a known temperature distribution has been examined. Since melting points are to be measured directly from the reconstructed profiles, a second verification process has been performed where a material with a known melting temperature is examined. These two verification procedures are used to demonstrate that the experimental system and the subsequent mathematical analysis procedures are capable of reconstructing the temperature distribution generated across a material. The two cases considered are a white light source with a calibrated spectral output (for known temperature reconstructions) and polycrystalline iron (for melting point investigations).

7.1 Analysis of a Known Temperature Source

A calibrated white light source was positioned behind a pinhole of known radius. The lamp was a 12V, 100W tungsten halogen projector lamp constructed out of fused silica, with a grit blasted silica envelope to provide a good diffusive surface. Its spectral output was measured at the National Physical Laboratory (NPL) [36] at 5nm steps between 300nm and 800nm, and corresponds to a correlated colour temperature of 2977K (see figure 7.1).

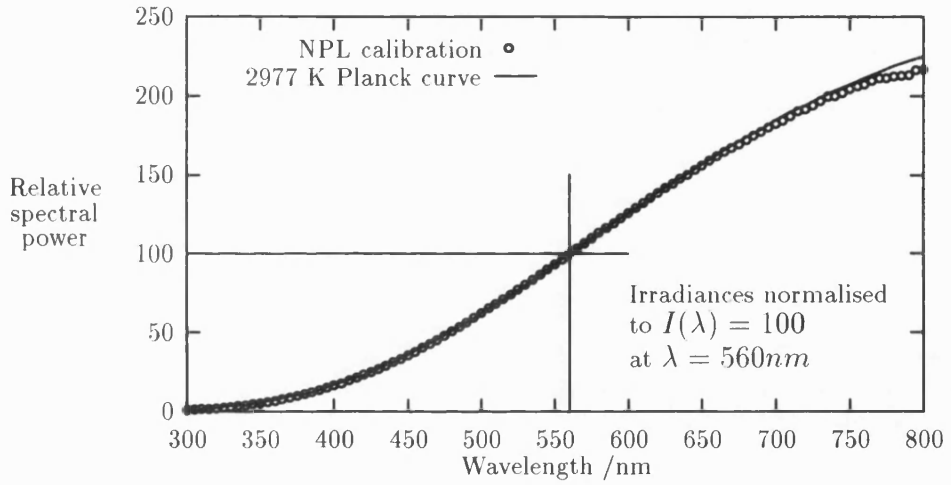

Figure 7.1: Spectral irradiance of known white light source

The lamp was shone through a circular hole of diameter 120μm (measured on a travelling microscope) laser drilled in a piece of 85μm thick steel shim, which was mounted at the focal point of the collecting (and laser focusing) optics. This produced an effective sample with a constant colour temperature across its surface of 2977K. As the original sample characteristics are known, it is thus possible to

gauge how accurately the analysis procedure is performing its reconstruction.

The collection and focusing optics used in this experiment produced a vertical magnification factor of 4.286 since the focal lengths of the lenses L_1 and L_2 (in figures 3.2 and 3.8 respectively) were 7cm and 30cm. Therefore the height of the image formed on the CCD detector surface was 514μm, which corresponds to a spectral image covering 23 pixels vertically.

A set of temperature profiles were generated with a basic analysis system of: Fourier symmetrisation, Nestor and Olsen inversion and non-linear regression. Three smoothing methods were applied in separate analyses: no smoothing, Fourier smoothing, nine point moving average. The three resulting profiles are shown in figure 7.2 (the true temperature of 2977K is also marked), with an expanded view of the flat section of the curve shown in figure 7.3.

The non-smoothed profile is the same width as the true temperature distribution across the pinhole. This is seen as the outermost reconstructed point being at pixel number 11. However the outermost point is very inaccurate ($\approx$5200K). This is due to the large gradient that occurs at the edge of the true temperature distribution. The inverse Abel transform includes a derivative term, and at this point the large gradients cause large errors to be introduced. Because the internal points in the profile are calculated as functions of all points from the point in question to the edge, this gradient problem is carried through into the inner regions of the reconstructed profile. This is observed as the overestimation of temperature towards the centre of the profile. Another problem at the edge of the image is that the intensity of light being detected is much lower than at the centre. The ripple

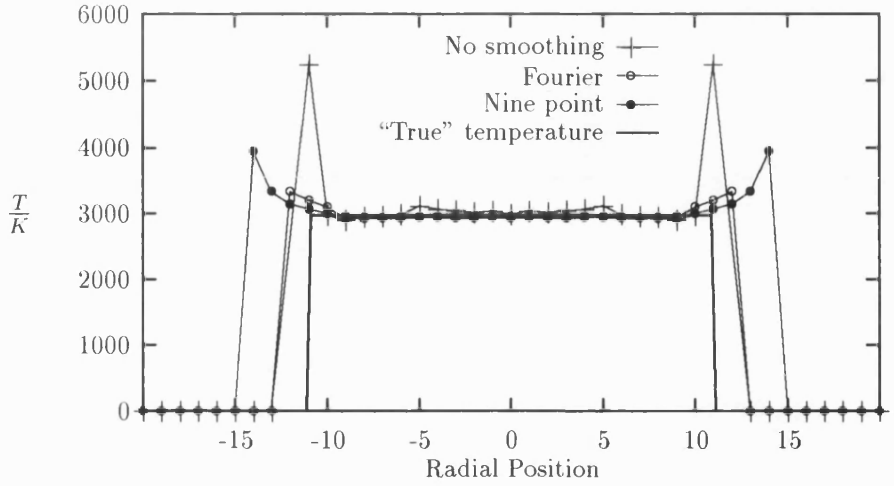

Figure 7.2: Comparison of generated temperature profiles for a known temperature source using different smoothing techniques.

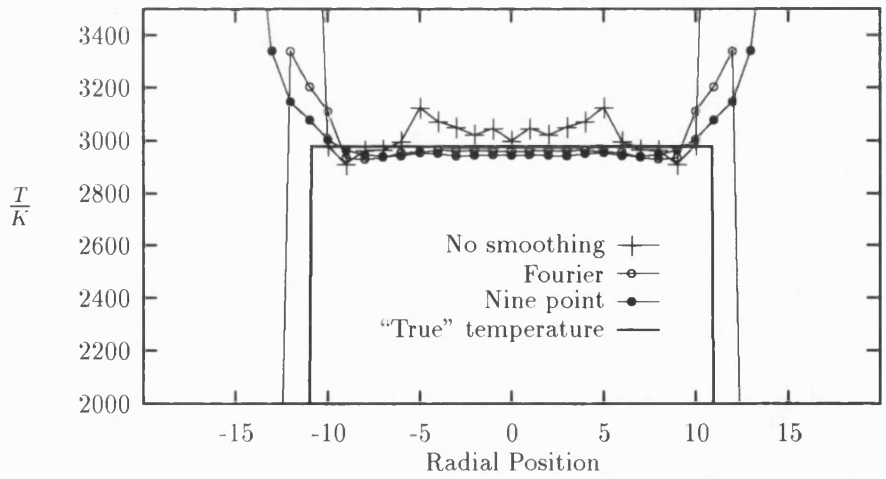

Figure 7.3: Expanded view of the flat section of the profile in figure 7.2.

in the spectral intensity caused by the dichroic mirror cannot removed totally at these low intensities and the resulting temperature fits are therefore less reliable.

The two smoothing methods reduce the edge spike and also model the inner part of the profile better. However both smoothing methods produce profiles which are wider than the true temperature distribution. This widening is reasonable, since the smoothing process will smear the edge intensities to pixel positions outside the extent of the true spectral image. The centre of the smoothed profiles lie very close to the true temperature, underestimating by approximately 40K between pixel position -9 and 9 (on figure 7.3).

This particular analysis demonstrates that the experimental and analysis systems are capable of reconstructing a known temperature profile.

7.2 Melting of Polycrystalline Iron

The experiment outlined in section 7.1 demonstrates that the apparatus is able to reconstruct a temperature profile from a spectral image recorded by the CCD detector (see section 3.2.5). This present procedure is used to demonstrate that melting point information can be obtained from these generated temperatures profiles.

The ability to measure melting points depends on the constant temperature observed while a material is melting, due to the latent heat of melting. This constant temperature is observed as a small flat section in the side of the profile, and cor-

responds to a ring of melting material surrounding a central area of melt, as illustrated by figure 7.4.

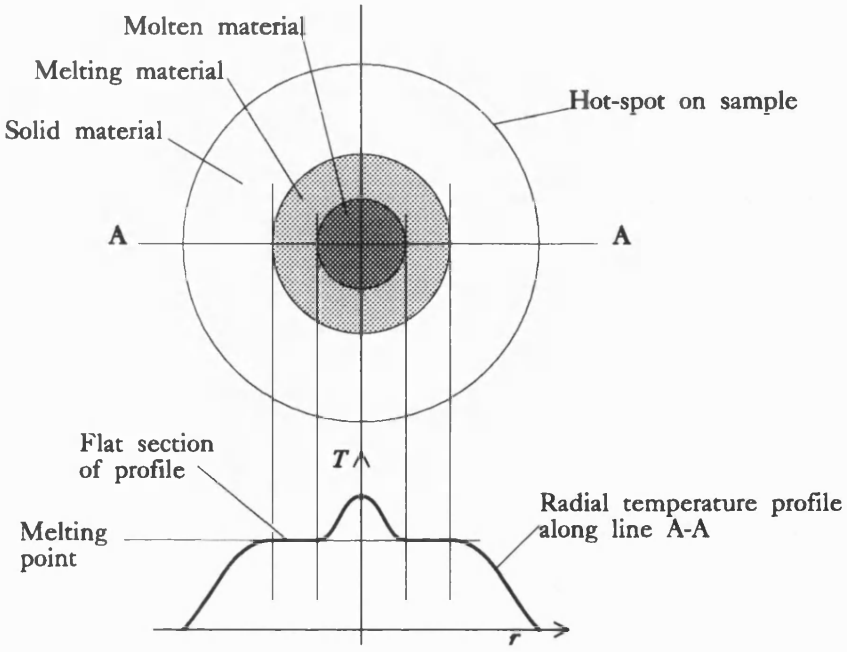

Figure 7.4: Ring of melting material causing flat section in profile.

A set of measurements have been performed on a sample of 99.99% pure, polycrystalline iron, of dimension 2cm×1cm×0.3cm, mounted in a clamp at the focal point of the laser focusing lens (L_1 in figure 3.2). The exact positioning of the sample was performed using the heating laser at very low power, moving the sample along the axis of the beam until a very small glowing spot was observed. At such low powers there is only sufficient heating when the area illuminated by the laser is a minimum, i.e., at the focal point (and beam waist position).

The sample was heated with the laser flash lamp current set at 30A and then 31A to produce a bright glowing spot in each case, the cylindrical focusing optics being used to form a focused image of the hot-spot within the 100μm wide spectrograph

Radial position	T / K 31A	Radial position	T / K 30A
11	1794 ± 51	8	1784 ± 140
12	1714 ± 58	9	1856 ± 152
13	1829 ± 66	10	1822 ± 211
14	1748 ± 78	11	1762 ± 287
15	1843 ± 116	12	1786 ± 546
Mean	1777 ± 63		1812 ± 48

Table 7.1: Temperature values across flat section of iron profiles (rounded to nearest integer).

slit. A scan of each spot was then taken with exposure of 750ms, 5 data scans being averaged to produce a final image.

The OMA2T program was used to analyse both data sets, to calculate the temperature profile across the hot-spot. The centre position of the data set was determined (using equal integral method, section 5.3.2) as 44.0 ± 0.0 and 44.4 ± 0.9 for the 30A and 31A cases respectively. The analysis stages used in the profiling were: Fourier symmetrisation, Nestor and Olsen Inversion, iteratively reweighted linear regression. No artefact removal or smoothing was required as no spots were observed on the CCD image. The resulting temperature profiles are shown in figures 7.5(a) and 7.5(b), with a comparison of the two curves (without error bars for clarity) being shown in figure 7.6.

The flat sections of the two profiles consist of the temperature values listed in table 7.1, which are then averaged to produce an estimate of the melting point, also listed in 7.1. Both values agree well with the quoted values (for pure iron) of 1813K [62] and 1808K [63], these values being within the experimental error. The

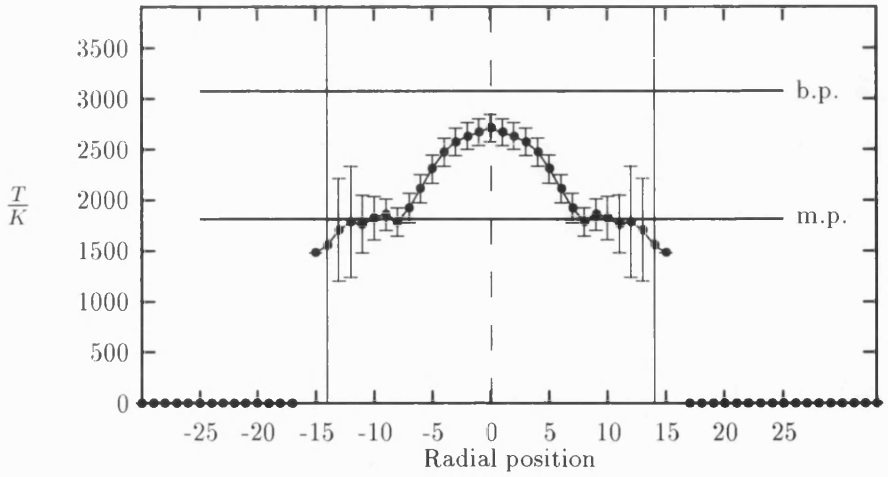

(a) 30A flash lamp current

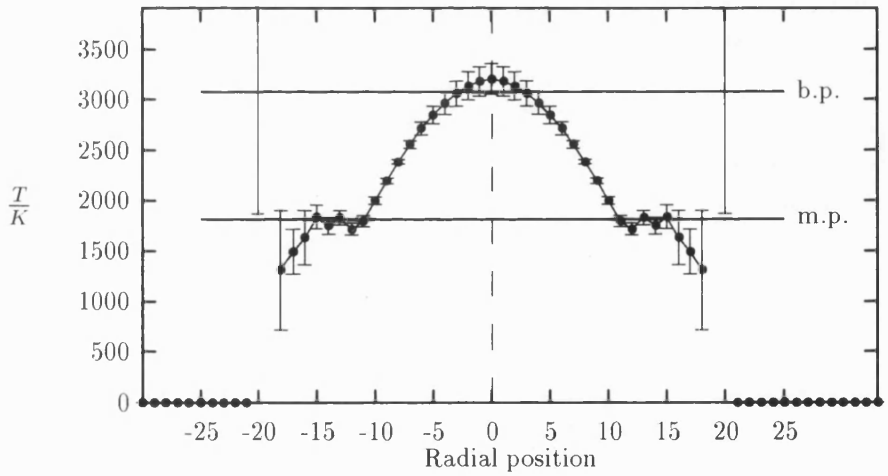

(b) 31A flash lamp current

Figure 7.5: Temperature profiles generated on iron sample

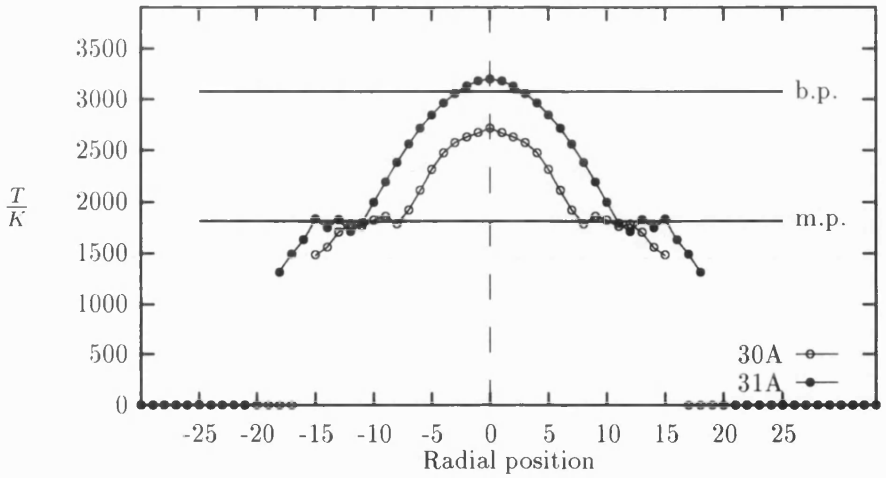

Figure 7.6: Melting point of iron observed from scans at flash lamp current of 30A and 31A

31A case does appear to reach temperatures higher than the quoted values of the boiling point of iron (3073K [62] and 3023K [63]); however the error bars in that region of the curve do stretch below that temperature.

This experiment demonstrates that the system used here is capable of accurately modelling the temperature profile across a laser heated spot, and provides information enabling melting point characteristics to be determined accurately.

Chapter 8

Melting Experiments on Uranium Dioxide

8.1 Background

The most common fuel used in thermal reactors is ceramic uranium dioxide in the form of long thin rods. As a result, a great deal of interest has been generated in the thermodynamic properties of UO_2 to enable accurate computer models of the conditions inside a reactor core to be constructed.

Uranium dioxide has a wide range of stoichiometries [64], the variation of which is believed to have a large effect on its physical and thermodynamic properties. The stoichiometric form, UO_2, has the cubic fluorite structure as shown in figure 8.1 with lattice constant of 5.470Å [65]. Potential models have been derived [66] for this structure which assume that there are full ionic charges of $+4$ and -2 on the uranium and oxygen. Such models have been useful in reproducing many of

the experimentally determining physical properties. The UO_2 fluorite structure is capable of a large amount of oxygen disorder [67]. Furthermore the uranium ion is easily oxidised from U^{4+} to U^{5+} via the mechanism [1,68]:

$$2U^{4+} + \frac{1}{2}O_2 \rightarrow 2U^{5+} + O_{int}^{2-}, \tag{8.1}$$

where the O_{int}^{2-} is an interstitial oxygen. This process results in the ability of uranium dioxide to form hyperstoichiometric structures up to $UO_{2.25}$. Higher oxygen concentrations results in the formation of other phases: U_4O_9, U_3O_8, UO_3 [64,69,70]. The phase diagram for the U–O system is given in Dawson [64].

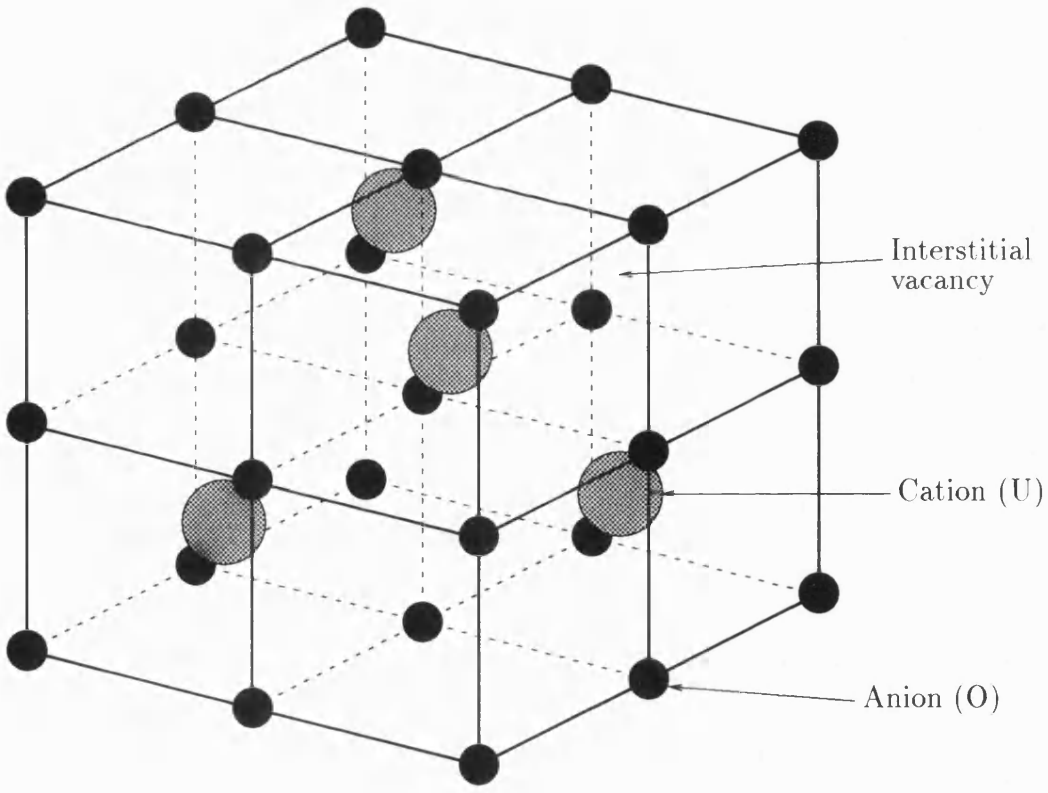

Figure 8.1: Uranium dioxide cubic fluorite structure.

For investigations of the effect of stoichiometry on thermal properties, it is essential to retain the sample in its original stoichiometry during the experimental procedure. When UO_2 is heated, it oxidises easily unless it is contained within a reducing atmosphere. Hyperstoichiometric forms also require reducing atmospheres, usually CO/CO_2 mixtures, the proportion of CO being determined by both the oxygen content of the sample and the temperature to which the sample is to be heated. Therefore, the experimental system discussed in chapters 3 and 4, in particular the Controlled Atmosphere Chamber, has been designed to allow the suitable gas mixtures to be used, permitting measurements on samples of stoichiometries up to $UO_{2.2}$.

8.2 Experimental Results

Stoichiometric, depleted UO_2 (Harwell sample number K1118)[1] has been investigated, of dimension 15.50mm×3.74mm×1.50mm, as illustrated in figure 8.2, and weighing 0.750g. The sample volume was calculated as 69.58mm^3 (taking into account the two indentations), and its density as 10.78gcm^{-3}. Given the density of fully dense UO_2 as 10.96gcm^{-3} [63,64], the sample fractional porosity (f), assuming no significant impurity concentration, was then calculated to be:

$$\begin{aligned} f &= 1 - \frac{\text{Measured density}}{\text{Fully-dense density}} \\ &= 0.016 \end{aligned} \tag{8.2}$$

[1]One of three samples supplied by R. Williamson, Reactor Fuel Division, Harwell Laboratories, U.K.

The porosity of the sample is an important consideration in the calculation of thermal conductivities [71]; however for melting points its effect is negligible.

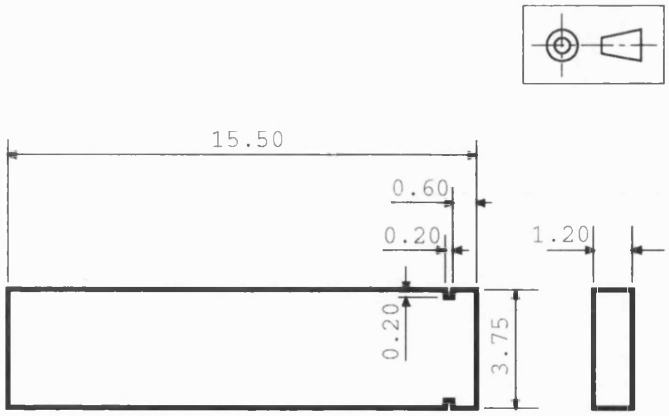

Figure 8.2: Schematic diagram showing the dimensions of the UO_2 sample used for melting point measurements (dimensions in mm)

Two sets of experiments were performed on this UO_2 sample: X-ray analysis of the bulk structure, laser heating measurements to determine its melting point. The results of these experiments are considered separately in the following sections.

8.2.1 X-Ray analysis of polycrystalline UO_2 samples

To investigate the purity of the polycrystalline sample, a set of shallow angle X-ray powder diffractometry experiments were performed; the reflection spectra obtained are illustrated in figure 8.3. This analysis was performed using a Philips diffractometer with automatic powder diffraction software (PC-APD) and the powder diffraction file. The incident X-ray radiation was dichromatic, consisting of the copper $K_{\alpha 1}$ (1.54060Å) and $K_{\alpha 2}$ (1.54439Å) lines in the intensity ratio 2:1. As a result, each of the reflection peaks in the measured spectrum consists of

a closely spaced doublet, with the peak corresponding to the $K_{\alpha 2}$ radiation (i.e. at the slightly larger diffraction angle 2Θ) being half the intensity of the $K_{\alpha 1}$ reflection. This splitting effect is more resolved at high reflection angles and may be observed in figure 8.3 for peaks at 2Θ above 50°.

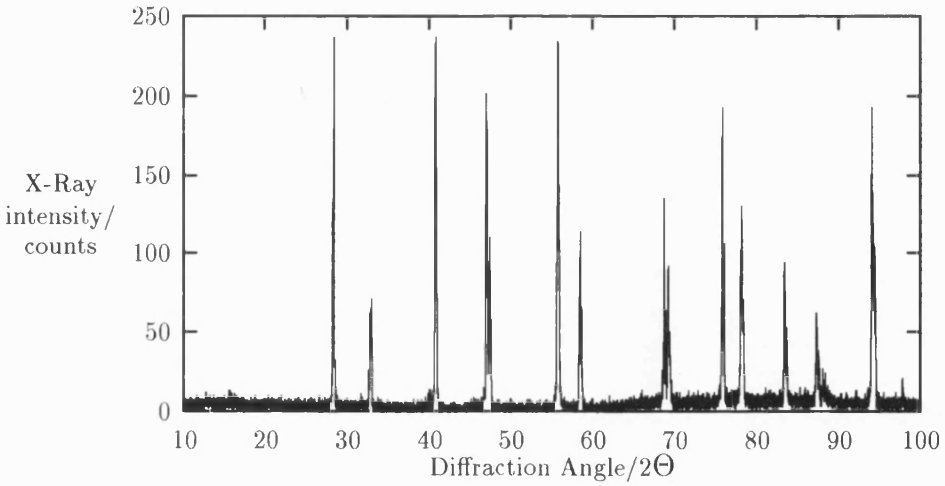

Figure 8.3: Measured X-ray diffraction spectrum for polycrystalline UO_2

The spectrum contains fifteen peaks (doublets), nine of which were matched to bulk UO_2 sample, a further five being matched to the element iridium, with one peak being outside the range of the available diffraction data. No other peaks were observed in the spectrum. The presence of iridium peaks is to be expected in these samples, since part of the manufacturing procedure involved suspending the samples from an iridium wire in a furnace during annealing [72]. The diffusion of iridium into the sample is restricted to one end of the UO_2 sample, where the wire is attached (the indentations in figure 8.2). Further diffraction experiments concentrating on the bulk sample away from the indentations showed an appreciable decrease in the height of the iridium lines, and hence a much reduced

concentration of this element in that region of the sample. Table 8.1 lists the measured diffraction angles (2Θ for the $K_{\alpha 1}$ reflection only), calculated *d*-spacings and the matched UO_2 and Ir lines [73, 74]. This table demonstrates the good match between the published *d*-spacings and the experimental data for both the bulk UO_2 and the iridium impurity.

Measured (sample K1118)		ICDD PDF values			
		UO_2		Ir	
Angle 2Θ/°	*d*-spacing/Å	*d*	Plane	*d*	Plane
28.3	3.151	3.1530	111		
32.8	2.728	2.7330	200		
40.7	2.215			2.2170	111
47.0	1.932	1.9330	220		
47.4	1.916			1.9197	200
55.8	1.646	1.6474	311		
58.4	1.579	1.5782	222		
68.7	1.365	1.3670	400		
69.2	1.357			1.3575	220
75.8	1.254	1.2543	331		
78.1	1.223	1.2224	420		
83.5	1.157			1.1575	311
87.3	1.116	1.1158	422		
88.1	1.108			1.1082	222

Table 8.1: Matched lines for X-ray diffraction spectrum obtained from polycrystalline UO_2 containing Ir as an impurity.

8.2.2 Heating experiments

The UO_2 sample was mounted on a specially constructed plate in the Controlled Atmosphere Chamber (CAC). See figure 3.13 on page 53 for details of the CAC assembly. The CAC was flushed with a $2\%H_2/Ar$ reducing gas mixture, a positive

pressure being maintained by a bubbler attached on the waste gas pipe from the CAC. The flush ensured that the UO_2 sample did not oxidise during heating, thus retaining its stoichiometry.

A series of laser heating runs was performed, one image being recorded for each laser power setting listed in table 8.2 below.

Scan no.	Power/A	Exposure/ms
1	21	300
2	23	100
3	25	30
4	*27	10
5	25	30
6	24	70
7	23	90
8	22	150
9	21	300

*Sample cracked during measurement

Table 8.2: Data scans recorded on UO_2 sample K1118

Images 1–4 were recorded with the laser focused onto the same area of sample to provide a consistent surface, thus allowing a comparison of images and temperatures. However, with the laser flash lamp current set at 27A, the bright spot disappeared, and on closer inspection a large crack was observed across the width of the sample. Therefore the laser was being focused within the crack, hence no heating occurred and no spot was visible. Images 5–9 were subsequently recorded with the sample being moved between successive images (to prevent further cracking of the sample).

After examination of the recorded images with the URT package (see appendix A),

it was observed that the peak intensities moved toward the shorter wavelength end of the image with increased flash lamp current, confirming that the sample temperature increased as expected. No dark or light spots were present in the image, hence no artefact removal was performed during the analysis procedure.

When temperature analysis was performed using the OMA2T program, data scans with flash lamp current below 24A were found to have peak temperatures below 1500K. This is the minimum temperature that can be reliably reconstructed from data restricted to the spectral range of the experimental apparatus. Therefore data scans 1, 2, 7, 8, and 9 were unsuitable for temperature profiling; however now that experiments have been performed it is known that to produce sufficient heating in UO_2 samples for this type of analysis, laser flash lamp currents above 23A must be used.

Initial analysis of the data was performed using the minimum number of analysis procedures: Fourier symmetrising (section 5.5), Nestor & Olsen inversion (sections 5.6 and 6.2.1), iteratively reweighted linear regression (section 5.7.4). Temperature profiles were also calculated with either Fourier smoothing or nine-point smoothing along the vertical tracks in an effort to reduce noise and provide cleaner data for the inversion process. The two heating runs that produced temperatures above 1500K (5 and 6) are now considered in turn, the lower power case first.

The temperature profiles obtained from scan 6 in table 8.2 (flash lamp current 24A), using the non-smoothed and Fourier smoothing procedures are shown in figure 8.4. The profile obtained using nine-point smoothing is very similar to both

these curves (figure 8.4), and is therefore not shown. Owing to the type of fitting procedure used (see section 5.7.6), the errors seen at the centre of the profile are larger than at the outer part of the curve.

The three profiles are very similar, and superimposing them onto one set of axes shows that the smoothing process does not affect the overall shape of the profile, but does remove some of the noisier spikes. The comparison is shown in figure 8.5. The peak temperatures (measured at the centre of the spot) are listed in table 8.3, and are all below the quoted value of melting point for UO_2, hence no flat section

Smoothing	T/K
None	2749 ± 1114
Fourier	2737 ± 786
Nine-point	2723 ± 737

Table 8.3: Measured UO_2 peak temperatures from three smoothing methods.

is observed in the profile (see figure 7.4 in section 7.2). The estimated errors on these temperatures are large because the resolution of the linear regression methods decreases with increasing temperature, as discussed in section 5.7.6.

The profile obtained using the nine-point smoothing method extends further to the sides than the other two curves, because the smoothing process itself necessarily spreads the data through the surrounding positions. This spread is then considered in the regression procedure and temperatures measured for the extended areas of the data.

The temperatures generated at an increased laser flash lamp current of 25A (scan

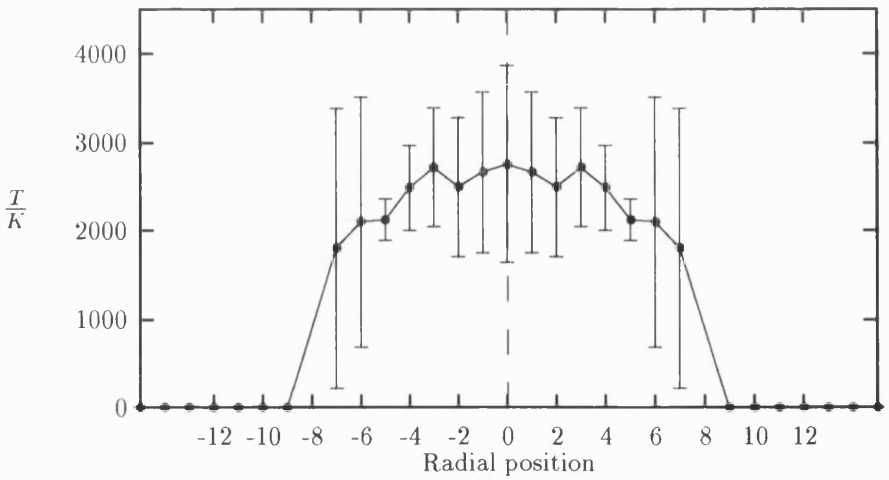

(a) No smoothing

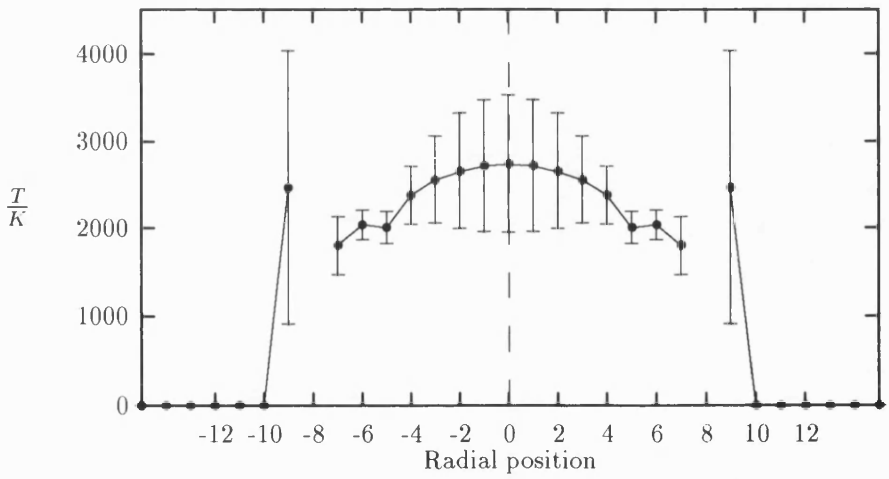

(b) Fourier smoothing

Figure 8.4: UO_2 profiles obtained with a laser flash lamp current of 24A using iteratively reweighted regression for temperature fitting.

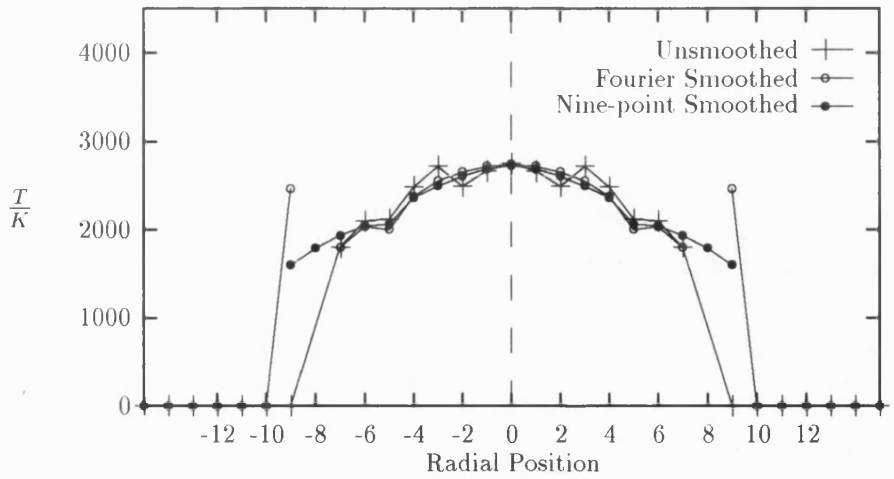

Figure 8.5: Comparison of smoothing effects on the 24A UO_2 profile

5 in table 8.2) were greater than those obtained in the 24A case as would be expected. A comparison of the temperature profiles obtained at the two flash lamp currents is shown in figure 8.6. The horizontal line is set at the generally accepted value of melting temperature of 3120K [75]. It is clear that in the 25A case the centre of the sample is heated above the melting temperature and a ring of melt is observed (compare with figure 7.4).

The peak temperatures at the centre of the profile exceeded 3000K, rendering the linear regression methods unsuitable. Therefore this data set has been analysed using the non-linear regression process discussed in section 5.7.5. Again three analyses have been performed: without smoothing, with Fourier smoothing, with nine-point smoothing. The resulting profiles (unsmoothed and Fourier) are shown in figure 8.7.

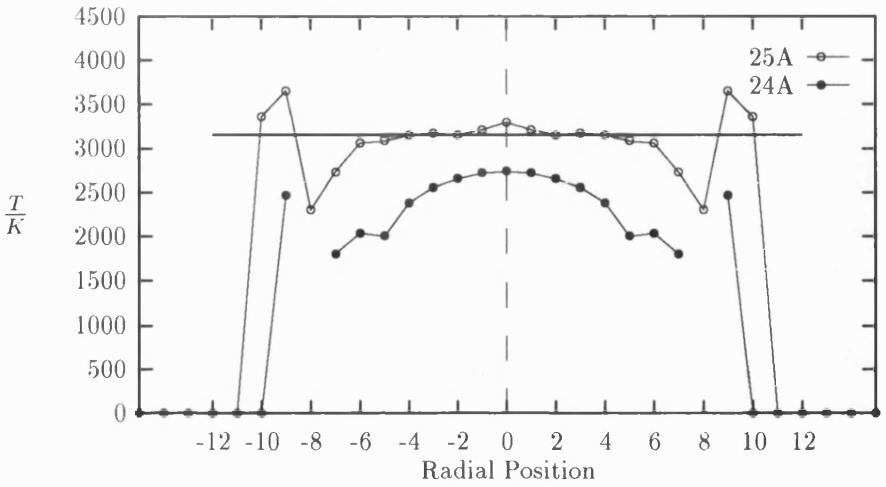

Figure 8.6: Comparison of temperature profiles generated on UO_2 for different flash lamp currents.

The unsmoothed and Fourier smoothed profiles have a flat section between radial positions 2 and 6, at a temperature of approximately 3000K. The nine point smoothed profile has no obvious flat area since the nine point window is wider than the section of peak; hence the peak is smoothed out. The flat areas correspond to a ring of melting material (see figure 7.4) which is at the melting point. The center of the sample hot-spot is at a higher temperature and therefore is molten material on the sample surface. The three profiles are compared in figure 8.8 as was done in the 24A case (figure 8.5).

The melting point has been determined by calculating the mean temperature of the five points contained within the step, together with a variance estimate made from the individual point variances. The temperatures (and standard deviations) of points 2–6 in the unsmoothed and Fourier profiles are listed in table 8.4, with

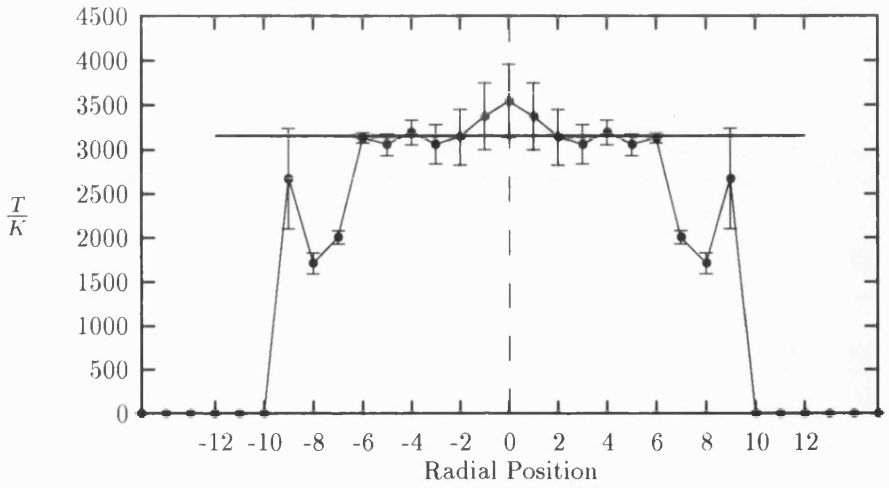

(a) No smoothing

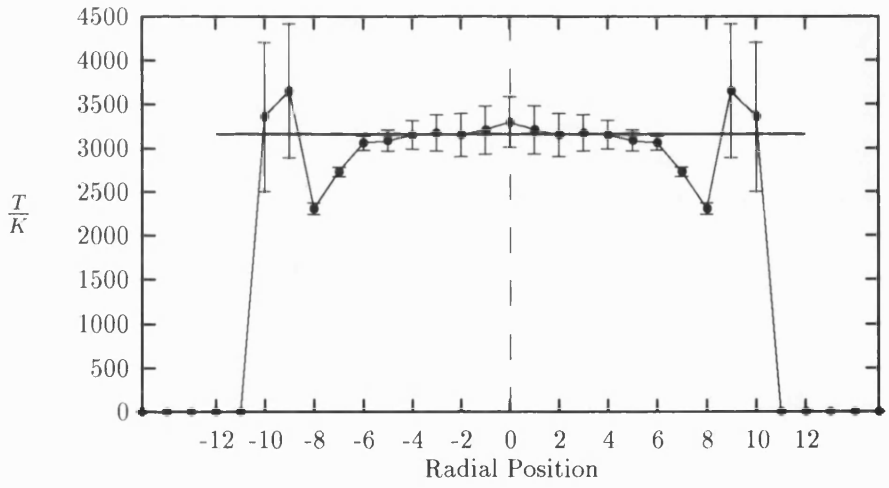

(b) Fourier smoothing

Figure 8.7: UO_2 profiles obtained with a laser flash lamp current of 25A using non-linear non-linear regression for temperature fitting.

the corresponding mean temperature across the melting ring.

Radial position	T/K	
	Unsmoothed	Fourier
2	3139 ± 309	3146 ± 245
3	3056 ± 219	3171 ± 208
4	3189 ± 138	3148 ± 164
5	3055 ± 121	3086 ± 121
6	3126 ± 56	3051 ± 80
Mean	3120 ± 51	3085 ± 60

Table 8.4: Measured temperatures along a 25A UO_2 profile step (rounded to nearest integer.

The error bounds on the calculated melting temperatures given in this table enclose the corresponding temperature obtained using the other smoothing technique. For example, the melting temperature of 3120±51 for unsmoothed analysis encloses the value of 3185K obtained for the smoothed fit, and vice versa. This implies that the smoothing process does not alter the overall shape of the curve, but merely reduces the amount of noise contained within it (as intended). The values of melting temperature given in table 8.4 compare well with published data which ranges between 3033K and 3153K [62,63,75–79] (all rounded to the nearest whole number of degrees), the associated measurement errors in the present data in table 8.4 enclosing these quoted values. The generally accepted value of melting temperature is taken as 3120K (from Rand, Ref [75]) without an associated error in most texts. This agreement validates the use of the remote temperature measuring technique for determining the properties of refractory materials such as UO_2 under extreme physical conditions.

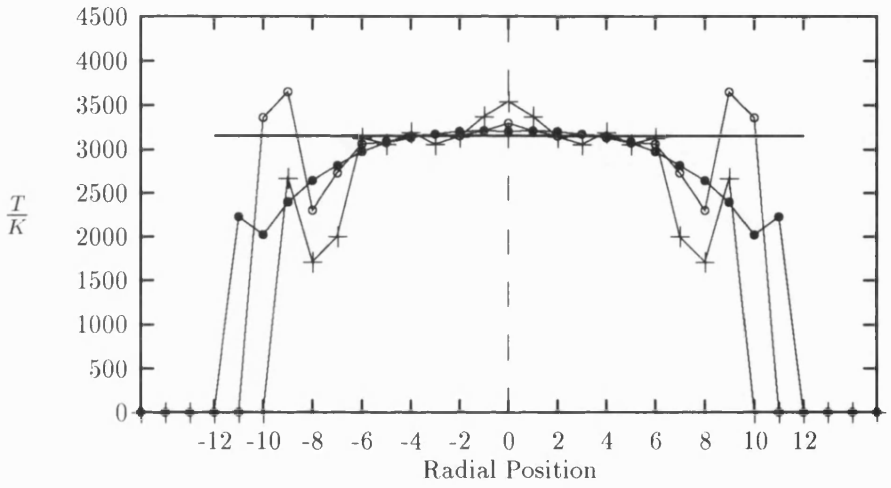

Figure 8.8: Comparison of smoothing effects on the 25A laser flash lamp current UO_2 temperature profile.

Chapter 9

Conclusions

The aim of this project was to design, construct and test a piece of equipment to generate extreme temperatures on the surface of a material under test, and then to measure the resulting temperature distribution. The measurement process is required to be as fast as possible, to allow the time evolution of the sample's surface temperature to be investigated. This heating/measurement system is also intended for use in conjunction with diamond anvil cells for studies at both high temperatures (up to 6000K) and high pressures (up to 100kbar routinely) simultaneously.

A system has been proposed by Heinz and Jeanloz [6] of the University of California, Berkeley, for measuring temperature distributions in laser heated diamond anvil cells. Their system is based on a four wavelength, spectro-radiometric temperature measurement process, with a scanning monochromator arrangement used to reconstruct the surface temperature distribution. The system described in this text is also a spectro-radiometric technique, but uses two dimensional charge cou-

pled device (CCD) methods to produce a near instantaneous image of the sample at over 500 separate wavelengths.

The two systems are based around the same measurement principle; the spectral distribution of light emitted from a set of narrow strips across the surface is transformed into a radial coordinate system using Abel transform techniques. The temperature as a function of radial distance from the centre of the heated spot is then reconstructed using the assumption that the sample emits light according to the Planck radiation law [80].

Although based on the same measurement principle, the techniques applied for performing the measurement are different between the two systems.

The Berkeley system is a single wavelength imaging system with a scanning slit used to construct the profile one line integral at a time. Four separate imaging processes are required to obtain the four spectra used in their temperature fitting process. Heinz and Jeanloz [6] estimate a period of 2–3 minutes to record each wavelength scan (the whole process taking up to 12 minutes), so no time dependent properties of the heated spot may be determined. The system described in this text uses a spectrograph in combination with a two dimensional CCD array rather than a scanning slit (see section 3.2.5). Its mode of operation is equivalent to the Berkeley system recording 384 points along 576 separate wavelength scans; however all the points are recorded simultaneously in the case of the CCD detector. The whole imaging process is performed in 10–50 milliseconds for most samples, and time dependent information is collected by recording an image at a set interval after the heating commences. It is considered that this system is a substantial

advance over the Berkeley implementation, and makes their system obsolete.

The present experimental and mathematical analysis procedures are described in chapters 3 to 5. To ensure that all parts of the apparatus are functioning correctly, this system has been tested using both a known temperature source and a material with a known melting point (see chapter 7). The results from these analyses demonstrate that the system is capable of accurately reconstructing the temperature profile generated on a heated sample allowing melting point measurements to be made directly.

The preliminary measurements performed on a sample of stoichiometric uranium dioxide (UO_2) confirm that the temperature generation apparatus can produce surface temperatures approaching 4000K, even at low laser flash lamp currents. The reconstructed profiles obtained for this sample have also enabled the melting point (T_m) of UO_2 to be determined at ambient pressure.

All the melting point measurements performed using this system on the two samples considered: iron (section 7.2) and UO_2 (chapter 8), are consistent with the respective published values, and are listed together in table 9.1.

Test Sample	Melting point (T_m/K)	Measured melting point (T_m/K)
Iron (30A)	1813	1812 ± 48
Iron (31A)	1813	1777 ± 63
UO_2	3120	3120 ± 51

Table 9.1: Comparison of calculated melting temperatures with published values for iron and UO_2.

The future aims of this project involve the application of standard heat conduction models to the reconstructed temperature profiles enabling the determination of both thermal conductivity and diffusivity. Full investigations of uranium dioxide at various stoichiometries between UO_2 and $UO_{2.2}$ are to be carried out. These experiments are hoped to provide information on the effect of oxygen interstitials on the thermodynamic properties of uranium dioxide.

The effects of pressure are to be investigated by heating samples contained within diamond anvil cells and measuring the resultant surface temperature distributions. These measurements will only be possible since the apparatus was designed to measure remotely (no surface contact).

Appendix A

Computer Implementation

The computer programming carried out for in this project can be divided into two areas: the calculation of temperature profiles from raw data, the visualisation of data sets before, during, and after the analysis procedure. These two cases are now considered individually.

A.1 Temperature Analysis

The entire analysis package, called OMA2T, is written in FORTRAN 77, and is run on an HP series 9000 model 720 workstation with 256 greyscale display. The analysis methods required for a particular data set are selected by entering the appropriate code numbers in a parameter file read by the program. This allows the same program to perform many different analyses without re-compilation of the code. The wavelength calibration is also supplied to the program (via the parameter file) as two entries: the base wavelength λ_0, the incremental wavelength $\Delta\lambda$,

together with the name of the file containing the spectral calibration coefficients and the cut-off value required (see sections 4.4.1 and 4.4.2). Again, these two entries allow alteration of calibration data without re-compilation of the source.

At important stages of the analysis, information about the data set is printed on screen, allowing progress to be monitored. Results from individual mathematical stages are also printed, for example the calculated vertical centre position of the data set, together with an error estimate (see section 5.3).

A.2 Data Visualisation

The Utah Raster Toolkit (URT) is a graphics suite based around the Run Length Encoded (RLE) graphic format. It can be used to convert raw data to and from greyscale (or full colour) images, and then to view the image on one of many different screen types. A helpful facility in the URT screen imaging routines is the ability to animate RLE pictures together, allowing direct comparisons of two or more images simply by looking for small colour/greyscale changes during the animation. For this experiment, the analysis package is run on a workstation using the X11 windows system, so the routines to view images on X workstations are used.

There are two main areas in which the URT package is used. The first, and probably the most useful, is during the analysis process. This allows the current state of the data to be seen on screen in real-time. Secondly, raw data files (and some intermediate data sets which the OMA2T program outputs) are imaged

separately from the analysis procedure, allowing subsequent analysis of the intermediate stages to determine the effects of the individual mathematical stages in the analysis procedure.

A.2.1 Within the Analysis Program

A special set of routines have been written which enable the URT package to be used from within the analysis program itself. The routines are written in C, and require the URT distribution to be available on the system, although only two of the URT routines are actually used. They are designed to allow the direct, on-screen imaging of a two-dimensional data set held in an array being used by the program. At present these routines only allow greyscale images to be generated on an X window system, however the routines may be altered to use other graphic systems and colours.

By using these routines after significant stages during the analysis procedure it is easy to determine whether the data set is responding as would be expected at each stage. For this experiment there are several main stages where it is useful to see the form of the data. The processes and algorithms used in each of these stages are listed separately in sections 5.1 to 5.7.

The first image output is the form of the raw data from the experiment itself. Viewing this set helps decide whether the data is non-symmetric, or if the optional smoothing stages are required, etc. Figure 5.1 is a typical image that would be obtained for data requiring the pre-smoothing stage; the removal of small

spots. The second image that is important is the data after the spectral correction process, as this shows whether all the ripples in the data (due to the dichroic mirror) have been removed (see section 3.2.1). These two are perhaps the most important stages for data visualisation, as the remaining analysis depends on the state of the data once the correction has been made. Later stages that may be useful include; before and after the Fourier pre-smoothing stage, after the symmetrisation of the set, and after the Abel inversion.

A.2.2 Output Data Files

Once a data file has been converted from its OMA form into ASCII ready for analysis (see section 3.2.7) it can also be converted into a graphic image. A stand-alone program has been written, based heavily on the subroutines outlined above, to provide the necessary conversion. This program (called **OMA2RLE**) converts the ASCII data into an **RLE** image which can be imaged on the screen at a later stage. These **RLE** files can be further converted into *PostScript* format using a standard **URT** package routine and then printed. All the data images in this text are converted using **OMA2RLE** and then imported as *PostScript* images.

One advantage of having the **RLE** images stored on disc is that the images can be animated together. This allows the small changes present in data sets before and after analysis stages to be detected, a process which would be extremely difficult if the two images were to be compared side by side. The **RLE** images can also be cropped and magnified, allowing small details of an image to be seen, an example being shown in figure 5.2, the original image shown in figure 5.1.

References

[1] Catlow C. R. A. Recent problems and progress in the study of UO_2 and mixed UO_2–PuO_2. *J. Chem. Soc., Faraday. Trans. 2*, **83**, 1065–1071, 1987.

[2] Hutchings M. T. High-temperature studies of UO_2 and ThO_2 using neutron scattering techniques. *J. Chem. Soc., Faraday. Trans. 2*, **83**, 1083–1103, 1987.

[3] Fritz I. J. Elastic properties of UO_2 at high pressure. *J. App. Phys.*, **47**, 4353–4358, 1976.

[4] Jayaraman A. Diamond anvil cell and high pressure physical investigations. *Rev. Mod. Phys.*, **55**, 65–108, 1983.

[5] Jayaraman A. Ultrahigh pressures (review article). *Rev. Sci. Instrum.*, **57**(6), 1013–1031, June 1986.

[6] Heinz D. L. and Jeanloz R. Temperature measurement in the diamond anvil cell. In: *High Pressure Research in Mineral Physics* (Manghnani M. H. and Syono Y., eds.), pages 113–127. American Geopyhsical Union, Washington D.C., 1987.

[7] Jayaraman A. Diamond anvil cell and high pressure physical investigations. In *Rev. Mod. Phys.* [4], page 67.

[8] Mao H. K. and Bell P. M. High pressure physics: The 1-megabar mark on the ruby R_1 static pressure scale. *Science*, **191**, 851–852, 1976.

[9] Mao H. K. and Bell P. M. High pressure physics: Sustained static generation of 1.36 to 1.72 megabars. *Science*, **200**, 1145, 1978.

[10] Mao H. K. and Bell P. M. Observations of hydrogen at room temperature (25°c) and high pressure (to 500 kilobars). *Science*, **203**, 1004, 1979.

[11] Mao H. K., Bell P. M., Dunn K. J., Chrenko R. M., and Devries R. C. Absolute pressure measurement and analysis of diamonds subjected to maximum static pressures of 1.3–1.7 mbar. *Rev. Sci. Instrum.*, **50**, 1002, 1979.

[12] Bassett W. A. and Takashi T. *Am. Mineral*, **50**, 1576, 1965.

[13] Moore M. J., Sorenson D. B., and Devries R. C. A simple heating device for diamond high anvil pressure cells. *Rev. Sci. Instrum.*, **41**, 1665, 1970.

[14] Hazen R. M. and Finger L. W. High-temperature diamond-anvil pressure cell for single-crystal studies. *Rev. Sci. Instrum.*, **52**, 75, 1981.

[15] Ming L. C., Manghnani M. H., and Balogh J. Resistive heating in the diamond anvil cell under vacuum conditions. In: *High Pressure Research in Mineral Physics* (Manghnani M. H. and Syono Y., eds.), pages 53–59. American Geopyhsical Union, Washington D.C., 1987.

[16] Shiferl D., Fritz J. N., Katz A. I., Schafer M., Skelton E. F., Qadri S. B., Ming L. C., and Manghnani M. H. Very high temperature diamond anvil cell for x-ray diffraction: Application to the comparison of the gold and tungsten high-temperature-high-pressure internal standards. In: *High Pressure Research in Mineral Physics* (Manghnani M. H. and Syono Y., eds.), pages 75–83. American Geopyhsical Union, Washington D.C., 1987.

[17] Liu L. G. and Bassett W. A. The melting of iron up to 200kbar. *J. Geophys. Rev.*, **80**, 3777, 1975.

[18] Ming L. C. and Bassett W. A. Laser heating in the diamond anvil cell press up to 2000°C sustained and 3000°C pulsed at pressures up to 260kbars. *Rev. Sci. Instrum.*, **45**, 1115–1118, 1974.

[19] Jeanloz R. and Heinz D. L. Experiments at high temperatures and pressure: Laser heating through the diamond cell. *Journal de Physique*, **45**(C8), 83–92, 1984.

[20] Hemley R. J., Bell P. M., and Mao H. K. Laser techniques in high pressure geophysics. *Science*, **237**, 605–612, 1987.

[21] Heinz D. L. and Jeanloz R. Measurement of the melting curve of $Mg_{0.9}Fe_{0.1}SiO_3$ at lower mantle conditions and its geophysical implications. *Journal of Geophysical Research*, **92**(B11), 11437–11444, October 1987.

[22] Grant G. A. *General Physics and Heat.* Edward Arnold, London, 1977.

[23] Benedict R. P. *Fundamentals of Temperature, Pressure and Flow Measurements.* Wiley Interscience, New York, 3^{rd} edition, 1984.

[24] Kostowski H. J. and Lee R. D. Theory and methods of optical pyrometry. In: *Temperature, its Measurement and Control in Science and Industry* (Brickwedde F. G., ed.), volume 3, page 449. Reinhold, New York, 1962.

[25] Coxon W. F., editor. *Physical Processes in the Chemical Industry*, volume V: Temperature Measurement and Control. Heywood, London, 1960.

[26] Heimann W. and Mestor U. Non contact determination of temperatures by measuring the infra-red radiation emitted from the surface of a target. In: *Temperature Measurement 1975* (Billing B. F. and Quinn T. J., eds.), pages 219–237, Bristol, 1975. Institute of Physics.

[27] Hoge H. J. Temperature measurement in engineering. In *Temperature, its Measurement and Control in Science and Industry*, volume 2, page 287. Reinhold, New York, 1955.

[28] Gentry P. J. A survey of the published data concerning the hemispherical emissivity of uranium dioxide. Technical Report ND-R-687(W), United Kingdom Atomic Energy Authority, Windscale Nuclear Power Development Laboratories, 1981. Northern Division Report.

[29] Levi L. *Applied Optics*, volume 2. Wiley, New York, 1980.

[30] O'Shay D. C. *Elements of Modern Optical Design.* Wiley, New York, 1985.

[31] Pedrotti F. L. and Pedrotti L. S. *Introduction to Modern Optics.* Prentice-Hall International, London, 1987.

[32] *Newport Catalog*, 1990.

[33] Hecht E. and Zajac A., editors. *Optics.* Addison-Wesley, Reading, Massachusetts, 2^{nd} edition, 1989.

[34] Jalkian R. D., Pomeroy R. S., Kolczynski J. D., Bonner Denton M., Lerner J. M., and Grayzel R. Evaluation and application of a holographic aberration corrected imaging spectrograph. *American Laboratory*, 1989.

[35] J–Y Optical Systems, Stanmore, Middlesex, UK. *The Optics of Spectroscopy. A Tutorial V2.0*, 1988.

[36] Certificate of calibration. Technical report, National Physical Laboratory, Teddington, Middlesex, 1986. Reference Number 127460/0P3.

[37] Chatfield C. *The Analysis of Time Series - An Introduction.* Chapman and Hall, London, 1984.

[38] Schultz M. H. *Spline Analysis.* Prentice-Hall, Eaglewood Cliffs, N.J., 1966.

[39] Bracewell R. N. *The Fourier Transform and its Applications.* McGraw-Hill, New York, 2^{nd} edition, 1971.

[40] Hoaglin D. C., Mosteller F., and Tukey J. W. *Exploring Data Tables, Trends and Shapes.* Wiley, New York, 1985.

[41] Dobson A. J. *An Introduction to Generalized Linear Models.* Chapman and Hall, London, 1991.

[42] Beaton A. E. and Tukey J. W. The fitting of power series, meaning polynomials, illustrated on band-spectroscopic data. *Technometrics*, **16**, 147–192, 1974. with discussion.

[43] Draper N. R. *Applied Regression Analysis.* Wiley, New York, 1981.

[44] Bates D. M. and Watts D. G. *Nonlinear Regression Analysis and its Applications.* Probability and Mathematical Statistics. Wiley, New York, 1988.

[45] Gill P., Murray W., and Wright M. H. *Practical Optimization.* Academic Press, London, 1981.

[46] Hartley H. O. The modified Gauss-Newton method for fitting of non-linear regression functions by least squares. *Technometrics*, **3**, 269–280, 1961.

[47] Radon J. Über die bestimmung von funktionen durch ihre integralwerte längs gewisser manningfaltigkeiten. *Berichte Sächsische Akademie der Wissenshaften.*, **69**, 262–267, 1917.

[48] Ding P., Mu Y., and Pan S. An interpolation solution of the Abel transformation for use in optically thick, cylindrically symmetric plasmas. *J. Quant. Spectrosc. Radiat. Transfer*, **45**(2), 115–119, 1991.

[49] Deans S. R. *The Radon Transform and some of its Applications.* Wiley Interscience, New York, 1983.

[50] Nestor O. H. and Olsen H. N. Numerical methods for reducing line and surface probe data. *SIAM rev.*, **2**, 200–207, 1960.

[51] Barr W. L. Method for computing the radial distribution of emitters in a cylindrical source. *J. Opt. Soc. Am.*, **52**, 885–888, 1962.

[52] Bockasten K. Transformation of observed radiances into radial distribution of the emission of a plasma. *J. Opt. Soc. Am.*, **51**(9), 943–947, 1961.

[53] Cremers C. J. and Birkebak R. C. Application of the Abel integral equation to spectrographic data. *Applied Optics*, **5**(6), 1057–1064, 1966.

[54] Brunner H. The numerical solution of a class of Abel integral equations by piecewise polynomials. *J. Comput. Phys*, **12**, 412–416, 1973.

[55] Piessens R. Calculation of the radial distribution of emitters in a cylindrical source. *Computer Physics Communications*, **5**, 294–298, 1973.

[56] Maldonado C. D., Caron A. P., and N O. H. New method for obtaining emission coefficients from emitted spectral intensities. Part I—circularly symmetric light sources. *J. Opt. Soc. Am.*, **55**(10), 1247–1254, 1965.

[57] Kalal M. and Nugent K. A. Abel inversion using fast Fourier transforms. *Appl. Opt.*, **27**(10), 1956–1959, 1988.

[58] Dong J. and Kearney R. J. Symmetrizing, filtering and Abel inversion using Fourier transform techniques. *J. Quant. Spectrosc. Radiat. Transfer*, **46**(3), 141–149, 1991.

[59] Hansen E. W. and Law P.-L. Recursive methods for computing the Abel transform and its inverse. *J. Opt. Soc. Am. A*, **2**(4), 510–520, 1985.

[60] Deutsch M., Notea A., and Pal D. Abel reconstruction of piecewise constant radial density profiles from X-ray radiographs. *Applied Optics*, **28**(15), 3183–3186, 1989.

[61] Dasch C. J. One-dimensional tomography: A comparison of Abel, onion-peeling, and filtered backprojection methods. *Applied Optics*, **31**(8), 1146–1152, 1992.

[62] Kaye G. W. C. and Laby T. H. *Tables of Physical and Chemical Constants and some Mathematical Functions.* Longman, London and New York, 15^{th} edition, 1986.

[63] Weast R. P., editor. *Handbook of Chemistry and Physics. Ready Refernce Book of Chemical and Physical Data.* CRC Press Inc., Cleveland, Ohio, 57^{th} edition, 1976.

[64] Dawson J. K. and Sowden R. G. *Chemical aspects of nuclear reactors.* Butterworths, London, 1963.

[65] Schoenes J. Electronic structure of uranium monochalcogenides and uranium monopnictides. *Physics Reports (Review Section of Physics Letters)*, **66**(5), 187–212, 1980.

[66] Catlow C. R. A. Point defects and electronic properties of uranium dioxide. *Proc. Roy. Soc. Lond. A*, **353**, 533–561, 1977.

[67] Catlow C. R. A. Oxygen diffusion in UO_2, ThO_2 and PuO_2. *J. Chem. Soc., Faraday. Trans. 2*, **83**, 1057–1069, 1987.

[68] Jackson R. A., Murray A. D., Harding J. H., and Catlow C. R. A. The calculation of defect parameters in UO_2. Technical Report TP-1109, Theoretical Physics Division, AERE Harwell, Oxfordshire, 1985.

[69] Yemel'Yanov V. S. and Yevstyukhin A. I. *Metallurgy of nuclear fuel. Properties and principles of the technology of uranium, thorium, and plutonium.* Pergamon Press, Oxford, 1969.

[70] Gronvold F. High temperature X-ray study of uranuim oxides in the UO_2–U_3O_8 region. *J. Inorg. & Nuclear Chem.*, **1**, 357, 1955.

[71] Loeb A. L. Thermal conductivity: VIII. a theory of thermal conductivity of porous materials. *J. Amer. Ceram. Soc.*, **36**, 332, 1954.

[72] Williamson R. Private communication. 1993.

[73] International Centre for Diffraction Data. *Powder Diffraction File*, 1992. Card number 41-1422.

[74] International Centre for Diffraction Data. *Powder Diffraction File*, 1992. Card number 6-598.

[75] Rand M. H., Ackermann R. J., Gronvold F., and Pattoret. *Rev. Int. Hautes Temp. Refract.*, **15**, 355–365, 1978.

[76] Lambertson W. A. and Mueller M. H. Uranium oxide phase equilibrium system, UO_2–MgO_2. *J. Amer. Chem. Soc.*, **36**, 332, 1953.

[77] Ehlert T. C. The melting point and spectral emissivity of UO_2. Master's thesis, University of Washington, 1958.

[78] Wisnyi J. G. and Pijanowski S. The melting point of UO_2. Technical Report KAPL-1658, U.S.A.E.C, 1956.

[79] Anderson J. S., Sawyer J. O., Worner H. W., Willis G. M., and Bannister M. J. Decomposition of uranium dioxide at its melting point. *Nature*, **185**, 915, 1960.

[80] Fowles G. R. *Introduction to Modern Optics.* Dover, New York, 2^{nd} edition, 1975.